

Summer 2015

Diamond MEMS Biosensors: Development and applications

Wenli Zhang
Louisiana Tech University

Follow this and additional works at: <https://digitalcommons.latech.edu/dissertations>



Part of the [Biomedical Engineering and Bioengineering Commons](#), [Chemical Engineering Commons](#), and the [Electrical and Computer Engineering Commons](#)

Recommended Citation

Zhang, Wenli, "" (2015). *Dissertation*. 188.
<https://digitalcommons.latech.edu/dissertations/188>

This Dissertation is brought to you for free and open access by the Graduate School at Louisiana Tech Digital Commons. It has been accepted for inclusion in Doctoral Dissertations by an authorized administrator of Louisiana Tech Digital Commons. For more information, please contact digitalcommons@latech.edu.

**DIAMOND MEMS BIOSENSORS: DEVELOPMENT AND
APPLICATIONS**

by

Wenli Zhang, B.S.

A Dissertation Presented in Partial Fulfillment
of the Requirements of the Degree
Doctor of Philosophy

**COLLEGE OF ENGINEERING AND SCIENCE
LOUISIANA TECH UNIVERSITY**

August 2015

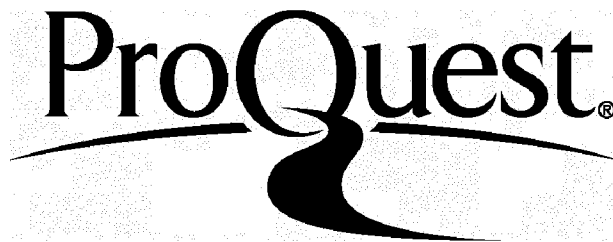
ProQuest Number: 3664520

All rights reserved

INFORMATION TO ALL USERS

The quality of this reproduction is dependent upon the quality of the copy submitted.

In the unlikely event that the author did not send a complete manuscript and there are missing pages, these will be noted. Also, if material had to be removed, a note will indicate the deletion.



ProQuest 3664520

Published by ProQuest LLC(2015). Copyright of the Dissertation is held by the Author.

All rights reserved.

This work is protected against unauthorized copying under Title 17, United States Code.
Microform Edition © ProQuest LLC.

ProQuest LLC
789 East Eisenhower Parkway
P.O. Box 1346
Ann Arbor, MI 48106-1346

LOUISIANA TECH UNIVERSITY

THE GRADUATE SCHOOL

JULY 2, 2015

Date

We hereby recommend that the Dissertation prepared under our supervision by
Wenli Zhang

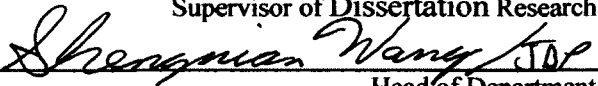
entitled DIAMOND MEMS BIOSENSORS: DEVELOPMENT AND
APPLICATIONS

be accepted in partial fulfillment of the requirements for the Degree of

Doctor of Philosophy in Engineering

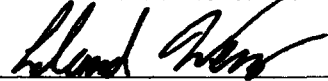



Supervisor of Dissertation Research


Head of Department

Engineering
Department

Recommendation concurred in:









Advisory Committee

Approved:



Director of Graduate Studies



Dean of the College

Approved:



Dean of the Graduate School

ABSTRACT

This research focuses on the development a dielectrophoresis-enhanced microfluidic impedance biosensor (DEP-e-MIB) to enable fast response, real-time, label-free, and highly sensitive sensor for bacterial detection in clinical sample. The proposed design consists of application of dielectrophoresis (DEP) across a microfluidic channel to one of the impedance spectroscopy electrodes in order to improve the existent bacterial detection limits with impedance spectroscopy. In order to realize such a design, choice of electrode material with a wide electrochemical potential window for water is very important. Conventional electrode material, such as gold, are typically insulated for the application of DEP, and they fail when used open because the DEP voltages avoiding electrolysis do not provide enough force to move the bacteria.

First, the use of nanodiamonds (ND) seeding gold surface to widen the electrochemical potential window is examined, since diamond has a wider potential window. ND seed coverage is a function of sonication time, ND concentration, and solvent of ND dispersion. Examining these parameters allowed us to increase the ND surface coverage to ~35%. With the highest ND coverage achievable, such electrodes are still susceptible to damage from electrolysis, however yield a unique leverage for impedance biosensing. When NDs is seeded at a 3x3 interdigitated electrode array, which act as electrically conductive islands between the electrodes and reduce the effective gap between the electrodes, thus allowing to perform impedance

spectroscopy in solutions with low electrical conductivity such as ITS. The changes obtained in resistance to charge transfer with bacterial capture is nearly twice than that obtained with plain electrodes.

Secondly, the feasibility of using boron-doped ultra nanocrystalline diamond (BD-UNCD) to apply DEP is tested without constructing a 3x3 IDE array. BD-UNCD electrodes can be used for DEP through tagging of the bacteria with immunolatex beads. This allows applying a larger DEP force on the bacteria. Since historically bead based assays are plagued with problems with non-specific binding, the role of different parameters including bead bioconjugation chemistry, bead PEGylation, BD-UNCD surface PEGylation, and DEP on specific and non-specific binding are tested. Most importantly DEP increases the specific binding and PEGylation of beads decreases the specific binding.

Finally, a 3x3 IDE array with BD-UNCD was fabricated, and used impedance spectroscopy to test the suitability of BD-UNCD IDEs for impedance biosensing. The huge electrode resistance and the charge transfer resistance at BD-UNCD IDEs poses a problem for impedance biosensing as it will lead to lower sensitivity.

BD-UNCD is the material of choice for applying DEP at open electrodes however gold is the choice of material for designing the chip interconnects. So the BD-UNCD layer should be as thin as possible and the interface between gold IDEs and the solution phase during DEP. The findings in this dissertation put us closer to realizing a DEP-e-MIB.

APPROVAL FOR SCHOLARLY DISSEMINATION

The author grants to the Prescott Memorial Library of Louisiana Tech University the right to reproduce, by appropriate methods, upon request, any or all portions of this Dissertation. It is understood that “proper request” consists of the agreement, on the part of the requesting party, that said reproduction is for his personal use and that subsequent reproduction will not occur without written approval of the author of this Dissertation. Further, any portions of the Dissertation used in books, papers, and other works must be appropriately referenced to this Dissertation.

Finally, the author of this Dissertation reserves the right to publish freely, in the literature, at any time, any or all portions of this Dissertation.

Author 

Date 07/27/2015

DEDICATION

Dedicated to my wife, parents and in-laws, for their love and support.

TABLE OF CONTENTS

ABSTRACT.....	iii
DEDICATION.....	vi
LIST OF FIGURES	xi
LIST OF TABLES.....	xvii
CHAPTER 1 INTRODUCTION	1
1.1 Statement of the Problem	1
1.2 Research Objectives	6
1.3 Structure of the Dissertation.....	6
CHAPTER 2 DIAMOND MEMS BIOSENSOR DEVELOPMENT AND APPLICATIONS.....	8
2.1 Introduction	8
2.2 Diamond Material Synthesis and Properties.....	9
2.2.1 Synthesis of microcrystalline diamond (MCD) and nanocrystalline diamond (NCD)	10
2.2.2 Synthesis of ultra nanocrystalline diamond	12
2.2.3 Properties of diamond films	15
2.2.3.1 Mechanical properties	15
2.2.3.2 Electrical, thermal and electrochemical properties.....	19
2.2.3.3 Biological properties	22
2.3 Micro/Nanofabrication Methods for Diamond Films	23

2.3.1 Conformal diamond coating.....	23
2.3.2 Selective deposition.....	24
2.3.3 Photolithography and reactive ion etching processes.....	25
2.4 Functionalization of Diamond Surfaces.....	27
2.4.1 Surface terminations.....	28
2.4.2 Photochemical methods of functionalizing diamond surfaces	30
2.4.3 Electrochemical method of functionalized diamond.....	32
2.4.4 Chemical functionalization of H-terminated diamond surfaces.....	33
2.5 Diamond Surface for MEMS Biosensing Applications.....	34
2.5.1 Diamond thin film for electrochemical biosensor applications.....	35
2.5.1.1 Electrochemical biosensing using H-terminated diamond electrodes	35
2.5.1.2 Electrochemical biosensing using O-terminated diamond	36
2.5.1.3 Electrochemical biosensing with biomolecule functionalized diamond surfaces	37
2.5.1.4 Electrochemical biosensing using nanostructured diamond electrodes.....	39
2.5.1.5 Detection using impedance spectroscopy	41
2.5.2 Diamond micro-cantilever based biosensor	43
2.5.3 Diamond-based field-effect transistor (FET) biosensors	44
2.6 Summary	44
CHAPTER 3 NANOSTRUCTURING OF BIOSENSING ELECTRODES WITH NANODIAMONDS FOR ANTIBODY IMMOBILIZATION	49
3.1 Introduction.....	49
3.2 Methods.....	53
3.2.1 Materials.....	53
3.2.2 ND seeding and analysis	53

3.2.3 Functionalization of NDs	55
3.2.4 Fluorescent labeling of bacteria.....	56
3.2.4 Bacteria capture experiment	56
3.2.5 Biosensor fabrication and testing	57
3.3 Results and Discussion.....	57
3.4 Conclusion.....	76
CHAPTER 4 REDUCTION OF NON-SPECIFIC BINDING IN BEADS-BASED DIELECTROPHORETIC PRECONCENTRATION AT DIAMOND ELECTRODES	78
4.1 Introduction	78
4.2 Materials and Methods.....	82
4.2.1 Materials	82
4.2.2 Coimmobilization of IgG and PEG on epoxy-/sulfate- modified PS beads or epoxy-modified magnetic beads.....	83
4.2.3 Coimmobilization of IgG and PEG on carboxylate-modified PS beads	84
4.2.4 Coimmobilization of IgG and PEG on aldehyde-/sulfate-modified PS beads	84
4.2.5 Coimmobilization of mouse IgG and PEG on BD-UNCD	85
4.2.6 Preparation of microfluidic channel with BD-UNCD functionalized surface	86
4.2.7 Specific and non-specific adsorption of functionalized beads on functionalized BD-UNCD surface.....	88
4.2.8 Comparing the pathogen capture performance of different beads	89
4.3 Result and Discussion	89
4.4 Conclusion.....	110

CHAPTER 5 BD-UNCD IMPEDANCE BIOSENSOR MICROFABRICATION AND POTENTIAL BIOSENSING APPLICATIONS TESTING	111
5.1 Introduction	111
5.2 Materials and Methods	113
5.2.1 Materials	113
5.2.2 BD-UNCD impedance biosensor fabrication	114
5.2.3 Coimmobilization of FITC-labeled goat anti-mouse IgG and PEG on BD-UNCD	116
5.2.4 Biosensor testing	117
5.3 Result and Discussion	117
5.4 Conclusion.....	129
CHAPTER 6 CONCLUSION AND FUTURE WORK RECOMMENDATIONS	130
6.1 Conclusion.....	130
6.2 Future Work Recommendations.....	133
REFERENCES	135

LIST OF FIGURES

Figure 1-1: Components of biosensors.	1
Figure 1-2: Scheme of dielectrophoresis-enhanced microelectrode impedance biosensor (DEP-e-MIB).....	3
Figure 2-1. Surface morphology of (A) triangular MCD, (B) rectangular MCD film, (C) cauliflower morphology MCD film, and (D) a NCD film.....	10
Figure 2-2. Processes of selective deposition of diamond, (A) using photoresist to prevent surface exposing to diamond particles, (B) using diamond-loaded photoresist to produce a pattern of nucleation, and (C) seeding the whole surface and lithographic etch the selective area to generate patterns.....	25
Figure 2-3. Schematic showing lithographically-based microfabrication process of diamond MEMS.....	27
Figure 2-4. 254 nm UV-light photochemical functionalization of H-terminated diamond using alkene molecules.....	32
Figure 2-5. Electrochemical functionalization of diamond electrodes using arly diazonium molecules.....	33
Figure 2-6. Reaction scheme of the spontaneous grafting process.....	34
Figure 2-7. Schematic DNA hybridization detection mechanism using $\text{Fe}(\text{CN})_6^{3-/4-}$ as mediator redox molecules.....	39
Figure 3-1. Measurement of ND particle sizes after dilution of the original ND containing DMSO with acetone, ethanol, isopropyl alcohol (IPA), methanol, and water. Average values are reported from five repeats.	58
Figure 3-2. Results from photon correlation spectroscopy showing size distribution of ND aggregates obtained by diluting the original ND:DMSO solution with acetone, ethanol, water, IPA, and ethanol.....	59
Figure 3-3. Measurement of ND particle mobility (μ_e) after dilution of the original ND containing DMSO with acetone, ethanol, isopropyl alcohol (IPA), methanol, and water. Average values are reported from five repeats.	60

Figure 3-4.	Measurement of ND particle zeta potential (Z) after dilution of the original ND containing DMSO with acetone, ethanol, isopropyl alcohol (IPA), methanol, and water. Average values are reported from five repeats.....	60
Figure 3-5.	On the left is the SEM image showing NDs (bright white spots) seeded on gold surfaces by sonication in solution containing NDs at 0.25% (w/v) for 30 minutes. On the right is the SEM image after 2D FFT filtering highlights the seeded NDs as red regions.....	62
Figure 3-6.	Surface coverage of NDs obtained on surfaces seeded for varying amounts of times with methanol solutions containing 0.25%, 0.125%, and 0.08% (w/v) NDs.....	63
Figure 3-7.	Fluorescence images obtained from a 10x10 array of 12 μm spots of FITC labeled anti- <i>E. coli</i> O+K attached to ND-seeded surfaces without (A) and with (B) sodium borohydride reduction treatment prior to performing UV assisted TFAAD linkage to NDs.	64
Figure 3-8.	Normalized fluorescence intensity obtained from seven 10x10 arrays on ND surface with and without reduction	64
Figure 3-9.	Bacteria capture density obtained using the antibody-ND coating as a function of surface coverage of NDs on the sample.....	65
Figure 3-10.	Optical images of a biosensor chip containing an array of nine interdigitated electrode (IDE) pairs that were fabricated to demonstrate the application of ND seeding layer for chemically stable covalent linkage of antibodies to electrodes. Each IDE contained sixty finger pairs with each finger 9 μm wide and spaced 9 μm apart.....	67
Figure 3-11.	A representative plot of real <i>versus</i> imaginary part of the impedance measured in de-ionized water on an IDE before and after ND seeding.....	67
Figure 3-12.	Representative plot of impedance magnitude and phase plotted against frequency as obtained on an IDE exposed to solutions with different electrical conductivity.....	68
Figure 3-13.	Example impedance spectra on an active sensors before (baseline) and after exposure to 10^6 cells/ml or 10^8 cells/ml of <i>E. coli</i> O157:H7 cells.....	70
Figure 3-14.	A modified Randles circuit that best fit our impedance results.....	70
Figure 3-15.	Significant changes observed in charge transfer resistance (R_{ct}), (R_n), and (W_{s1} -R) upon binding of bacterial cells to the sensor surface.....	72
Figure 4-1.	Co-immobilization of IgG and PEG on epoxy-/sulfate-modified beads.....	81
Figure 4-2.	Co-immobilization of IgG and PEG on carboxylate-modified beads.....	81

Figure 4-3. Co-immobilization of IgG and PEG on aldehyde-/sulfate-modified beads.....	81
Figure 4-4. Co-immobilization of IgG and PEG on BD-UNCD surface using the UValkene chemistry. (A) As-deposited BD-UNCD is hydrogen terminated. (B) TFAAD grafted to BD-UNCD surface. (C) Trifluoroacetic acid group is deprotected to create primary amines. (D) Reductive glutaraldehydation of the primary amines on the BD-UNCD surface. (E) Reaction with primary amines on the IgG with the aldehydes on the BD-UNCD surface followed by reaction of remainder of the aldehyde groups with the primary amines of the PEG.....	86
Figure 4-5. (A) Exploded view of the microfluidic preconcentrator showing different layers of construction. (B) A packaged microfluidic preconcentrator under testing.....	88
Figure 4-6. (A) Calibration chart correlating the 280 nm UV absorption to the BGG standard concentrations. (B) Amount of antibody reacted with carboxylate-modified (blue columns), aldehyde-/sulfate (red columns) and epoxy-/sulfate (green columns) PS beads, and epoxy-modified magnetic beads (yellow columns) as a function of incubation time as calculated using UV absorption at 280 nm.....	91
Figure 4-7. (A) Calibration chart correlating the absorption at 652 nm when measured using the micro-BCA assay to the BGG standard concentrations. (B) Amount of antibody reacted with carboxylate modified (blue columns), aldehyde-/sulfate (red columns) and epoxy-/sulfate (green columns) PS beads, and epoxy-modified magnetic beads (yellow columns) as a function of incubation time as calculated using the micro-BCA assay.....	92
Figure 4-8. The electrophoretic mobility experimentally measured for carboxylate-modified, aldehyde-/sulfate and epoxy-/sulfate beads as received, after antibody attachment, and after PEG co-immobilization.....	94
Figure 4-9. The zeta-potential measurement of CML, aldehyde/sulfate and epoxy sulfate beads after antibody and PEG attached.....	94
Figure. 4-10 CML, aldehyde/sulfate, epoxy/sulfate and magnetic epoxy <i>E. coli</i> O157:H7 antibody and PEG functionalized beads bacteria isolating efficiency study in <i>E. coli</i> O157:H7 cell culture.....	96
Figure. 4-11 CML, aldehyde/sulfate, epoxy/sulfate and magnetic epoxy <i>E. coli</i> O157:H7 antibody and PEG functionalized beads bacteria isolating efficiency in <i>E. coli</i> O157:H7 with <i>E. coli</i> K12 mixed culture.....	97

Figure. 4-12 CML, aldehyde/sulfate, epoxy/sulfate and magnetic epoxy <i>E. coli</i> O157:H7 antibody and PEG functionalized beads bacteria isolating selectivity study in <i>E. coli</i> O157:H7 with <i>E. coli</i> K12 mixed culture.....	98
Figure 4-13. The accuracy of antibody immobilized beads capture <i>E. coli</i> O157:H7 in the mixed <i>E. coli</i> O157:H7 and <i>E. coli</i> K12 culture.....	99
Figure 4-14. The sensitivity of antibody immobilized beads capture <i>E. coli</i> O157:H7 in the mixed <i>E. coli</i> O157:H7 and <i>E. coli</i> K12 culture.....	100
Figure 4-15. The specificity of antibody immobilized beads capture <i>E. coli</i> O157:H7 in the mixed <i>E. coli</i> O157:H7 and <i>E. coli</i> K12 culture.....	100
Figure. 4-16 The specific capture test of anti-mouse IgG functionalized microspheres on BD-UNCD surface with or without PEG immobilization without DEP applied. (** represents $p>0.05$).....	102
Figure. 4-17 The non-specific capture test of anti-mouse IgG functionalized microspheres on BD-UNCD surface with or without PEG immobilization without DEP applied.....	102
Figure. 4-18 The specific capture test of anti-mouse IgG functionalized microspheres on BD-UNCD surface with or without PEG immobilization with DEP applied. (** represents $p>0.05$).....	104
Figure. 4-19 The non-specific capture test of anti-mouse IgG functionalized microspheres on BD-UNCD surface with or without PEG immobilization with DEP applied. (** represents $p>0.05$).....	105
Figure. 4-20 The specific capture test of anti-mouse IgG functionalized microspheres on BD-UNCD surface with or without PEG immobilization without DEP applied. (** represents $p>0.05$).....	107
Figure. 4-21 The non-specific capture test of anti-mouse IgG functionalized microspheres on BD-UNCD surface with or without PEG immobilization without DEP applied. (* represents $p<0.05$).....	108
Figure. 4-22 The specific capture test of anti-mouse IgG functionalized microspheres on BD-UNCD surface with or without PEG immobilization with DEP applied. (** represents $p>0.05$).....	109
Figure. 4-23 The non-specific capture test of anti-mouse IgG functionalized microspheres on BD-UNCD surface with or without PEG immobilization with DEP applied. (** represents $p>0.05$).....	109

Figure 5-1. Process flow of fabricating BD-UNCD impedance sensor. (A) 2 μm thick BD-UNCD film on 525 μm thick silicon wafer which has 1 μm thick silicon dioxide on it, (B) 1 μm thick silicon dioxide was deposit on BD-UNCD film via PECVD, (C) the wafer processed through regular photolithography and buffered oxide etching process to generate patterns on silicon dioxide, (D) the silicon dioxide patterns were used as mask to etch BD-UNCD film in ICP-RIE system and removed with BOE after etching BD-UNCD film, (E) 500 nm silicon dioxide was deposit on the wafer via PECVD as an insulation layer, (F) a regular photolithography and buffered oxide etching process were performed to open the windows on sensor electrodes parts and connection fingers parts.....	115
Figure 5-2. The images of fabricated BD-UNCD impedance sensor (A). The microscope images of IDE electrodes with different magnifications (B) 100x, (C) 200x, and (D) 500x.....	118
Figure 5-3. Fluorescent image of (A) fabricated BD-UNCD surface and (B) non fabricated BD-UNCD surface with the attachment of FITC-label goat anti-mouse IgG via UV-alkene chemistry.....	119
Figure 5-4. Fluorescent intensity of both surface with negative control.....	120
Figure 5-5. Equivalent circuit diagram for curve fit using impedance spectroscopy....	123
Figure 5-6. Nyquist Plots on impedance spectroscopy obtained from nine sensors (for 0.1xPBS).....	124
Figure 5-7. Charge transfer resistance (R_{ct}) in ohm obtained for all nine sensors.....	125
Figure 5-8. Bode Plots on nine sensors for 0.1xPBS.....	126
Figure 5-9. Parameter plots, electrode resistance for all nine sensors in 0.1x PBS.	127
Figure 5-10. Parameter plots, double layer capacitance, (C) space charge capacitance $W1-P$ for all nine sensors in 0.1x PBS.....	127
Figure 5-11. Parameter plots, space charge capacitance parameter for all nine sensors in 0.1x PBS.	128
Figure 5-12. Parameter plots, Warburg resistance for all nine sensors in 0.1x PBS.	128
Figure 5-13. Parameter plots, Warburg parameter $W1-T$ for all nine sensors in 0.1x PBS.....	129
Figure 5-14. Parameter plots, Warburg parameter $W1-P$ for all nine sensors in 0.1x PBS.....	129

Figure 6-1. (A) Scheme of the new design of DEP-e-MIB, and (B) cross view of IDE.....	134
--	-----

LIST OF TABLES

Table 2-1. Characteristics of diamond films.....	14
Table 2-2. Mechanical and tribological properties of Si and UNCD film.....	16
Table 2-3. Diamond biosensor appears in the past two decades and references.....	45
Table 3-1. Equivalent Circuit Fit Values for One of the Active and Control Sensors.....	72
Table 3-2. Properties of solvent mixtures estimated from molar ratio weighted calculations.....	74
Table 3-3. Equivalent Circuit Fit Values for the Other Two Active Sensors.....	75
Table 3-4. Equivalent Circuit Fit Values for the Other Control Sensor.....	76
Table 4-1. Specificity of capture calculated from data in Figures 4-16, 4-17, 4-18, and 4-19.....	106
Table 4-2. Specificity of capture calculated from data in Figure 4-20, 4-21, 4-22, and 4-23.....	110
Table 5-1. Equivalent circuit on impedance spectroscopy.....	121

ACKNOWLEDGMENTS

I would like to thank my parents, Mr. Xueqing Zhang, Mrs. Bo Hu, and my in-laws, Mr. Tuanzhong Han and Mrs. Xuexia Zhang for their love and support.

I would like to thank my wife, Bing Han for being my greatest supporter and soul mate during my PhD life. Her patience, understanding and commitment to me are the invaluable contributions to my achievement.

I would like to thank my dear advisor Dr. Adarsh Radadia for being my mentor, and teaching me so many things including my research. He helped me to grow stronger and tougher in my research life, and taught me how to be an independent researcher.

I would like to thank my group mates, Kush Patel and Nowzesh Hasan, for their help on some parts of my research project.

CHAPTER 1

INTRODUCTION

1.1 Statement of the Problem

MEMS biosensor research and application has seen a rapid growth in the last decade [1]. There are four main components in a biosensor, namely the bioreceptor, the transducer, the amplifier, and the microelectronic data processor, as shown in Figure 1-1. Immobilized ss-DNA, aptamers, enzymes, antibodies, microorganisms, or whole cells are typically used as the bioreceptor layer. The transducer in a biosensor converts the information of target-bioreceptor interaction into an electrical, optical, or thermal signal. The amplifier and microelectronics further process this signal into a readable and quantifiable data.

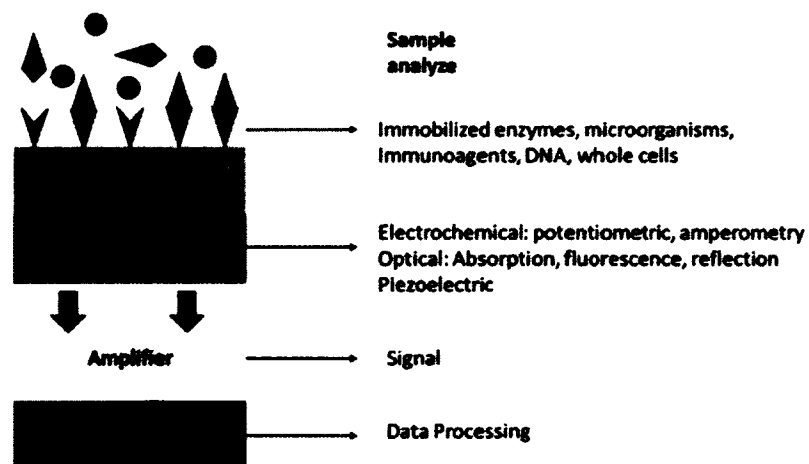


Figure 1-1: Components of biosensors.

Current clinical testing for bacterial infections is carried out using either enzyme-linked immune-sorbent assay (ELISA), polymerase chain reaction (PCR) or cell culture methods[2, 3]. The cell culture methods of detecting bacteria in clinical samples achieves the lowest detection limit, typically few cells/ml, but the whole process takes at least 6 hours, depending on the bacteria, sometimes taking up to several days for difficult to grow bacteria. The PCR based methods can detect bacterial infections down to 10 cell/ml with high degree of selectivity, however the reagent preparation is cumbersome and vulnerable to contamination, and takes up at least 12 hours. The ELISA-based methods are quicker to process, typically requiring only 4 hours of work time, however it is not as sensitive as the PCR, the limits of detection are on the order of 1000 cells/ml. Moreover, neither of the above techniques is field-portable, as they require bulky instruments for performing the tests. Electrical biosensors hold the potential to meeting the needs of field-portability, however, the detection limits of such biosensors do not match to the detection limit of PCR or ELISA.

In this dissertation, to achieve better detection limits through a new electrical biosensing scheme called dielectrophoresis-enhanced microfluidic impedance biosensing (DEP-e-MIB) was proposed as shown in Figure 1-2. Impedance spectroscopy is carried out using a pair of interdigitated electrodes decorated with immobilized bioreceptors (antibodies, DNA/RNA, proteins, and aptamers). A small sinusoidal excitation potential is applied across the impedance electrodes and the impedance change is monitored to detect the binding of target molecules to the bioreceptors. This makes impedance spectroscopy a rapid, label-free, and real-time detection scheme. Further the small size of the measurement device makes this technique field deployable. Detection limits down to

10^5 bacterial cells/ml [2], 10^3 EID₅₀ (avian influenza virus H5N1)/ml [4], 0.02 fg protein (interferon- γ)/ml [5], and 1 nM ssDNA [6] have been demonstrated with impedance spectroscopy.

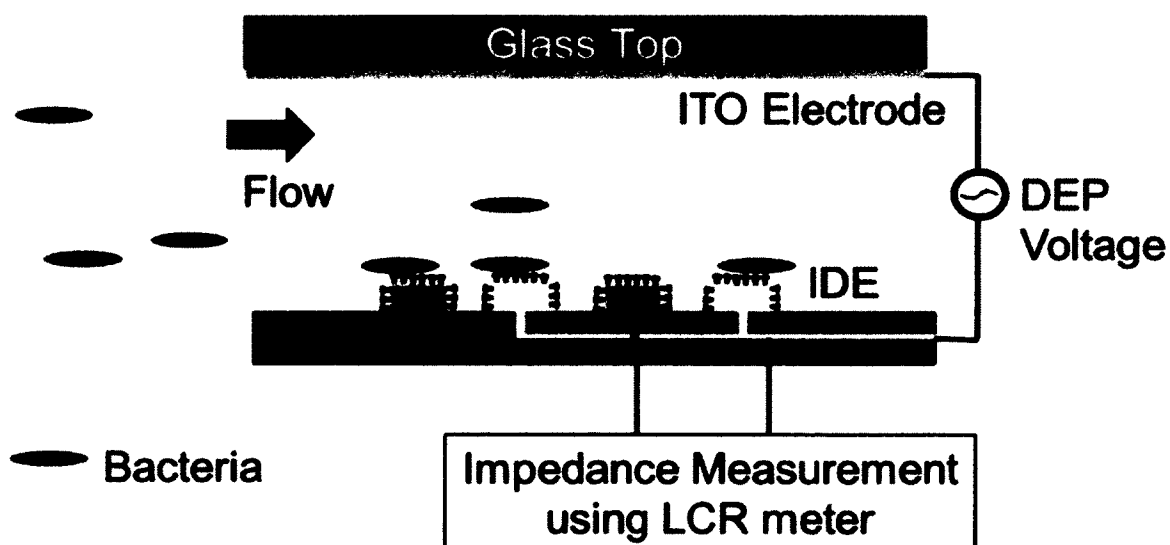


Figure 1-2. Scheme of dielectrophoresis-enhanced microelectrode impedance biosensor (DEP-e-MIB).

To improve the detection limit of impedance biosensing using microfluidics and DEP-enhanced concentration of bacteria at the impedance sensor has been proposed, as shown in Figure 1-2. The DEP-e-MIB is packaged with a microfluidic channel to flow liquid samples containing bacteria and thereby provide a more thorough contact between the liquid sample and the relatively small area of the impedance sensor. Using DEP for isolating and concentrating cells has already been reported widely.[7-10] In 2007, Cheng *et al.* has reported a 3D DEP gate chip for cell sorting and concentrating to increase the performance of biosensing.[11] One of the impedance sensor electrode and the indium tin oxide (ITO) coating on the glass top are used to apply the DEP voltage across the height

of the microfluidic channel and thus ensures deeper penetration of the DEP field. This is advantageous over the planar DEP electrodes applied over interdigitated electrodes. The positive DEP force will bring the bacteria in the vicinity of the bioreceptor layer on the impedance sensor. This way DEP and microfluidic are proposed to improve our sensor's sensitivity. After flowing sample, the DEP voltage will be switched off, the microfluidic channel will be washed to remove non-specifically bound material and the impedance change of the biosensor will be measured using a portable electrochemical interface and impedance analyzer.

DEP is typically carried out with insulated electrodes while impedance spectroscopy is carried out using open electrodes and thus experimentally one would use two separate sets of electrodes. The unique part of our design is that through the proper choice of electrode material, to carry out DEP and impedance spectroscopy using a shared electrode was proposed. This simplifies the design and the fabrication process. The insulation on the DEP electrodes is used to avoid electrolysis, and Joule heating, which can damage fragile microfabricated electrodes. The electrode material influences the voltages at which water oxidizes or reduces, also called its electrochemical window. In a 1 M KCl solution, the electrochemical window is between +1.5 V and -0.6 V for gold electrode vs. Ag wire. Comparatively, the electrochemical window of diamond vs. Ag/AgCl is between +1.9 V and -1 V. Within the last two decades, boron-doped diamond electrodes have become popular as they present a wider electrochemical window for water compared to gold and platinum. The electrochemical window is between +2.6 V and -1.9 V for boron doped ultra nano crystalline diamond (BD-UNCD) electrode.

Diamond thin films have good electrochemical stability [12, 13], high Young's modulus, biocompatibility and chemical stability[14]. Moreover, diamond thin films can now be deposited on silicon and other microelectronic compatible substrates by chemical vapor deposition (CVD) processes, which are readily integrable with other semiconductor practices [15]. Until recently, one of the biggest challenges in diamond-based biosensing was to develop an interface for integrating microelectronics and biotechnology [14, 16-18]. Multiple electro- and photo- chemical surface functionalization methods have now been reported to immobilize DNA, enzymes, and antibodies on the diamond surface and tested for biosensing applications. One of the chemical methods includes the UV-alkene chemistry where the 254-nm or smaller wavelength UV ejects electrons off the diamond carbon atoms into the adjacent alkene molecules, leading to covalent attachment of alkenes to the diamond carbon atoms by S_N1 reaction mechanism. Using this chemistry, Wang *et al.* have shown improved stability of DNA-modified ultra nanocrystalline diamond (UNCD) films to thermal cycling conditions over DNA-modified silicon, gold, glass, and glassy carbon surfaces. This is because the UV-alkene chemistry results in a hydrolytically stable C-C linkage that is able to withstand 30 times thermal cycling of hybridization-dehybridization of surface bound DNA while glass, gold and silicon surfaces only lasted for five to ten such cycles.[19] Hartl *et al.* functionalized enzyme catalase on nitrogen-doped nanocrystalline diamond surface exhibiting n-type resistivity between 1 and 3.33 Ω -cm and demonstrated suitability of diamond for creating electrical biosensors. An enzyme-modified diamond electrode showed direct electron transfer between the enzyme's redox center and the diamond electrode with a lower background current and a better stability than gold electrodes decorated with catalase.[17] Recently,

Radadia *et al.* immobilized antibodies to UNCD using the UV-alkene chemistry and tested its suitability for bacterial biosensing.[18] UNCD surface chemistry showed improved temporal stability of antibodies on UNCD compared to glass surfaces when exposed to saline media at 37 °C for prolonged periods extending up to two weeks. These results strengthen the need to build and investigate the performance of diamond-based biosensors.

Thus in this dissertation, DEP-e-MIB with gold electrodes, nanodiamond-seeded gold electrodes, and boron-diamond electrodes were fabricated and tested to carry out the daunting task of applying DEP-based concentration at open electrodes and impedance biosensing.

1.2 Research Objectives

(1) Fabricate a 3x3 interdigitated electrode array with nanodiamond (ND) coated gold electrodes and test it for DEP and impedance spectroscopy.

(2) Fabricate a 3x3 interdigitated electrode array with boron-doped ultra nanocrystalline diamond electrodes and test it for DEP and impedance spectroscopy.

1.3 Structure of the Dissertation

Chapter 2 provides the necessary background information about the different growth methods and properties of diamond thin films, which makes diamond more suitable for biosensing applications. Also, examples of diamond biosensor developed so far have been illustrated.

Chapter 3 provides development of the nanodiamond seeding process to generate a uniform coating of diamond nanoparticle and its application for DEP and impedance spectroscopy using a 3x3 interdigitated electrode array.

Chapter 4 introduces the concept of using immunolatex beads as DEP tags to the original DEP-e-MIB design and examines the influence of chemistry of the bead chemistry and BD-UNCD chemistry in the preconcentration of beads.

Chapter 5 demonstrates the fabrication of a 3x3 interdigitated electrode array made with boron-doped ultra nanocrystalline diamond. In addition, the suitability of this sensor for DEP and impedance biosensing has been evaluated.

Chapter 6 summarizes the key findings during my dissertation research and suggest possible 3x3 interdigitated electrode array design that holds potential to realizing DEP-e-MIB assay.

CHAPTER 2

DIAMOND MEMS BIOSENSOR DEVELOPMENT AND APPLICATIONS

2.1 Introduction

Micro-electro-mechanical systems (MEMS) encompass technologies implemented at characteristic lengths from nanometers to microns. MEMS devices have already been widely applied in information technology, biosensing, biotechnology and national security [20-22]. An ideal material for constructing MEMS devices should result in low cost, stability and reproducibility. Current MEMS technology is dominated by silicon (Si) based materials and the suite of fabrication technologies inherited from the microelectronics industry. Hence, Si forms an optimal choice to mass-produce MEMS biosensors; however, Si lacks the chemical, mechanical and biological stability required for stable and reproducible sensing results. Further Si has a small energy band gap to start with in the quest of higher sensitivity for electrical biosensors. This creates a need for an alternative substrate material for MEMS biosensors. Studies on diamond have unveiled a number of excellent properties that are absent in Si and other usable materials [23, 24], which has made the diamond material as an attractive choice for MEMS biosensing applications. The attractive properties of diamond in MEMS biosensing applications can be illustrated as of reduced frictional coefficients, increased resistance to wear, higher

Young's modulus, tensile and fracture strength, excellent thermal conductivity, low coefficient of thermal expansion, biocompatibility, high mechanical strength and tribological effective comparing with Si. In addition, suitable doping could diverge the electrical properties of diamond from insulation to semi-metal.

Usage of diamond in MEMS biosensing applications can be used in two ways, as a coating material to improve the functionality of an existing MEMS design [25, 26] or as a structural material to deliver a unique performance [27] which is unobtainable with other prevalent materials. This chapter will review and highlight the development and application of diamond-based MEMS biosensors. In Section 2.2, a briefly discussion of the syndissertation and properties of diamond film has been illustrated. In Section 2.3, the fabrication method of diamond thin film for MEMS biosensing devices will be presented. The surface modification of diamond film for biosensing application will be discussed in Section 2.4. In the last section, development and application of diamond materials in the MEMS biosensing field will be reviewed.

2.2 Diamond Material Syndissertation and Properties

Diamond growth by chemical vapor deposition (CVD) has been reported since the 1960s [28]. The application of diamond materials in the research and industrial area became active and extensive beginning in the 1980s. Several types of diamond thin film have been synthesized and studied on their different microstructures, surface morphologies and other properties. In this section, the syndissertation and properties of microcrystalline diamond (MCD), nanocrystalline diamond (NCD), ultra nanocrystalline diamond (UNCD) and boron-doped ultra nanocrystalline diamond (BD-UNCD) has been

reviewed, as shown in Figure 2-1. The CVD diamond thin film has different surface properties with different seeding processes and growth species.

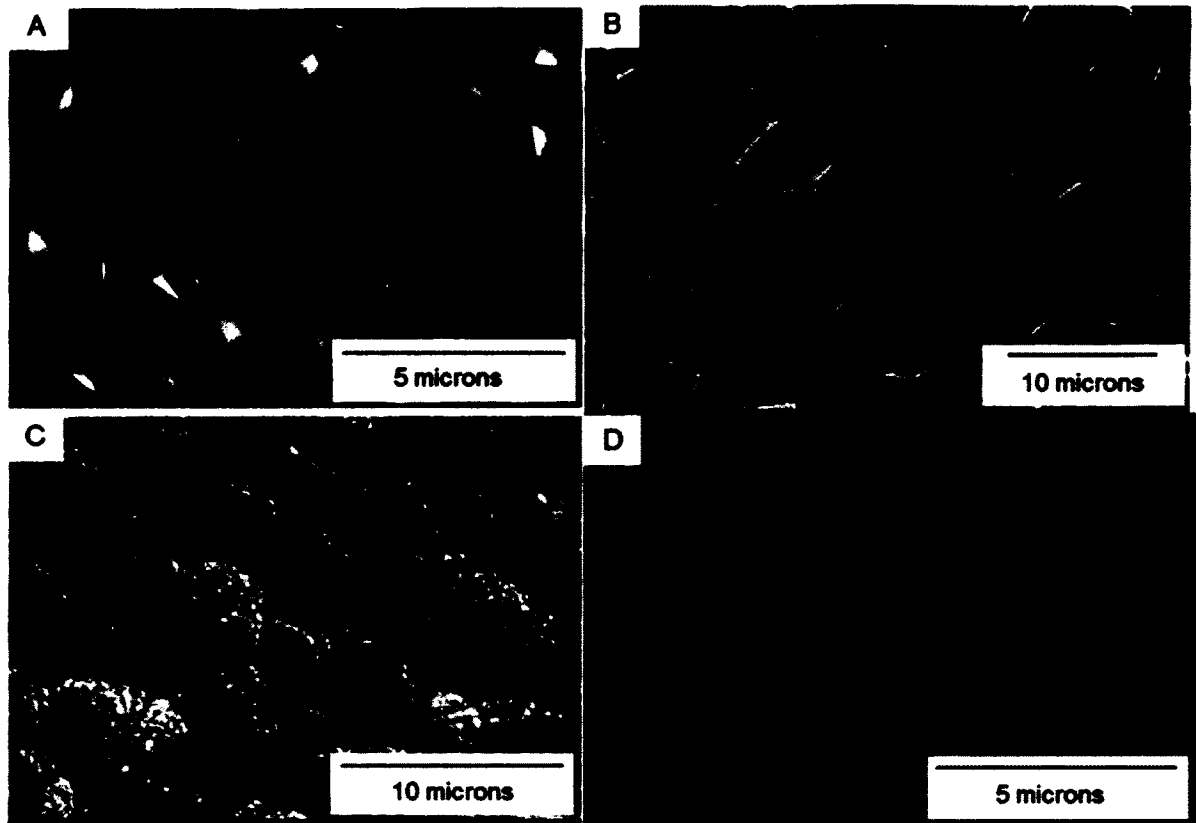


Figure 2-1. Surface morphology of (A) triangular MCD, (B) rectangular MCD film, (C) cauliflower morphology MCD film, and (D) an NCD film.

2.2.1 Synthesis of microcrystalline diamond (MCD) and nanocrystalline diamond (NCD)

For the growth of diamond thin film on non-diamond substrates, substrates are first seeded with diamond micro and nano particles [25-27, 29-45]. This enhances the nucleation of diamond grains [44]. Next, the diamond films (MCD or NCD) are grown on the non-diamond substrate via hot filament chemical vapor deposition (HFCVD) or

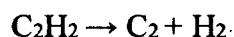
microwave plasma-enhanced chemical vapor deposition (MWCVD) via hydrogen-rich gas mixture (hydrogen with hydrocarbon, usually methane) [41, 44]. The growth of MCD thin film is carried out in hydrogen (>98%) and methane (0.1 - 0.4%) at 600 °C to 1000 °C. This typically generates MCD films with 0.1 to 5 μm wide grains and columnar microstructure which is typically seen when 1% CH_4 is present. The use of non-agglomerating diamond micro or nanoparticles is important to create a high seeding density ($> 10^{11} / \text{cm}^2$). Low nucleation densities ($< 10^{10} / \text{cm}^2$) result in MCD films with rough and highly faceted morphology while the root mean square (RMS) roughness is typically up to 10% of the film thickness. Nucleation densities greater than $10^{12} / \text{cm}^2$ were achieved using optimized seeding process [46] result in formation of NCD films with a relatively smooth and high surface coverage [44, 47].

The growth of MCD and NCD is driven by the CH_4/H_2 chemistry. Following the seeding process, the growth of MCD and NCD is typically homoepitaxial (twinning and defect formation) on the seeds with some non-diamond carbon incorporated in the grain boundaries. The principal diamond growth species are $\text{CH}_3\cdot$ radicals [45, 48]. The atomic hydrogen drives the hydrogen abstraction reactions that prepare the $\text{CH}_3\cdot$ radicals by removing one hydrogen atom from CH_4 to form $\text{CH}_3\cdot$ and move it into a nearby site at the corresponding diamond lattice. Plasma containing 98% to 99% of the hydrogen results in diamond films that are largely free of secondary phase non-diamond material as the atomic hydrogen will etch the co-deposited undesirable graphitic or amorphous carbon phase on the substrate. However, the presence of atomic hydrogen will continuously etch the diamond at a much lower rate (up to 50 times lower), even that, it will result a larger surface roughness and the formation of intergranular voids and

columnar morphology with grain size larger than 1 μm [40, 44]. The NCD film with reduced grain size (10 to 100 nm) can be grown by increasing the ratio of CH_4/H_2 in the plasma which will result a smoother surface profile than MCD film, even though, this outcome could be accomplished at the cost of increased non-diamond components at the grain boundaries [49, 50]. Another class of NCD film with high sp^3 content [44, 51] can be grown by a relatively low ratio of CH_4 (0.3%)/ H_2 with a special diamond seeding treatment [46]. However, the limitation of this class of NCD is only a few hundreds of nanometer film thickness which can be surpassed by increasing the film thickness, though in consequence, the surface roughness increases significantly.

2.2.2 Syndissertation of ultra nanocrystalline diamond

There is a class of nanocrystalline diamond which is grown in an Ar-rich/ CH_4 gas mixture without the presence of hydrogen via microwave plasma-enhanced chemical vapor deposition system. This chemistry produces carbon dimers (C_2) in the plasma, derived by thermal decomposition via the reactions below:



The carbon dimer has been purported to play a critical role in the UNCD nucleation and growth process, while the plasma creates a complex mixture of carbon dimers and hydrocarbon species $\text{CH}_3\cdot$ radicals [30, 52]. The activation energy of carbon dimers has been predicted to be as low as 6 kcal/mol by calculations. The lower the activation energy of carbon dimers makes it easier for the insertion into the surface of the growing film, thus establishing the growth characteristic of UNCD. Recent modeling

indicated the species of UNCD growth which may contain not only carbon dimer, but also some other hydrocarbons because when the carbon dimer concentration in the plasma is high, it will be low at the surface [53, 54]. The relatively low concentration of atomic hydrogen in the plasma arises mainly from the thermal decomposition of methane to acetylene (about 1.5%), which also play a key role in this growing process. The growth of UNCD film can achieve a high-linear growth rate as the formation of continuous films have low thickness due to the lack of the atomic hydrogen minimizing regasification of very small grains. The typical UNCD thin film growth happens as low as 350 to 400 °C with up to 100 sccm of 1% CH₄/99% Ar mixture at 100 to 200 Torr.

The unique film nanostructure of UNCD consists of 3 to 5 nm grains having pure sp³ bonded carbon, 0.4 to 0.5 nm wide high energy grain boundaries with an ultra-smooth grown surface (4 – 6 nm) due to its nucleation and growth process. The grain boundaries which consist of a mixture of sp³, sp² and other types of high energy bondings, have been studied in detail and those high energy grain boundaries are more mechanically stable than the low energy grain boundaries in MCD. The UV Raman spectroscopy [55] and synchrotron based near-edge X-ray absorption fine structure measurements [56] show the presence of the sp² bonding in a typical UNCD film which is about 5%. When the optimized seeding process is introduced, the grown UNCD film had 7 – 10 nm grain size and 1 – 2 nm grain boundaries with the existing of nitrogen in the gas mixture. It is believed that the nitrogen was incorporated at the grain boundaries which was promoting sp² bonds formation as shown in TEM studies [57], optical measurements and spectral photoconductivity [58]. The UNCD or NCD film can be electrically conductive via nitrogen or boron doping during the film growth process [59-63].

There is a new low-pressure bias-enhanced nucleation and growth process (BEN-BEG) reported by Chen *et al.* [64]. The advantages of the BEN process are comparable which have potentially better seeding efficiency [64], stronger adhesion to the substrate [64-68], and an integrated fully dry nucleation/growth using a plasma process only. The new BEN-BEG process includes the following steps: etching of Si (100) substrate for 10 min in a pure hydrogen plasma under bias to remove any native SiO₂ layer from the surface; and *in-situ* BEN-BEG, the UNCD film is grown in 2.2 kW microwave power at 25 mbar in an MPCVD system with 350 V substrate bias and 850 °C as substrate temperature using H₂ (93%)/CH₄ (7%) as grown species with growth rate up to 1 µm/h. The BEN-BEG process yields films with low stress, smooth surfaces (up to 4 – 6 nm) and uniform grain size (3 – 5 nm) throughout the whole film area that makes them potential candidate materials for fabrication of UNCD-based MEMS devices. The main characteristics of these materials are shown in Table. 2-1.

Table 2-1. Characteristics of diamond films.

	MCD	NCD	UNCD
Growth Species	CH ₃ · (H ⁰)	CH ₃ · (H ⁰)	C ₂
Crystallinity	Columnar	Mixed diamond & Non-diamond	Equiaxed diamond
Grain size	0.5 – 10 µm	50 – 100 nm	2 – 5 nm
Surface Roughness	400 nm – 1 µm	50 – 100 nm	20 – 40 nm
Electronic Bonding	sp ³	Up to 50% sp ² (second phase)	2 – 5% sp ² (in Grain Boundaries), 95 – 98% sp ³
Hydrogen Content	< 1%	< 1%	< 1%

2.2.3 Properties of diamond films

2.2.3.1 Mechanical properties

The aforementioned diamond film has some unique sets of complementary mechanical and tribological properties which are extremely well-suited for MEMS devices compared to silicon, as shown in Table 2-2. These properties depend on the nucleation pretreatment method, the surface chemistry and film growth conditions. UNCD films have shown hardness about 98 GPa and Young's modulus of 980 GPa [34] close to the corresponding values for single crystal diamond, 100 GPa and 1200 GPa, respectively. In addition, the hardness and Young's modulus of UNCD films are several times larger than the values of those of silicon. When adding 3% of nitrogen during the UNCD film growth to produce electrically conductive UNCD film, Young's modulus of nitrogen doped UNCD film decreased to about 880 GPa.[34] Further addition of nitrogen (5% to 20%) in the plasma led to a decrease in Young's modulus down to 550 GPa. Adiga *et al.* have reported the Poisson's ratio of hot filament CVD-grown UNCD was about 0.057 ± 0.038 [69] in 2010, which was within the range of single crystal diamond. Those properties would make a better understanding of mechanical-based diamond biosensor design and fabrication.

Table 2-2. Mechanical and tribological properties of Si and UNCD film.

	Density (kg/m ³)	Lattice constant (Å)	Cohesive energy (eV)	Young's modulus (GPa)	Hardness (GPa)
Si	2330	5.43	4.64	165	10
Diamond	3300	3.57	7.36	980	98
	Shear modulus (GPa)	Fracture strength (GPa)	Flexure strength (MPa)	Friction coefficient	Relative wear life
Si	80	1	127.6	0.4-0.6	1.0
Diamond	577	5.3	2944	0.01-0.04	10000

Fracture strength is an important bulk parameter for MEMS devices, especially for the one with moving components, such as cantilever biosensor to make sure it will not break. The fracture strength of UNCD film was measured about five times higher than silicon materials [34]. However, fracture strength of UNCD film is dependent on the nucleation pretreatment used. Espinosa *et al.* has reported the comparison of the influence in fracture strength of UNCD films with two different nucleation methods used: mechanical polishing silicon surface with micron-size diamond powder and ultrasonic agitation of the silicon substrate in an alcohol solution containing nanodiamonds particles [70]. With the ultrasonic seeding process to generate a denser and smoother surface in order to minimize the possibility of defect-prone regions on UNCD film, the fracture strength was in the range of 4.08 – 5.03 GPa comparing to the range of 1.74 – 2.26 GPa, which was using mechanical polished nucleation.

The acoustic velocity (AV) is an important factor for RF MEMS resonators, which is widely used in sensing area.[71, 72] The AV was measured using an atomic force microscope (AFM) on a fixed-free UNCD resonator in vacuum to avoid damping effects due to air [69]. The UNCD film has higher AV comparing with any other

material, 15400 m/s, comparing to 11700 m/s for high-quality AlN and 8100 m/s for single crystal silicon. The high AV and Young's modulus of UNCD film makes it an excellent material for fabricating RF MEMS resonators, which could be operated at a higher frequency for a given geometry or larger devices for a given frequency.

The surface properties of UNCD film exhibited surface inertness, a very stable surface chemistry and low nanoscale adhesion. The surface properties of UNCD film were investigated using surface-sensitive spectroscopies, such as photoelectron emission microscopy coupled with near edge X-ray absorption fine structure spectroscopy, Auger electron spectroscopy and X-ray photoelectron spectroscopy [51, 73, 74]. These experiments could characterize the chemistry and bonding configuration of UNCD surfaces and its effects on adhesion and friction. This information is important for the design and fabrication of reliable and working diamond-based MEMS because the underside of UNCD films may be a part of the tribological interface for given MEMS geometries. UNCD has the lowest coefficient of friction (COF) of 0.01 – 0.05 compare to silicon (0.4 – 0.6), diamond-like carbon (DLC) films (~ 0.2), and MCD films (~ 0.4) [34, 75]. Sumant *et al.* has studied the quantitative information on interfacial adhesion and friction between AFM tip and UNCD film surface using AFM in ambient air before and after H-plasma treatment [73]. The UNCD underside shows a lower work of adhesion (55 mJ/m^2) before H-plasma treatment which is comparable with that of the untreated $\langle 111 \rangle$ diamond surfaces. The UNCD surfaces exposed to H-plasma to etch the non-diamond carbon at the interfaces, left the UNCD surface H-terminated with reduced work of adhesion (10 mJ/m^2). This approached the van der Waals' limit for attraction force between the native oxide surfaces [74]. The friction force measured of UNCD underside

was comparable to that of the untreated diamond <111> surface [73]. The friction force of UNCD reduced due to the H-plasma treatment [74]. With the very low nanoscale adhesion and friction force of the UNCD surface, it makes the understanding that UNCD can significantly outperform Si in surface-machining biosensing applications where surface properties are important for performance.

The surface roughness of the UNCD film which depends on the nucleation density and initial growth, is another important property for MEMS biosensing devices. Different nucleation steps have been established to achieve high seeding density, mechanical polishing, ultrasonic seeding process and bias-enhanced nucleation process. The mechanical polishing silicon substrate with micro- or nanodiamond particles generates a relatively low nucleation density (10^{10} sites/cm²) [44]. The ultrasonic treatment of the substrate in an alcohol solution with diamond nanoparticles resulted higher nucleation density (10^{11} site/cm²) and smoother UNCD film growth, even in the temperature as low as 400 °C [32]. A nucleation method called NNP or “Rotter nucleation technique”, generated an extremely high nucleation density (10^{12} site/cm²) [46]. However, the limitation of this process for MEMS device fabrication is that this process involves an extra plasma treatment and high temperature for nucleation, which will make it difficult for some low temperature materials on the MEMS devices. There was a new nucleation which deposited of 10 nm of tungsten layer on the substrate as a template layer [74]. The tungsten template layer significantly increased the initial nucleation density to lower the surface roughness, eliminating interfacial voids and growth of thinner UNCD film in low temperature. This structural optimization enabled its integration with a wide choice of

substrate materials. All the surface properties of UNCD film indicate that the UNCD film is suitable for MEMS biosensing devices, such as cantilever and resonator biosensors.

2.2.3.2 Electrical, thermal and electrochemical properties

Electrical and electrochemical properties are two important factors for electrochemical biosensing. The electrical properties of undoped diamond, which has a band gap of 5.45 eV, is an ideal electrical insulator material with resistivity in the order of $10^{20} \Omega \cdot \text{cm}$. However, the diamond can be electrically conductive by doping dopants, such as boron, nitrogen and sulfur [76-79]. Boron is the most widely used dopant because of its low charge carrier activation energy of 0.37 eV which will lead diamond to a p-type doping [76]. With the different doping level of boron, the diamond can act as an extrinsic semiconductor to semimetal. In addition, some other dopant, such as nitrogen with charge carrier activation energy of 1.6 – 1.7 eV [76, 77], phosphorus with charge carrier activation energy of 0.6 eV [78, 80], and sulfur [78, 79] can lead an n-type doping in diamonds. Also, diamond thin film can be doped with two dopants at the same time to generate a co-doped diamond surface, such as nitrogen-boron [76] and boron-sulfur co-doping [77, 78]. However, sulfur can only be used as a dopant with the presence of boron, with the low boron doping level, an n-type doping results. Also, with the heavily boron doped CVD diamond can switch its conductivity from p-type to n-type after a deuterium plasma treatment [80]. The conductivity of doped diamond depends on the doping level. For boron doped diamond, the resistivity lays between 5 – 100 $\text{m}\Omega \cdot \text{cm}$ with the doping level from 500 ppm to 10000 ppm [76, 80]. Another disadvantage of diamond electrodes is the low conductivity, the diamond can be electrically conductive with the

different dopants and doping level, which will make its electrical conductivity changing from insulator to semiconductor or even semi-metal [81].

The highest thermal conductivity of diamond among the varieties of carbon materials has been reported, which is above 2000 W/mK at room temperature [82]. However, the thermal conductivity of diamond materials decreases with the decreasing of the grain size of diamond [82]. The sputter-deposited Al, Au, Cr, Cu, Pt and Ti thin film about 200 nm thick, shows as establish Ohmic contact with the surface of diamond, which is critical for electrostatically actuated MEMS application as it will require reliable electrical contact [83]. The high thermal and chemical stability of diamond has been widely reported [14, 81, 84, 85], especially electrochemical stability which has been considered as one of the major advantages of diamond electrodes compared to conventional electrode materials [86]. Doped-diamond was first introduced into electrochemistry by Pleskov *et al.* in 1987 [87]. The electrochemical behavior of diamond in aqueous electrolytes has been studied in the past three decades. The most unique electrochemical property of diamond is the widest potential window around 3.5 V in 0.2 M H₂SO₄ solution, which means it has varying potential for both oxygen and hydrogen evolution [86, 88-91], however, all the diamond electrochemical biosensing devices will not be operated in the extreme environment where phosphate buffer is the most commonly choice to avoid extreme settings.[92] The diamond electrode has larger potential window measured comparing with metals so far in aqueous electrolytes, which makes it a totally different electrode material comparing with gold, platinum or mixed metal oxide. Also, diamond does not encounter surface oxide formation and reduction reactions which are found at conventional metal or metal-oxide electrode materials

between oxygen and hydrogen evolution. However, the electrochemical properties of diamond electrodes depend on the doping level, surface termination and non-diamond carbon content. On the other hand, the electrochemical properties of diamond electrodes in non-aqueous electrolytes are additional important factors in the electrochemical biosensing. The electrochemical biosensing is also widely used in the organic solvent, acetone, acetonitrile, propan-2-ol and tetrahydrofuran.[93-95] Several organic electrolytes have been studied, such as propylene carbonate [96, 97], acetonitrile [97, 98], γ -butyrolactone, N, N-dimethylformamide and diethyl carbonate-propylene carbonate mixture [97]. Boron-doped diamond film electrodes exhibited in a non-aqueous electrolyte with a 1.5 – 2.5 times wider potential window (approximate 5-7.5 V) than in aqueous electrolyte, almost the same as glassy carbon or graphite electrode in the same organic electrolytes [96-98]. The diamond electrodes' electrochemical stability in aqueous and non-aqueous electrolytes makes it a better electrode material for biosensing application. However, there were some reports showing that diamond electrodes were electrochemically etched under certain experimental conditions [91, 99]. Panizza *et al.* has shown a strong decreasing in surface roughness with the electrochemical experiment performed in 1 M H_2SO_4 + 3 M acetic acid with 1 A/cm² at 40 °C [99]. On the other hand, the electric current of electrochemical biosensing would only be hundreds of mA maximum, in such condition, the diamond electrodes would have a very slow losing rate and usually it lasts for years.[99] The diamond electrode will still be attractive for electrochemical biosensing applications because of the relatively slow anodic corrosion rate in electrochemical measurement.

2.2.3.3 Biological properties

For biosensing applications, it is important to tether biomolecules like DNA, aptamers, antibodies, and enzymes or to grow a confluent layer of mammalian cells on the surface of the transducer. Biocompatibility means the material has no toxic or injurious effects for biological systems and the ability of a material to perform a host response in a specific application. In 2002, Yang *et al.* showed that the UV-alkene chemistry of UNCD surface provided a stable covalent bonding to ssDNA for up to 30 cycles compared to gold, silicon, glass and glassy carbon.[39] In contrast, the thiol chemistry on gold, silane chemistry on glass, PEG-O-SiCl₃ chemistry on silicon,[100] and self-assembled lipid or electrooxidation chemistry on glassy carbon[101, 102] showed a decrease in tethered ssDNA from their surface. Similar properties also have been reported on crystalline diamond and MCD films.[103] Hartl *et al.* have shown the enzyme catalase covalently immobilizing on nanocrystalline diamond electrode which was very active and sensitive to the presence of hydrogen peroxide comparing with gold electrode.[104] In 2011, Radadia *et al.* reported the stability of immobilized antibody on UNCD film which can be active approaching 2 weeks in PBS at 37 °C and at least 4 weeks in PBS at 4 °C.[105] These results indicated that protein bonding to diamond was significantly better than other conventional substrates in the long-term bonding stability, which is especially important for biosensing applications in high-throughput systems.

The cell adhesion properties on diamond material, which is an important factor for cell-based biosensing devices and cell monitoring devices, have also been studied in detail in the past decade. The ordered growth of neurons has been demonstrated on a protein-coated diamond surface using microcontact printing, and the neurons survived in

culture for at least 1 week.[106] The neuronal cell excitability and adhesion property on functionalized diamond surfaces has been studied in detail on H-terminated and O-terminated diamond surfaces with rat hippocampal neurons and chick ciliary ganglia by Ariano *et al.*[107] The measurement of cell adhesion force on MCD and UNCD surface has been first measured using atomic force microscopy (AFM) by Chong *et al.*[108] The UV-treated UNCD surface, which has been oxygenated and hydrophobic, showed the highest cell adhesion force and the biocompatibility of UNCD was better than MCD film identified using the cell growth method. Bajaj *et al.* has shown the superior properties of UNCD film in cell growth of different cell lines comparing with other surfaces.[109] Xiao *et al.* reported the *in vitro* and *in vivo* studies of UNCD film by implanting UNCD coated silicon retinal microchips into rabbits' eyes for up to 6 months.[38] The implantable devices fabricated or coated with UNCD film also has been reported in the past years to show the excellent biocompatibility of diamond materials.[110, 111] The cell properties on BDD have been studied with different terminated surface groups and different cell lines and showed the excellent biocompatibility of boron-doped diamond films.[112, 113] All the researches shown above have given a clear evidence of diamond to be an excellent well-suitable material for biosensing applications.

2.3 Micro/Nanofabrication Methods for Diamond Films

2.3.1 Conformal diamond coating

Since diamond has unique mechanical and tribological properties, such as low wear and friction, the thin diamond film can be coated on silicon based MEMS to provide a layer of low friction and low wear. However, before the invention of UNCD growth, conventional diamond CVD deposition was the only method that could provide a

discontinuous thin film with low density of large grain and high surface roughness [114]. On the other hand, UNCD films can be coated at a high aspect ratio MEMS structure, those are even extremely conformal having film thickness up to 10 μm . However, the diamond-coated MEMS may only have the tribological properties of diamond, the mechanical properties may be dominated by the silicon core. Therefore, the conformal diamond coating method can only be used in the specific applications which requires the perfect tribological properties of diamond.

2.3.2 Selective deposition

The second method of diamond devices microfabrication is selective deposition, which has no analogue in Si microfabrication technology. All the surfaces will be needed a seeding process, exposing substrate to the diamond particle suspension, before the diamond growth. In the selective growth process, the substrate can be seeded via three different methods, as shown in Figure 2-2. Figure 2-2A shows the selective deposition process using photoresist to prevent the nucleation of diamond particles on selective area. Figure 2-2B shows the scheme of using diamond-loaded photoresist to generate selective nucleation patterns. And Figure 2-2C shows the process of seeding the whole substrate followed by lithographic patterning to generate selective seeding area. The feature resolution of selective deposition is limited by the grain size.

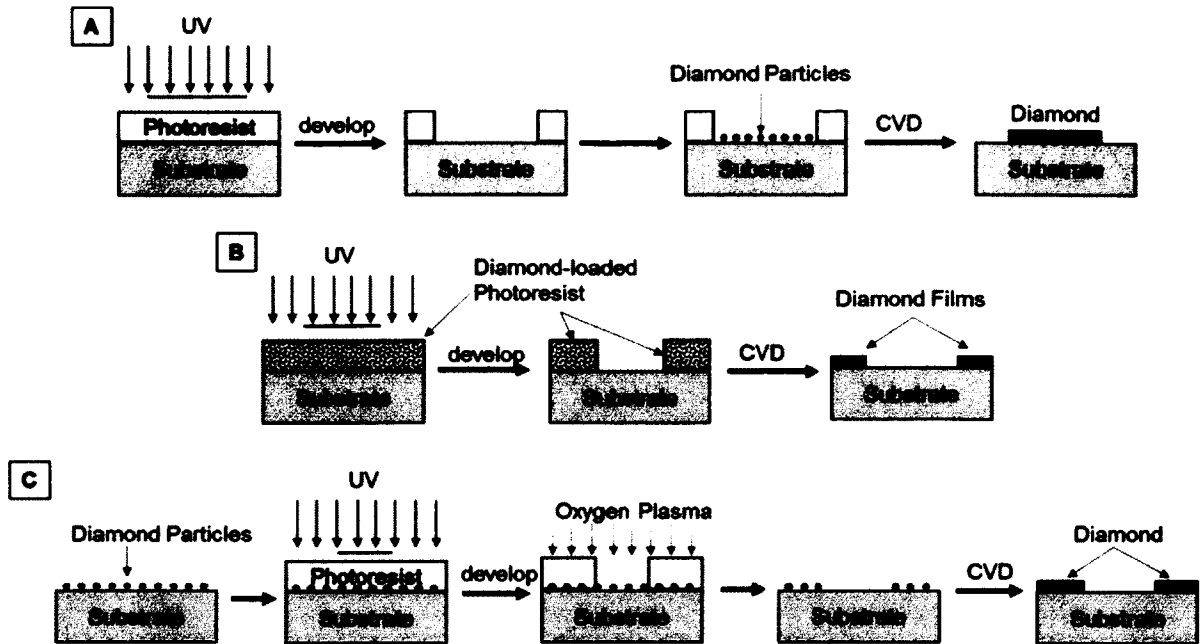


Figure 2-2. Processes of selective deposition of diamond, (A) using photoresist to prevent surface exposing to diamond particles, (B) using diamond-loaded photoresist to produce a pattern of nucleation, and (C) seeding the whole surface and lithographic etch the selective area to generate patterns.

2.3.3 Photolithography and reactive ion etching processes

In this fabrication process, blank UNCD layers are typically grown on a sacrificial release layer, such as thermal or PECVD SiO_2 . As shown in Figure 2-3, the UNCD film will be deposited on another layer of SiO_2 as the mask layer. The lithographic process will introduce the patterns on the SiO_2 mask layer. The UNCD film with patterned mask will follow the reactive ion etching process in oxygen plasma to etch the UNCD layer selectively. At last, the SiO_2 mask layer can be removed by buffered oxide etching.

Due to the high chemical inertness and mechanical strength, the etching steps for diamond MEMS devices become complicated. The most suitable method for etching the diamond thin film is plasma-assisted reactive ion etching (RIE), which includes inductively coupled plasma (ICP), capacitive coupled plasma (CCP), electron cyclotron

resonance (ECR) and ion-beam assisted (IBAE).[115] The ICP-RIE is the most commonly used technique for vertical-like structure etching with a short processing time due to the high density of plasma; however, the high plasma density will cause high temperature on the substrate. There are several reports using ICP-RIE for processing diamond tips and nanoneedles with higher etching rate and anisotropic.[116-120] However, due to the high power of the plasma, the selectivity of the masks and diamond film was varied with the composition of gas mixtures.[117] The advantage of ECR-assisted plasma is low substrate temperature and pressure to generate a very clean structure with sharp edges due to the low microwave power, however, ECR-assisted plasma gives a relatively low etching rate comparing with ICP-RIE.[121] The conventional CCP-RIE has very good control of surface morphology due to the lower etching rate, because of the low ion density and power.[122] Zhang *et al.* processed a diamond cone structure with 28 ° and tip radius of 2 nm using CCP-RIE with single and nano-crystalline diamond.[122] The commonly used active gas species are O₂, CF₄, Ar, and SF₆ for ICP, CCP, and ECR RIE systems.[123] However, the final properties of etched diamond surface strongly depend on the primary surface morphology, gas composition, pressure, reactor type and composition of diamond.[124, 125] The higher power of the RIE system will increase the etching rate of diamond film, but the surface roughness will be increased.[123] In contrast, increasing the pressure of the system will cause the decrease of etching rate significantly.[116, 123] The composition of active gases is an important factor to influence the selectivity between the diamond film and mask where aluminum showed the best selectivity.[126] The conventional masks for diamond etching process are metals, such as Al, Pt, Au, and Ti, silicon nitride and silicon

dioxide.[126] Although selectivity of the silicon dioxide mask is lower than that of Al, the silicon dioxide mask can be used for one step fabrication of needle-like microstructures, such as diamond AFM tips.[118] All the etching methods summarized above need to be chosen accordingly to get the best result for diamond MEMS biosensing device fabrication.

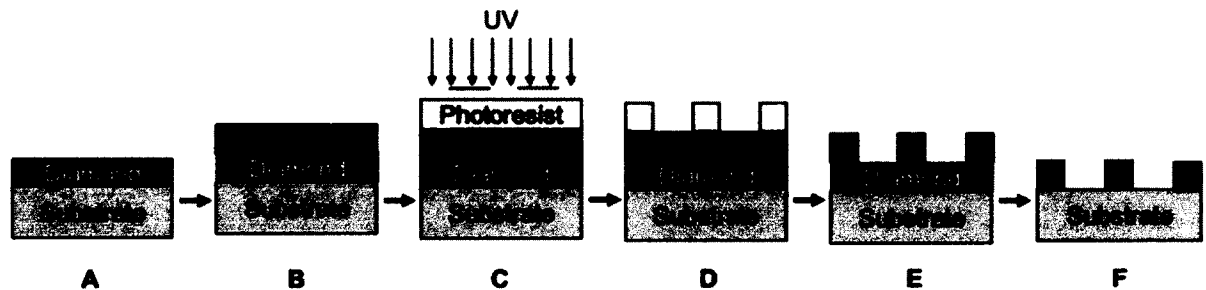


Figure 2-3. Schematic showing lithographically-based microfabrication process of diamond MEMS.

2.4 Functionalization of Diamond Surfaces

For the bio-application of diamond thin films, the surface modification generally addresses two main purposes: the introduction of functional groups and changing surface properties. For the biosensor applications, the immobilization of functional biomolecules, such as DNA, antibodies, enzyme and the reduction of non-specific binding are both important. In another case, the surface modification will also be necessary for increasing the cell adhesion.

The chemical stability of diamond surface has been reported at the first place to repel diamond from bio-applications; however, in the past decade, the research on functionalizing of the diamond surface has started. Since 2002, the diamond surface has been shown which can be modified with DNA, which made a big step in the bio-

application field of diamond. The diamond surface can be modified using different methods, such as plasma, photochemistry, and electrochemistry.

Hydrogen- and oxygen-termination are the most stable terminations of diamond. In the past decades, other terminations of diamond surface, such as F-termination[127, 128], Cl-termination[128, 129], and amine-termination[128], have been reported.

2.4.1 Surface terminations

As-produced diamond thin film has an H-terminated surface, which will be stable in air and aqueous electrolyte at least for a month, due to the hydrogen containing atmosphere in the diamond growth process.[76, 86, 130] Also, the O-terminated diamond surface can be reduced in a cathodic treatment in acidic aqueous electrolyte to generate H-termination surface.[131] A hydrogen plasma treatment will also lead the diamond surface to a H-termination.[130] The H-termination diamond surface shows hydrophobic properties, with a typical contact angle of around 90°.[76, 86, 90, 130] The most important property of the H-terminated diamond surface is its surface conductivity, which enables the design of diamond biosensors based on H-terminated surfaces. The H-terminated diamond surface can be used directly for biosensing application without further surface modifications. The as-deposit H-termination diamond electrode can electrochemically detect oxalic acid with a linear response range of 0.05 – 10 μM and detection limit of 0.5 μM . [132] The electrochemical detection of L-cysteine (CySH), which plays a crucial role in biological systems, has been reported using H-termination diamond electrodes with a higher sensitivity down to 21 nM compared to glassy carbon electrode.[133] The O-terminated surfaces can be obtained with different methods, such as oxygen plasma, ozone exposure, wet oxidation and anodic electrochemical oxidation.

The nature of these O-termination surfaces depends on the methods of the oxidation process, the surface orientation and the ratio of sp^2/sp^3 . The H-terminated diamond surface can be modified into O-terminated surface which shows a hydrophilic property, having contact angle below 5° , during an anodic oxidation treatment in aqueous electrolyte.[76, 91, 130, 134] This anodic oxidation process also could remove the non-diamond sp^2 carbon impurities on the as-deposit diamond surfaces.[91, 130, 135-137] In addition, a short oxygen plasma treatment would also lead to oxygen containing functional groups on the diamond surfaces.[138] Although, the report shows the oxygen-termination happened naturally on H-termination diamond surfaces stored in air.[137] The surface conductivity vanishes after the O-termination from the surfaces, which has been inspected an easy method for the fabrication of conductive/non-conductive patterns at the surfaces for biosensing applications. Fujishima's group has shown the electrochemical selective detection of dopamine (DA) in the presence of ascorbic acid (AA) with a very low detection limit of 50 nM using O-terminated diamond electrodes.[139]

The diamond surface can be modified to fluorination-termination in an RF-plasma with CF_4/He atmosphere for a short time, although it has not been attracted much attention.[140] The F-terminated diamond surface will lead to an extraordinary hydrophobic surface property and larger potential window in aqueous electrolyte.[141, 142] In addition, the high hydrophobicity of F-terminated electrodes is extremely useful for tribological applications, and controlling adsorption of biomolecules. Also, the F-terminated diamond surface can further be biofunctionalized with the C-reactive proteins with 3900 of signal-to-noise ratio in ELISA assay.[143]

A Cl-termination surface can be obtained by plasma, photochemical or thermal decomposition of Cl-containing gases.[128, 129, 144] The Cl-termination surface is also hydrophobic, but the stability is a significant issue. The C-Cl surfaces can react in air or water to form C-OH, which can be used as an intermedia state for other surface functionalization.[128, 145]

Amine-termination has been believed as the most attractive termination for diamond bio-application because it can be linked with bio-molecules, such as DNA, antibody, enzyme and other proteins. The amine-termination can be obtained by exposing Cl-termination or H-termination surface to NH_3 gas under UV irradiation.[128] In addition, the amine-terminated surface is very sensitive to the changing of pH.

2.4.2 Photochemical methods of functionalizing diamond surfaces

The largest amount of research on functionalization of diamond surface are based on the H-terminated diamond surfaces, although some reports are show functionalization of O-terminated surfaces. There are three main methods of functionalizing diamond surfaces: photochemical, electrochemical and chemical methods. For the O-terminated diamond surface functionalization, only chemical methods are reported.

When Takahashi *et al.* has first introduced a photochemical of chlorination, animation and carboxylation process of the as-grown H-terminated diamond surface, it was a giant step of biofunctionalization of diamond.[146, 147] The mechanism of this photochemical method is based on the reactivity of alkene molecules with a termination of double bond towards H-terminated surfaces with the illumination of UV-light, typical 254 nm, as shown in Figure 2-4. The grafting process was believed to occur in the following steps: first, electron injected from the diamond surfaces in the liquid phase of

alkene, then formation is done of reactive species such as radicals and a last step was surface reactions. The electron from defect states were photoexcited into the conduction band and due to the negative electron affinity of H-terminated diamond surfaces, electrons can be ejected to the liquid phase.[148] Although, Shin *et al.*, suggested that electron were directly excited from the valence band of diamond into the molecular acceptor level of the alkene molecule.[149] In 2002, Yang *et al.* reported a new super stable photochemistry to modify nanocrystalline diamond surfaces using alkenes, followed by electrochemical reduction of diazonium salts for immobilizing DNA.[39] In addition, Radadia *et al.* reported photochemically grafting UNCD film with Trifluoroacetamide protected 10-aminodec-1-ene (TFAAD) following with deprotection of NaBH₄ and reduction of glutaraldehyde to immobilize antibodies with a stability at least for 2 weeks storing in PBS at 37 °C.[105] A one step amine modification on polycrystalline diamond has been demonstrated by exposing diamond surface to UV irradiation with the presence of ammonia gas.[150] Bouvier *et al.* reported that the diamond surfaces can be treated with ammonia plasma to generate amin-terminated surfaces.[151]

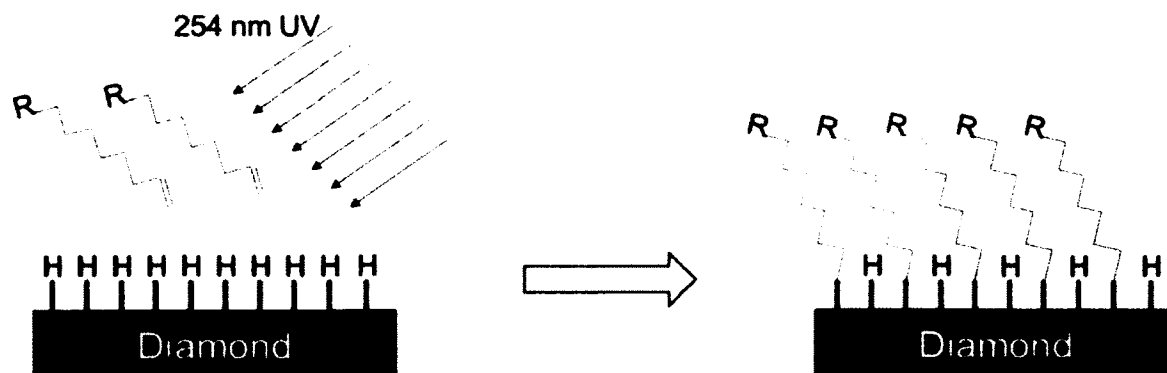


Figure 2-4. 254 nm UV-light photochemical functionalization of H-terminated diamond using alkene molecules.

2.4.3 Electrochemical method of functionalized diamond

In 1999, Swain *et al.* reported for the first time on the covalent grafting of aromatic groups to diamond surfaces by electrochemical reduction of phenyl diazonium salts in acetonitrile using boron-doped diamond electrodes, as shown in Figure 2-5.[152] The electrochemical modification was typically carried out in the water-free solutions with electrical conductive diamond electrodes which could provide electrons during the anodic polarization to reduce the diazonium ion, such as an organic solution. The electron from diamond electrodes induced the electrochemical reduction of diazonium ions forming aryl radicals and nitrogen molecule, followed by covalent bonding of the aryl radical to the diamond electrodes surface after hydrogen abstraction. Electrochemical surface modification of boron-doped diamond has also been carried out in organic solvent and generated amine group on diamond surfaces with the presence of 3-aminopropyltriethoxysilane.[153, 154] Although, most of the research was carried out using H-terminated diamond electrodes, Uetsuka *et al.* reported the electrochemical

functionalization with O-terminated diamond electrodes with the formation of multilayers.[155]

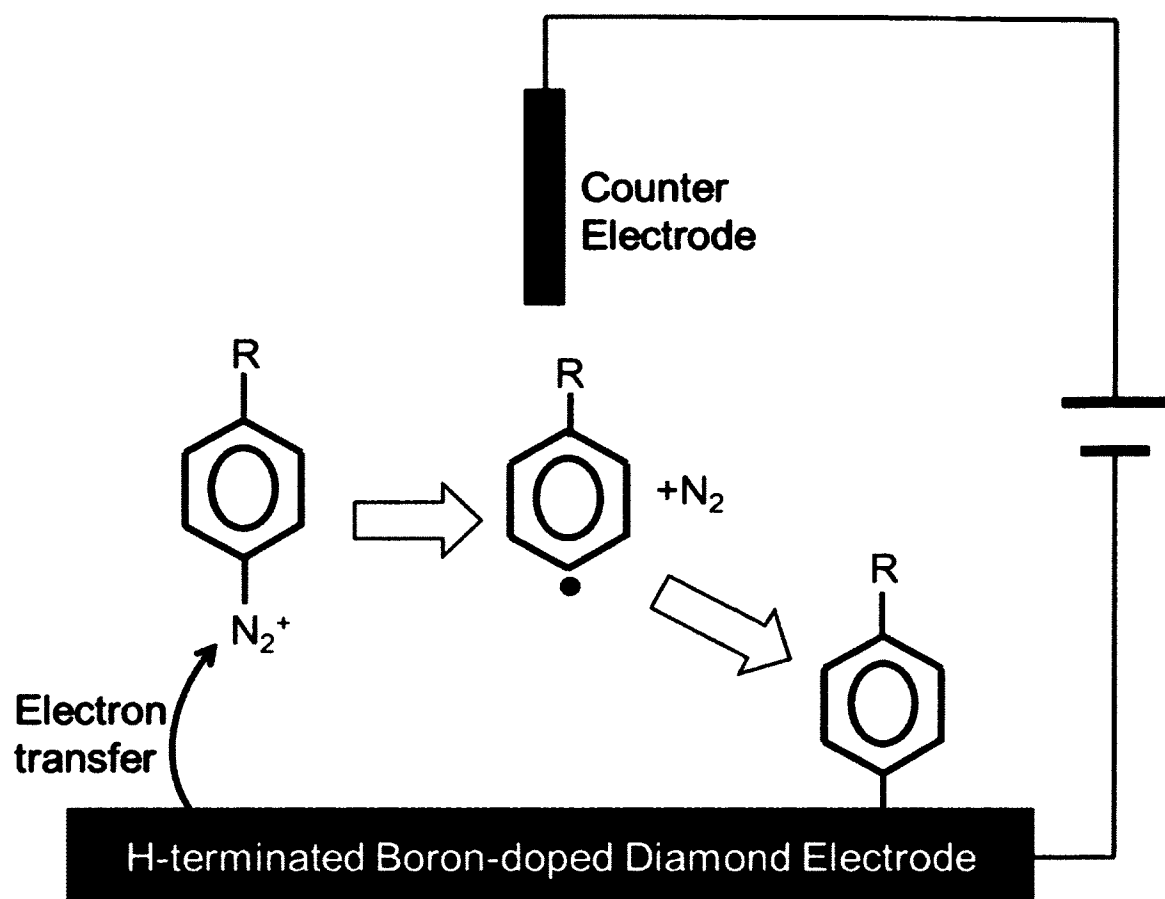


Figure 2-5. Electrochemical functionalization of diamond electrodes using aryl diazonium molecules.

2.4.4 Chemical functionalization of H-terminated diamond surfaces

The high chemical stability of diamond becomes an important issue for the surface modification of diamond, until photochemical and electrochemical modifications are invented. However, since 2005, the spontaneous grafting of diazonium salts to diamond surface has been reported.[156, 157] Figure 2-6 shows the reaction scheme of the spontaneous grafting of diazonium salts process. In order to reduce the diazonium

salts, the diamond surface has to be the reducing agent to provide electrons. Biphenyl radicals can abstract hydrogen from the diamond surface, which allow the reaction of the dangling bond with another radical. In the case of electrochemical grafting, electrons can be supplied during the cathodic polarization; however, in spontaneous grafting, no polarization is required. The grafting efficiency strongly depended on the reducing capacity of the diamond, the extremely long reaction, up to 72 hours to form a monolayer coverage, was reported by Andenier *et al.* [156] This spontaneous grafting process can be used for anchoring biomolecules on the diamond surface for biosensing application.

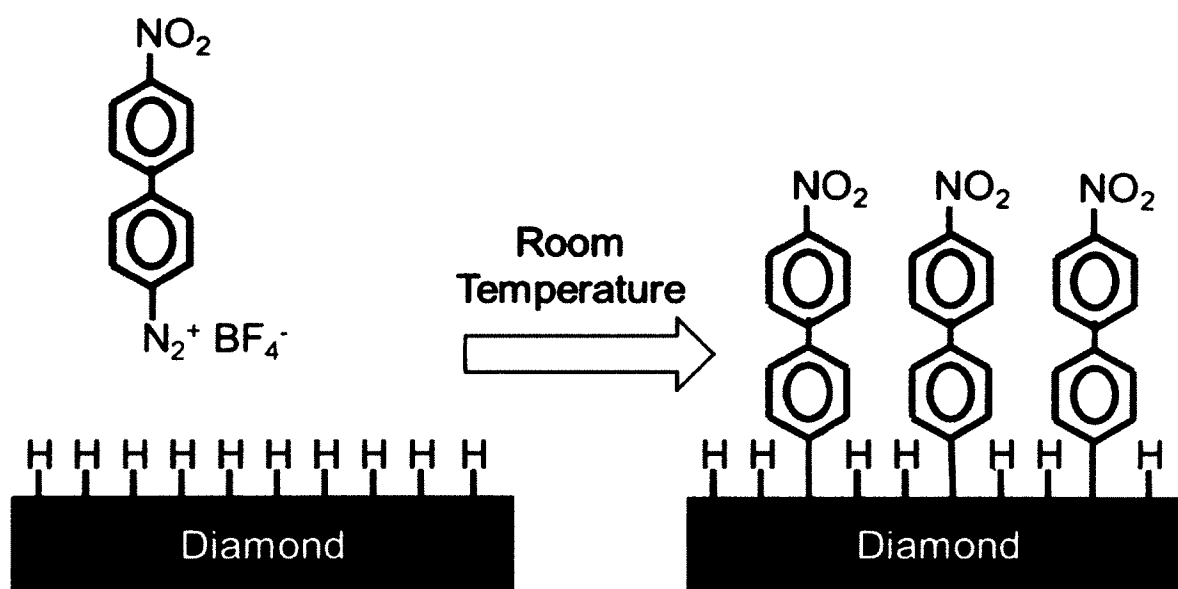


Figure 2-6. Reaction scheme of the spontaneous grafting process.

2.5 Diamond Surface for MEMS Biosensing Applications

Since the diamond thin films have some special properties, such as a wide potential window in aqueous and non-aqueous solution, low and stable voltammetric and amperometric background current, reversible to quasi-reversible electron transfer kinetic

for several inorganic redox systems, extreme corrosion resistance to strong acids and other corrosive environments, morphological and microstructural stability at extreme anodic and cathodic potentials, long-term response stability, and biocompatibility. Those excellent properties have made diamond an ideal candidate for the MEMS biosensing applications. Numerous examples of diamond biosensors have already been developed. Electrochemical biosensors, mechanical-based biosensors and optical biosensors will be described.

2.5.1 Diamond thin film for electrochemical biosensor applications

For the electrochemical biosensors, the substance of interest is concentrated at the electrode surface. The amperometric current associated with a redox process, which is involved with diffusion between the bulk solution and the electrode surface, is measured during the voltammetric swapping process. The detection limit for this electrochemical biosensing technique is about the maximum measurable current which is limited by the rate of bulk diffusion to the electrode surface. There are numerous examples in the literature of sensing of biomolecules using diamond as electrode material or electrode coating material. With different surface termination properties of diamond, most of the termination can be used directly as an electrode material for biosensing, such as H-termination, O-termination, carboxyl-termination, and amine-termination.

2.5.1.1 Electrochemical biosensing using H-terminated diamond electrodes

The as-deposited diamond electrodes with H-termination have high stability and sensitivity for analysis of a number of biological species. Ivandini *et al.* reported oxalic acid could be electrochemically detected with well-defined peaks of oxalic acid oxidation. And the linear response range of 0.05 – 10 μM with a detection limit of 0.5

nM has been reported.[132] Moreover, for the same case, no peak was observed using O-terminated diamond electrodes within the cycling potential, which propounded different surface properties with highly controlled electrochemical reactions. Spataru *et al.* reported the voltammetric detection and quantification of L-cysteine (CySH), which is a sulfur-containing amino acid and plays crucial roles in biological systems, using H-terminated BDD electrodes with a linear dynamic range of 0.1 – 100 μM and a detection limit of 21 nM at signal to noise ratio (S/N) of 3.[133] In 2014, Sochr *et al.* has developed a simple and sensitive square-wave voltammetric method for the detection of adrenaline in human urine using unmodified BDD electrodes with a linear detection range of 0.7 to 60 μM and detection limit of 0.21 μM . [158] Also, H-terminated diamond electrodes also showed advantages for electrochemical detection of other biological compounds, especially for negative-charged molecules, such as nicotinamide adenine dinucleotide (NADH) [159, 160], biogenic amines [161], glucose [162-164], Tyr [165] and Hb [166].

2.5.1.2 Electrochemical biosensing using O-terminated diamond

On the other hand, some of the biological species are more suitable for detection with O-terminated diamond electrodes. Dopamine (DA) for instance, is an important neurotransmitter in mammalian central nervous system. The biosensing of DA has been widely reported using carbon nanotubes [167], AuNPs [168], and polymer thin films [169]. However, these materials encountered problems, such as long-term stability and complicated preparation steps. With the O-terminated diamond electrodes, Fujishima's group reported the highly selective detection of DA with the presence of Ascorbic Acid (AA) with a detection limit of 50 nM (S/N = 3), in addition, the O-terminated diamond

surface showed a better sensitivity and selectivity than H-terminated diamond electrodes.[139] The possible explanation is that the O-terminated BDD electrodes acquire surface dipoles as a result of introducing C=O functional groups, which electrostatically repel the oxygen-containing groups on AA with strong dipoles. In 2014, an integration of diamond microelectrodes and CMOS based electrochemical biosensor for detection of histamine and dopamine has been developed by Hayasaka *et al.*, which offers real-time 2-D imaging of histamine diffusion in a solution.[170] In addition, some of other biomolecule can be electrochemically detected by O-terminated diamond electrodes, such as uric acid [171] and glutathione[172].

2.5.1.3 Electrochemical biosensing with biomolecule functionalized diamond surfaces

For most of the electrochemical biosensor, a layer of receptor has to be immobilized on the diamond electrodes to recognize the target biomolecules. Such receptors can be DNA, antibody, aptamer, enzyme or other kind of proteins. As discussed in the previous chapter, the biomolecules can be immobilized on the diamond electrodes by photochemical, electrochemical, chemical and surface absorption; however, surface absorption is not as stable as other covalent bonding. For the electrochemical biosensing application, the applied voltage is critical because the covalent linker can be destroyed by high voltage. Since 2002, Yang *et al.* investigated the stability of covalent bonding of DNA on the diamond surface, it made a big step for DNA-based electrochemical biosensing. Most commonly used DNA detection method is based on DNA hybridizing events. The probe ss-DNA needs to be immobilized on the diamond surface for the recognition of the target ss-DNA. Such DNA electrochemical biosensing method can be used for the detection of bacterial, virus and cancer cells. As shown in Figure 2-7, the

schematic DNA hybridization electrochemical detection mechanism using $\text{Fe}(\text{CN})_6^{3-/4-}$ as mediator redox molecules. In the case of the ss-DNA probe immobilized on the diamond electrode surface, mediator redox molecules are introduced, which can diffuse through the ss-DNA probe layer. When the negatively charged redox molecules diffuse through the layer of ss-DNA and interact with the diamond surface to generate a redox current. After the probe ss-DNA hybridized with target ss-DNA to form ds-DNA, the space between individual ds-DNA molecules becomes too small for the redox molecules to reduce the redox current, which can be electrochemically detected. In 2004, Yang *et al.* reported the electrochemical detection of DNA hybridization events using $\text{Fe}(\text{CN})_6^{3-/4-}$ as mediator redox molecules. The diamond electrodes were functionalized with ss-DNA, and a significant decrease of redox current was detected. In the past decade, a numerous literature reported the electrochemical detection of DNA.[173-177] For instance, in 2012, Liu *et al.* has developed a electrochemical biosensor for the detection of DNA hybridization, such diamond biosensor surface was modified with zirconia to enhance the performance.[177] Recently, a DNA electrochemical BDD biosensor has been developed, such biosensor incorporated immobilized ds-DNA as molecular recognition elements to monitor the *in situ* specific binding process with ds-DNA. It could screen and evaluate the effect caused to DNA by radical and health hazardous compounds.[175] Due to the better understanding of the electrochemical properties of biomolecules, electrochemical biosensors with microelectrodes have taken a big step not only for the detection of DNA, but also for some other biomolecule with a detection limit down μM , or even nM , such as L-phenylalanine, L-tyrosine[178], tobramycin[179], acetylcholinesterase (AChE), methyl

parathion[180], captopril[181], urea[182], glucose[183-185], human IgE[186], dopamine[187], and more.

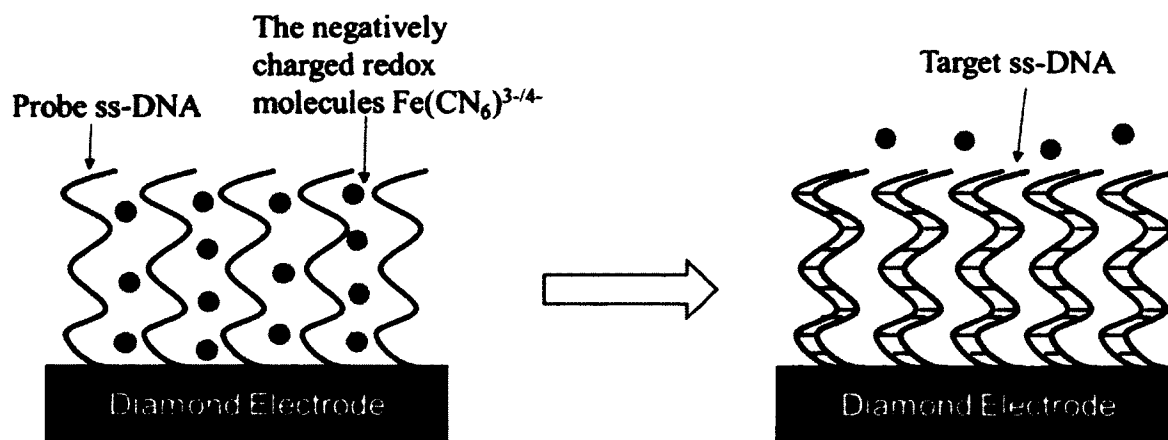


Figure 2-7. Schematic DNA hybridization detection mechanism using $\text{Fe}(\text{CN})_6^{3-/4-}$ as mediator redox molecules.

2.5.1.4 Electrochemical biosensing using nanostructured diamond electrodes

In order to reach even a lower detection limit, such as 10^4 cells/ml of bacteria the bare diamond electrodes cannot meet the requirement. There are several literature published in the recent year to report some alternative ways of modification of diamond electrode to improve the sensitivity of biosensing. In 2014, Rismetov *et al.* has developed an electrochemical biosensor based on the Pt-deposited BDD electrodes for the detection of hydrogen peroxide with a detection limit of $0.51 \mu\text{g/ml}$. [188] In 2014, an integration of diamond microelectrodes and CMOS based electrochemical biosensor for detection of histamine and dopamine which offered real-time 2-D imaging of histamine diffusion in a solution. [170] In 2014, Dai *et al.* reported an amperometric biosensor based on the nanoporous nickel modified BDD electrode with excellent stability and reproducibility of determination of L-alanine in the linear range of $0.5 - 4.5 \mu\text{M}$. [189] In 2012, a non-enzymatic glucose electrochemical biosensor was developed using $\text{Cu}(\text{OH})_2$ nanowire

coated with boron-doped diamond film, where the $\text{Cu}(\text{OH})_2/\text{BDD}$ electrodes gave a linear detection range of 0 to 6 mM with a detection limit of 9 μM . [190] In 2012, an electrochemical biosensor for fast detection of phenols has been developed with a detection limit of 0.07 μM , tyrosinase immobilized AuNPs modified BDD electrodes were used. [191] In 2011, BDD thin film electrodes modified with Pt-NPs dispersed graphene glucose biosensor have been reported with a wider linear range, a lower detection limit and a higher sensitivity comparing with other amperometric graphene-based biosensors. [192] In 2011, a BDD thin biosensor electrodes were modified with Pt-NPs to improve the electrical performance of the electrodes. Such Pt-NPs decorated biosensors showed a higher sensitivity, a lower detection limit and good stability. [193] In 2010, Song *et al.* reported a BDD-based glucose biosensor where electrodes were decorated with Pt-NPs-polyaniline to improve the electrochemical response. Such biosensors exhibited an excellent response to glucose with a wide linear range from 5.9 μM to 510 μM and a low detection limit of 0.1 μM . [194] In recent years, the biosensing activities are not only performed in the ideal environment, such as PBS buffer, there are also some reports showed the detection of biomolecules in some clinical sample, such as urine samples [158, 182] and serum samples. In 2014, Skoog *et al.* has reported titanium alloy microneedles coated with nitrogen incorporated ultra nanocrystalline diamond (N-UNCD) film, which improved mechanical strength, hardness, biocompatibility and electrochemical stability, to perform *in vitro* electrochemical biosensing of uric acid and dopamine. [195] In 2013, Picollo *et al.* reported an amperometric single crystalline diamond biosensor for the detection of quantal catecholamine secretion from individual cell. [196] In 2012, an amperometric biosensor made with a single crystalline diamond for

the detection and quantification of L-lysine in the serum sample and pharmaceutical compounds with a linear concentration range of 1 to 100 nM and a detection limit of 4 pM has been developed by Staden's group.[197] In 2011, Wang's group reported a diamond based MEMS electrochemical biosensor for *in vivo* electrical recording and *in vitro* detecting norepinephrine with a limit of 5 nM.[198]

2.5.1.5 Detection using impedance spectroscopy

In the classes of electrochemical biosensors, impedance spectroscopy biosensor attracted widespread attention due to their potential for real-time and label-free detection. For impedance biosensing, a biomolecule used for target recognition need to be immobilized on the diamond electrodes at the first play, such as DNA, antibody, and aptamer. The impedance change due to the binding of target biomolecule to the sensing biomolecules is rendered as detection. The detection sensitivity depends on a variety of properties: such as electrodes surface properties, functionalization of process and interactions between target and sensing biomolecules. There are two impedance measurement methods: non-faradaic and faradaic. For the non-faradaic method which does not need any redox molecules, the impedance change is mainly due to the change in dielectric properties of the double-layer or the capacitance. This non-faradaic method is especially useful for the on-site diagnostic where surface conductivity is changed due to the specific binding, such as bacterial captured on the surface, or DNA hybridization.[199] In the faradaic method, the change in charge transfer resistance from the presence of redox mediator causes the impedance change. Using these two impedance measurement methods, several kinds of biomolecules have been successfully detected, such as DNA, antigen, antibody and some other biomolecules.

Hamers *et al.* reported a DNA modified BDD surface with ethylene glycol co-immobilized, to reduce non-specific binding of non-target DNA sequences or other biomolecules, using impedance biosensing method to detect a target DNA sequence from complementary and non-complementary samples.[200] Yang *et al.* reported label-free and real-time detection of DNA using diamond electrodes via impedance spectroscopy.[201] In 2007, Vermeeren *et al.* developed an impedance DNA biosensor with BDD electrodes functionalized with ss-DNA to monitor hybridization and denaturing processes with the presence of complementary ss-DNA.[174] Impedance biosensing can also be used in the detection of other molecules. In 2011, Tran *et al.* developed a label-free electrochemical impedance aptamer based diamond biosensor for the detection of human IgE with a linear dynamic range from 0.03 $\mu\text{g/ml}$ to 42.8 $\mu\text{g/ml}$. [186] In addition, Zhu *et al.* reported an impedance spectroscopy based method using undoped diamond film to identify the presence of hemoglobin.[202] In 2011, Weng *et al.* has for the first time developed an electrochemical impedance biosensor made with BDD electrodes which were modified with folic acid immobilized AuNPs. Such biosensor was operated under a constant frequency 10 Hz to perform real-time monitoring of interactions between folate receptor-rich cancer cells and folic acid immobilized on AuNPs.[203] In 2011, Vermeeren *et al.* developed a fast and label-free immunosensor for detection of C-reactive protein (CRP), which was the key factor of the high prevalence of cardiovascular diseases (CVD). Such biosensor was operated at a constant frequency of 100 Hz to measure impedance change in real-time with a detection limit of 10 nM, which was within the physiological relevant concentration range of CRP in health control and CVD patients.[204] In order to better understanding what causes the

changing in the impedance measurement, it is not only focus on the changing in impedance, but also focus more on the equivalent circuit modeling and analyze to distinguish whether the impedance change is from specific detection or poor signal reproducibility. In 2012, Siddiqui *et al.* reported an UNCD microelectrodes array for the detection of *E. coli K12*, and developed a modeling circuit to better understand the reasons of the impedance changing on the electrode surface.[92]

2.5.2 Diamond micro-cantilever based biosensor

In the past decade, with the developing of MEMS fabrication process, micro-cantilever became another type of biosensor. The detection of biomolecules using micro-cantilever can be operated in static mode as well as dynamic mode in the case of detecting DNA [205, 206], biotin - streptavidin and antigen - antibody interactions [207], and bacteria capturing [208]. In the static mode, the cantilever displacement is measured due to the surface stress, mass changing and temperature variation on the cantilever surface. With the dynamic mode, the cantilever resonant frequency change, which was caused by elasticity, mass and temperature change, will be measured. Capacitive actuation, piezoelectric actuation and laser detection can be used for the determination of cantilever displacement and resonant frequency change.[209] The potential possibility of diamond-based micro-cantilever for biosensing application has been investigated in dynamic mode with detailed investigation of sensitivity of frequency change.[210, 211] In addition, Manai *et al.* has reported that the different recognition biomolecule immobilization method would also cause the response sensitivity difference of diamond micro-cantilever biosensor.[212] In 2010, Bongrain *et al.* reported a diamond coated

micro-cantilever biosensing to monitor the hybridization and denaturation of DNA due to the change of cantilever resonant frequency.[213]

2.5.3 Diamond-based field-effect transistor (FET) biosensors

The diamond-based field-effect transistor (FET) has been developed since the beginning of the last decade due to its higher signal-to-noise ratio, good stability and increased sensitivity. In addition, due to the electrochemical properties of diamond, such diamond FET can be operated without the gate oxide. If the pH and concentration of biosensing buffer is controlled, the recognition molecules immobilized on the diamond electrodes were within the Debye length, thus specific binding happened within the measurement range.[214, 215] As a result of specific binding happening within the electrical double layer in buffer solution, a diamond FET could easily detect changes in the charge distribution. Various diamond-based FET biosensor has been developed during the past decade. In 2004, Song *et al.* reported an enzyme surface modified diamond FET biosensor to detect and quantification of glucose with high sensitivity and selectivity.[216] The detection of penicillin using O-terminated diamond FET has been reported.[217-219] The DNA diamond FET biosensor has been widely reported with higher sensitivity, selectivity and detection limit down to 10 pM with different surface modification. [173, 220, 221] The diamond-based FET biosensor achieved a big step that Ruslinda *et al.* reported a diamond-FET-based biosensor with immobilized RNA aptamer for the determination of the presence of HIV-1 Tat protein.[222]

2.6 Summary

The excellent tribology, chemical stability, electrochemical properties and biocompatibility of diamond thin film makes it a suitable material for biosensing

applications. For the biosensing application, the diamond syndissertation will create different surface properties, such as surface morphology and surface terminations. The successful surface modification of diamond makes this a widely chosen material in the biomolecule detection application. To achieve high sensitivity, selectivity and a low detection limit of a diamond biosensor, the surface properties, surface modification and detection mechanism are the most crucial conditions that need to be considered.

Table 2-3 summarizes the different biosensor designs from some of the literatures in the past two decades, sorted with different target biomolecules or cells, a different sensing mechanism and detection limit.

Table 2-3. Diamond biosensor appears in the past two decades and references.

Target Biomolecules	Sensing Mechanism	Detection Limit	Surface Termination	References
Glucose	Spectrophotometric	12 mM	H-terminated	[223]
	FET	-	NH ₂ and O-terminated	[216]
	Electrochemical	13 mM	H-terminated	[162, 164, 224-226]
	Electrochemical	-	Glucose Oxidase covalent modified	[183, 184, 227, 228]
		0.1 μ M	Pt NPs-polyaniline modified	[192, 194]

		9 μ M	Cu(OH) ₂ nanoflower modified	[190]
Dopamine	Electrochemical	-	H-terminated	[139, 159, 187, 195, 229, 230]
NADH	Electrochemical	10 nM	H-terminated	[159, 160]
Uric acid	Electrochemical	15 nM	O-terminated	[195]
Horseradish peroxide	Electrochemical	-	O-terminated	[231]
Chlorophenols	Electrochemical	-	H-terminated	[232]
Theophylline	Electrochemical	-	H-terminated	[232]
L-Cysteine	Electrochemical	-	H-terminated	[133]
Estrogenic phenol derivatives	Electrochemical	1 μ M	Tyrosinase covalent modified	[233-236]
Cl ⁻	Field-effect transistor	-	H-terminated	[237]
2,4,6- trinitrotoluene	Electrochemical	5 ppm	H-terminated	[238]
<i>S. aureus</i> <i>bacteria</i>	ELISA	-	Antibody covalent modified	[239]
Human haemoglobin	Electrochemical	-	H-terminated	[166, 240]
Human haemoglobin	Electrochemical	-	AuNPs modified	[166, 240]
Oxalic acid	Electrochemical	0.5 nM	H-terminated	[132]

DNA	FET	10 pM	DNA covalent modified	[173, 174, 176, 177, 220, 221, 241]
DNA	Impedance Spectroscopy	-	DNA covalent modified	[173, 174, 176, 177, 220, 221, 241]
	Optical&FET	-		
Aspartame	Electrochemical	23 μ M	O-terminated	[242]
Hemoglobin	Electrochemical	0.4 μ M	H-terminated	[202]
Penicillin	FET	5 μ M	O-terminated	[217-219]
Acetylcholinesterase	FET	-	Enzyme covalent modified	[243]
E. coli	Electrochemical	4×10^4 cfu/ml	<i>o</i> -Nitrophenol covalent modified	[244]
Mouse IgG	Electrochemical	10 ng/ml	Anti-mouse IgG covalent modified	[245]
H ₂ O ₂	Electrochemical	0.7 μ M	Cytochrome <i>c</i> covalent modified, HRP covalent modified	[188, 246, 247]
C-reactive protein (CRP)	Capacitor based	25 ng/ml	Anti-CRP covalent modified	[204, 248]
Tyrosine	Electrochemical	-	H-terminated	[165]

Tyrosinase	Electrochemical	-	Polyaniline modified	[191, 249]
Human immunodeficiency virus (HIV)	Optical	-	Aptamer covalent modified	[222, 250]
Human immunodeficiency virus (HIV)	FET	-	Aptamer covalent modified	[222, 250]
Human IgE	Impedance Spectroscopy	0.03 µg/ml	Aptamer covalent modified	[186]
Norepinephrine	Electrochemical	5 nM	Antibody covalent modified	[198]
Folate receptor-rich cancer cells	Impedance Spectroscopy	-	folic acid covalent modified	[203]
L-alanine	Electrochemical	0.5 µM	Nanoporous nickel modified	[189]
Urea	Electrochemical	3.87 mg/dL	Urease	[182]
Adrenaline	Electrochemical	0.21 µM	H-terminated	[158]
Captopril	Electrochemical	0.165 µM	H-terminated	[181]
Acetylcholinesterase	Electrochemical	-	Carbon spheres coated with AuNPs	[180]

CHAPTER 3

NANOSTRUCTURING OF BIOSENSING ELECTRODES WITH NANODIAMONDS FOR ANTIBODY IMMOBILIZATION

3.1 Introduction

Microfabricated biosensor research and application has seen a rapid growth in the last decade exploring a variety of nanomaterials to interface between biomolecules and electronics; although no clear evidence shows an advantage of a specific material.[251] Some of these new nanomaterials include carbon nanotubes,[252-254] gold nanoparticles,[255-257] zinc oxide nanorods,[258] and graphene.[259, 260] In this chapter, the first application of detonation nanodiamonds (NDs) to biosensing electrodes through a seeding process is reported. ND seeded electrodes can be biofunctionalized using previously published UV-alkene surface chemistry of diamond films and used for pathogen detection.[101]

Silicon surfaces and metal oxide nanomaterials have been attractive to create biosensors due to the existing semiconductor infrastructure.[261] However, the widely reported silane chemistry-based for anchoring biosensing molecules on silicon and metal oxide nanomaterial biosensors is susceptible to hydrolysis in biological buffers and hence unstable.[262, 263] In contrast, chemical vapor deposition (CVD) diamond films composed predominantly of sp^3 -hybridized carbon atoms are known to have high chemical inertness, and a wide range of electrical conductivity.[264-266] As an electrochemical electrode, CVD diamond has proven to be highly reproducible, stable

over several months of storage in ambient air, produce low background (noise), and hence better detection limits than the conventional glassy carbon electrodes.[160, 161, 267] Fujishima and co-workers have shown diamond electrodes improve enzymatic biosensing of hydrogen peroxide and bis-phenol A.[231, 233] Hamers and co-workers demonstrated label-free biosensing of protein-protein binding and DNA hybridization using diamond-based impedance biosensors and field-effect transistors.[268, 269] Hartl *et al.* showed that electrons can directly transfer between the redox center of the enzyme catalase and the nitrogen-doped diamond films (n-type, 1-3.33 Ω -cm) with a lower background current and a better stability than gold electrodes.[270] Recently Nebel *et al.* showed that nano-structuring of the diamond electrodes with nanowires extends the electrochemical detection of complimentary DNA down to 10 pM, which is 100 times smaller concentration compared to those demonstrated by gold electrodes.[271] Moreover, CVD diamond films have also been widely reported as biocompatible coatings during multiple *in-vivo* studies on orthopedic [272, 273] and dental implants,[274, 275] and *in-vitro* studies.[109, 276, 277] These findings also imply potential of diamond for cell-based biosensors or *in-vivo* smart implants with sensors.

Additionally, among the many biomolecule immobilization chemistries of CVD diamond surfaces,[266, 278] the UV-alkene chemistry has gained considerable interest, and have been reported to withstand severe hydrolysis conditions and result in better biomolecular stability.[279] During this chemistry, a 254-nm or smaller wavelength UV photon ejects electrons off the diamond surface carbon atoms into the adjacent alkene molecules, leading to covalent attachment of alkenes to the diamond carbon atom by S_N1 reaction mechanism.[280, 281] Using this chemistry, Yang *et al.* have shown improved

stability of DNA-modified diamond films to thermal cycling conditions over DNA-modified silicon, gold, glass, and glassy carbon surfaces.[263] This is because the UV-alkene chemistry results in a hydrolytically stable C-C linkage that is able to withstand 30 times thermal cycling of hybridization-dehybridization of surface bound DNA, while glass, gold and silicon surfaces only lasted for five to ten such cycles.[282] Recently, Radadia *et al.* tested the stability of immobilized antibodies to diamond films using the UV-alkene chemistry.[105, 279] Diamond surface chemistry showed improved temporal stability of antibodies compared to glass surfaces when exposed to saline media at 37 °C for prolonged periods extending up to two weeks. These studies show the potential of using diamond as an interfacing material for biosensor construction.

However, the use of diamond surface for biosensor construction is currently limited by (1) high temperature requirement for growth (~700 °C), hence not allowing deposition on substrates with low melting point such as microscope slides, aluminum or gold, and (2) high costs associated with the CVD process. CVD diamond films are synthesized by seeding a sub-monolayer of high purity monocrystalline NDs as nucleation points, followed by its growth into a continuous film in methane, hydrogen and argon gas flows using a hot filament CVD reactor or a microwave plasma CVD reactor. Thus, in this chapter the process of ND seeding as a means for creating lower-cost biosensors was investigated while leveraging benefits of the UV-alkene chemistry of diamond surfaces.

ND synthesis was discovered as a green chemistry in the late USSR in the 1960s while studying the shock compression of non-diamond carbon modifications in blast chambers. The purification of the resulting mixture leads to colloidal suspensions of

single-digit diamond particles with diameters of 4–5 nm.[283] Development of environmentally friendly purification processes have now allowed high-purity ND powders to be produced in large volumes at a low cost with controlled surface chemistry.[284] Seeding NDs with high density has been an area of high interest in CVD diamond film syndissertation, and it has been explored extensively using sonication, and electrophoretic deposition.[285-288] During the sonication process, the collapse of microscopic cavitation bubbles causes acceleration of nanoparticles towards the substrates and lodges them on the substrate with huge amount of pressure. Shenderova and co-workers provided details of solvent selection and ND concentrations on the coating process and resulting surfaces for CVD diamond growth.[289] Commercially a large ultrasonic batch is used to uniformly seed NDs over the wafer; however, such high power sonication is known to cause milling-induced mechanical damage to the substrate. In contrast electrophoretic deposition can achieve higher surface coverage, but requires a conductive substrate, hence unable to coat insulating substrates such as oxides. Schmidlin and co-workers recently demonstrated deposition of a 5-nm thick dense layer of NDs on highly oriented pyrolytic graphite through electrophoretic deposition from an ultra-centrifuged suspension.[290] New techniques such as layer-by-layer assembly,[291, 292] inkjet printing,[293] and microcontact printing[294] have been reported to increase the seeding density. However, none of these methods have been evaluated by itself as a means to create biosensors. The sonication assisted seeding process is chosen as it allows even coating to non-conformal MEMS surfaces, while the sonication related abrasion was reduced using a bath setup as described in the methods section.

In this chapter, the simplest yet versatile approach of low power sonication-assisted seeding was used, and reported the effect of seeding solvents, concentrations, and time on ND surface coverage, and capture capability as a pathogen sensor. Also, the ND seeding technique was applied to an interdigitated electrode (IDE) array, characterize the changes introduced by ND seeding at the IDEs using impedance spectroscopy, and finally demonstrate label-free pathogen detection upon biofunctionalization of ND-seeded IDEs.

3.2 Methods

3.2.1 Materials

All stock solutions were prepared by deionized water from a Millipore deionization system to obtain minimum resistivity of 18.0 M Ω -cm. Sodium borohydride, 1-dodecene, glutaraldehyde (50%), sodium cyanoborohydride coupling buffer, casein blocking solution, and 3,3'-dihexyloxacabocyanine iodide stain (DiOC6(3)) were bought from Sigma Aldrich. Phosphate-buffered saline (PBS), PBS with Tween 20 (PBS-T20) and bovine serum albumin (BSA) were bought from Bioexpress. Methanol, chloroform, isopropanol alcohol (IPA), and polydimethylsiloxane (PDMS) were obtained from Fisher Scientific. NDs were purchased from International Technology Center in the form of 0.5 w/v% nanocrystalline diamond (Blue seeds) solution. *E.coli* O157:H7 antibodies were bought from Kirkegaard & Perry Laboratories, and anti-*E. coli* O+K FITC conjugate was bought from Pierce Thermo Scientific.

3.2.2 ND seeding and analysis

A silicon wafer with evaporated gold (200 nm Au/25 nm Cr) was diced in to 1-cm x 1-cm pieces that were used as substrates for ND seeding. The as obtained ND solution

consisted of 0.5 w/v% of average 5 nm monocrystalline diamonds in dimethylsulfoxide (DMSO). According to the manufacturer, the NDs were size separated by centrifugation and were found to be within 3-10 nm while the peak of the distribution was around 5 nm. These NDs show a positive zeta potential and DMSO as a solvent provides strong resistance to settling of these NDs.[289] As obtained ND solution was diluted with acetone, ethanol, IPA, methanol or water in 1:1, 1:3, or 1:5 ratio. Brookhavens Instruments ZetaPlus™ was used to measure the zeta potential and make particle size measurements using dynamic light scattering ($\lambda = 660$ nm). The zeta potential calculations were performed using the Smoluchowski equation because the ND particles were of wide size range (10 – 200 nm). The use of Huckel approximation did not change the trend seen in the zeta potential measurements. For sonication treatment, samples were immersed in ND-containing solutions in a tightly sealed 20 ml scintillation vial, and the vials were placed in a Branson 5510 sonication bath (40 kHz, 185 W) equipped with a stainless steel basket. A very low power sonication approach has been used as opposed to the relatively high sonication power immersion horns used commercially. This way the abrasion of gold electrodes was reduced. After sonication for the required amount of time, the seeded substrates were cleaned with methanol, deionized water, isopropyl alcohol, and blow-dried with nitrogen. Surface morphology of a nanocrystalline diamond seeded surface was investigated using Hitachi S-4800 field emission scanning electron microscopy (SEM) and further 2D fast Fourier transform filtering of the SEM images using the Gwyddion software package.

3.2.3 Functionalization of NDs

Some of the ND seeded surfaces were reduced in 65 mM sodium borohydride solution in methanol at 70 °C for 6 hours. Trifluoroacetamide protected 10-aminodec-1-ene (TFAAD) was mixed with 1-dodecene in 2:1 ratio (v/v) to form the functionalization mix. The 1-dodecene spaces the TFAAD molecules and enhances the efficiency of deprotection in the subsequent step to UV-functionalization. The photochemistry attachment was carried out in a nitrogen purged reaction chamber. Functionalization mix at about 2 $\mu\text{l}/\text{cm}^2$ was applied uniformly between the ND seeded surface and a piranha-cleaned quartz slide, then radiated with 254 nm UV at $\sim 2 \text{ mW}/\text{cm}^2$ for 6 hours. Excess reaction mix was removed by sonication in chloroform and IPA for 5 minutes each. The trifluoroacetic acid group from the functionalized surfaces was deprotected in a tight-sealed vial containing 65 mM sodium borohydride in anhydrous methanol for 6 hours at 70 °C.[295] The sample was then rinsed with deionized water and dried with nitrogen and the primary amine groups on the sample surface were then reacted with glutaraldehyde in a sodium cyanoborohydride coupling buffer at room temperature for 4 hours to yield an aldehyde termination by reductive amination.[296] The aldehyde terminated surface was rinsed with deionized water and dried with nitrogen. The functionalized surface was incubated for 18-22 hours at 4 °C with a 100 $\mu\text{g}/\text{ml}$ antibody solution, which was printed using a Nano-eNabler™. The Nano eNabler™ uses microcantilevers containing a microfluidic channel that delivers solutions from the reservoir to the tip. Tips that had 30-micron wide channels was used. After printing, a PDMS well was placed over the printed region and a coverslip to prevent evaporation. On the next day, the wells were washed with PBS-T20 twice and PBS once to remove non-specifically adsorbed antibodies.

Further non-specific binding sites were blocked with a casein-blocking buffer for 1 hour at room temperature. The well was then washed again with PBS-T20 twice and PBS once to remove excess casein.

3.2.4 Fluorescent labeling of bacteria

E. coli O157:H7 was inoculated in Luria-Bertani broth (LB) at 37 °C for 12 hours. Based on plating culture at the 12th hour, all bacteria were found to reach a stationary phase of growth. The concentration of the labeled culture was estimated by agar plating of the 10⁻⁵ and 10⁻⁶ dilution. Culture at the 12th hour was washed with a phosphate saline buffer (PBS) through pelleting (12k rpm, 2 min) and suspension in fresh PBS. Heat-inactivated bacteria (70 °C for 15 min) were used for work in this chapter. Labeling was performed by mixing 2 µl DiOC6(3) (5mg/ml) in the inactivated culture at 37 °C incubator for 30 minutes. Excess labeling dye was removed by pelleting and suspension in fresh PBS. The labeled culture was then suspended in PBS prior to capture studies.

3.2.4 Bacteria capture experiment

A 100 µl solution of 10⁵, 10⁶ and 10⁷ cells/ml was deposited in the PDMS wells, which were attached on the antibody-functionalized ND surface. A cover slip was placed on the top of the PDMS well to prevent evaporation. The surface exposed to the bacterial solution was placed in the 37 °C incubator for 30 minutes. Then the surfaces were washed with PBS (thrice) to remove non-specific bound bacteria. For use with the electrical biosensor, isotonic trehalose solution was used instead of PBS to reduce the conductivity of the media. The surface captured bacteria were imaged using an Olympus BX41 fluorescence microscope equipped with a Photometrics Coolsnap K4 camera and enumerated using ImageJ. Five images for each of the nine NCD samples was collected.

3.2.5 Biosensor fabrication and testing

Biosensor substrates consisted of 525 μm thick silicon with a 280 nm thick thermal oxide layer. The gold/chrome (200nm/25nm) was patterned through lift-off processing. A 300 nm thin PECVD oxide layer was deposited on the gold pattern as an insulation layer. Circular windows were opened in the insulation layer by buffered oxide etching to expose the interdigitated electrodes. Electrical connections were made using a high-density card-edge connector. Impedance measurements were made with a CompactStat (Ivium Technologies). The excitation voltage was limited to 10 mV to prevent the restructuring or delamination of the gold electrodes, the denaturing of attached biomolecules, or electroporation of capture bacteria. Control measurements were made using an isotonic trehalose solution (ITS) that measured a conductivity of 3 $\mu\text{S}/\text{cm}$. First impedance measurements were made after exposing the sensor to 10^6 cells/ml ITS for 1 hour, followed by rinsing with ITS thrice. Subsequently the sensor was exposed to 10^8 cells/ml ITS for 1 hour, followed by rinsing with ITS thrice, and impedance measurement again.

3.3 Results and Discussion

Monocrystalline NDs of an average particle size of 5-nm and a positive zeta potential were obtained as 0.5 (w/v)% in dimethyl sulfoxide (DMSO). The highly polar S=O bond in DMSO is proposed to form strong hydrogen bonds with acidic hydrogen atoms of the hydroxyl groups or the protonated forms of pyrone-like structures that are hypothesized to exist on the surface of NDs with positive zeta potential; thus a more stabilized ND suspension is formed in DMSO.[289] Seeding of ND is typically carried out in alcohols, ketones, DMSO, water, or their mixtures to reduce surface tension,

viscosity, volatility, boiling point, or environmental hazards specifically in case of water. Shenderova and co-workers have reported dilution of DMSO with methanol to produce the best seeding.[289] As shown in Figure 3-1, photon correlation spectroscopy shows that the 1:1 dilution of ND-DMSO with acetone, ethanol, IPA, methanol or water leads to the formation of ND aggregates when sonicated for 30 minutes and rest for 1 hour before particle size measurements in each case. Similar results were also achieved with 1:3 and 1:5 dilutions as shown in Figure 3-2.

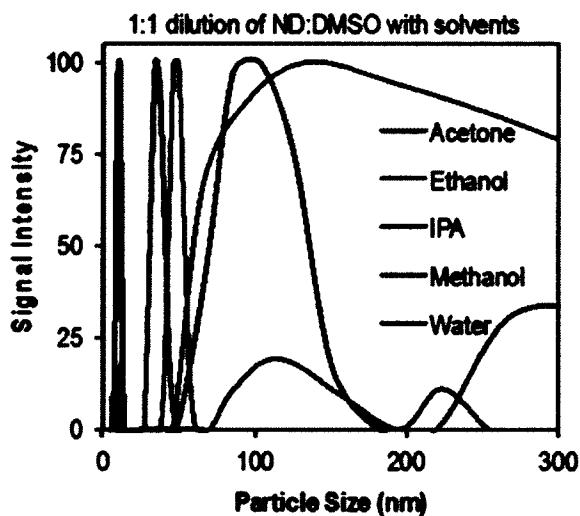


Figure 3-1. Measurement of ND particle sizes after dilution of the original ND containing DMSO with acetone, ethanol, isopropyl alcohol (IPA), methanol, and water. Average values are reported from five repeats.

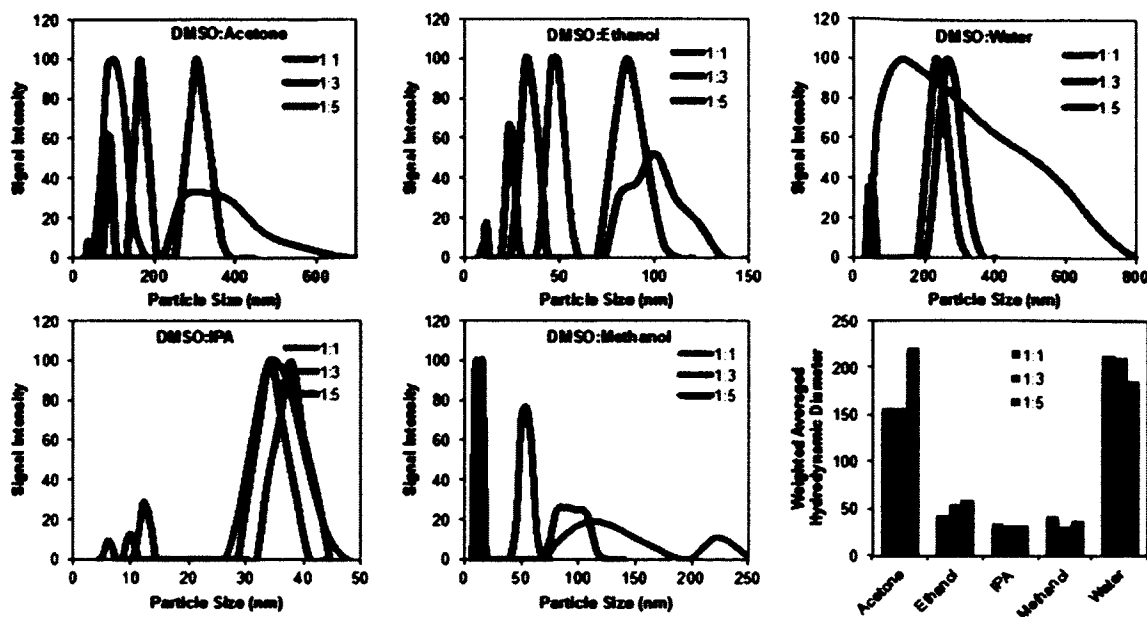


Figure 3-2. Results from photon correlation spectroscopy showing size distribution of ND aggregates obtained by diluting the original ND:DMSO solution with acetone, ethanol, water, IPA, and methanol.

It is that in case of polar protic solvent addition to DMSO, the aggregation of NDs occurs through displacement of polar aprotic DMSO molecules in the solvation sphere that is around the ND, by polar protic molecules of ethanol, IPA, methanol or water, and then this catalyzes the ND aggregation through hydrogen bonding.[289] The extent of ND aggregate size is also dependent on factors such as viscosity, density, and surface tension. Electrophoretic mobility in each case (Figure 3-3) was measured, and calculated zeta (ζ) potentials of the ND aggregates (Figure 3-4). The electrophoretic mobility is highest in case of methanol followed by ethanol, the p values of methanol and ethanol is lower than 0.05. Zeta potential calculations show that the suspensions of ND aggregates are stable ($\zeta > 20$ mV) in case of dilution with alcohols compared to dilutions with acetone or water. This shows that although NDs clump together on the addition of

alcohols, the suspension will provide a stronger resistance to sedimentation in alcohols compared to water and acetone.

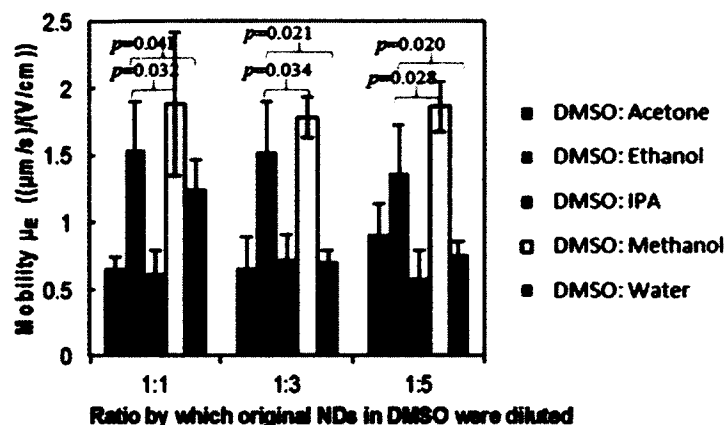


Figure 3-3. Measurement of ND particle mobility (μ_e) after dilution of the original ND containing DMSO with acetone, ethanol, isopropyl alcohol (IPA), methanol, and water. Average values are reported from five repeats.

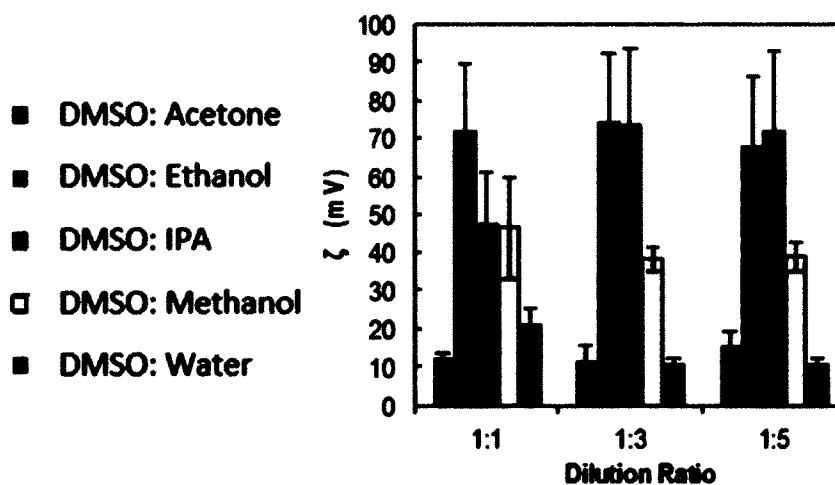


Figure 3-4. Measurement of ND particle zeta potential (Z) after dilution of the original ND containing DMSO with acetone, ethanol, isopropyl alcohol (IPA), methanol, and water. Average values are reported from five repeats.

Further the NDs were seeded on 200 nm thin evaporated gold films on silicon substrates *via* sonication in ND-DMSO diluted with acetone, ethanol, IPA, methanol and water. See Methods section for specific procedure on seeding and analysis of coverage on seeded substrates. Figure 3-5 (left image) shows a representative SEM image obtained for surfaces seeded for 30 minutes with an ND-DMSO diluted (1:1) with methanol. NDs show up as bright white spots in the SEM image. The large white grains in the background are the evaporated gold clusters. It can be seen that NDs were seeded continuously and uniformly irrespective of the topography of underlying gold film; no clustering of NDs was found at the grain boundaries of gold in case of methanol. In order to further extract information on seeding coverage and average seed size, a two-dimensional fast Fourier transform-based filtering was performed to remove the gold background. Figure 3-5 (right image) shows the SEM image obtained upon filtering. Figure 3-1E shows the surface coverage obtained with 30 minutes seeding with a 1:1 dilution of ND-DMSO with acetone, ethanol, IPA, methanol, and water. Methanol provides the highest surface coverage ($33.6 \pm 3.4\%$) compared to the other solvents. Methanol dilutions lower the surface tension, solution viscosity, and solution density, and provide the correct surface forces, while maintaining the small size of the NDs and the high surface area to volume ratio; thus methanol dilutions create the correct proportion of dispersion, polar, and hydrogen bonding forces to lodge particles onto the surface with the highest surface coverage.

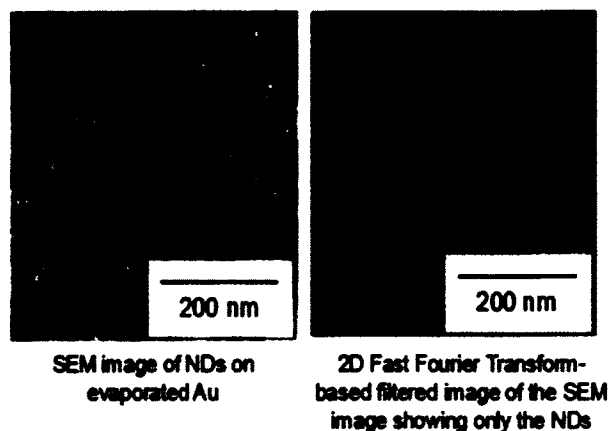


Figure 3-5. On the left is the SEM image showing NDs (bright white spots) seeded on gold surfaces by sonication in solution containing NDs at 0.25% (w/v) for 30 minutes. On the right is the SEM image after 2D FFT filtering highlights the seeded NDs as red regions.

Thus, it is shown that with our low power sonication setup, methanol produces better surface coverage among the many solvents used for ND seeding. Hence, methanol dilutions of ND-DMSO was used for further work in this chapter. In an attempt to reduce the seeding times, Figure 3-6 shows a plot of ND surface coverage on surfaces seeded with solutions of three different ND concentrations (0.25%, 0.125%, 0.083% w/v) for three different seeding times (5, 15, and 30 minutes). As expected, the surface coverage increased with ND concentration and seeding time. The surface coverage to plateau at some point of time and this time point would be earlier for high concentration solutions, all the p values are smaller than 0.05. While using the 0.25% (w/v) solution, the seeding coverage starts to plateau to about 33% coverage at 30 minutes seeding. While such plateau points were not obtained for 0.125% and 0.083% (w/v) solutions within 30 minutes of seeding. Seeding times can be further reduced through the use of ND concentrations higher than 0.25% (w/v).

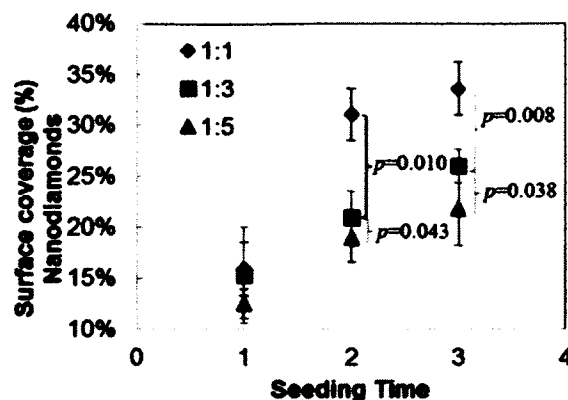


Figure 3-6. Surface coverage of NDs obtained on surfaces seeded for varying amounts of times with methanol solutions containing 0.25%, 0.125%, and 0.08% (w/v) NDs.

Figure 3-7 and Figure 3-8 confirms that ND seeded surfaces can be functionalized using previously reported UV-alkene surface chemistry of CVD diamond films. Surface modification was tested by attachment of FITC-conjugated anti-*E. coli* (*O*+*K*) and measuring the fluorescence intensity as shown in Figure 3-7A. Antibodies were spotted in a 10x10 array using a Nano eNabler™ (~12 μm spot size). Since the functionalization scheme relies on the presence of hydrogenated carbon atoms, the effect of sodium borohydride assisted mild reduction for improvements expected through an increase in antibody attachment was tested. See Figure 3-7B. Quantification of the fluorescence from spotted arrays as shown in Figure 3-8 shows the reduction step does not provide the anticipated enhancement in fluorescence with p value of 0.245. This shows that the as-seeded NDs were adequately hydrogenated for the UV-alkene chemistry. In our experiments, control surfaces (without NDs) record any fluorescence with our microscopes proving insignificant attachment of antibodies.

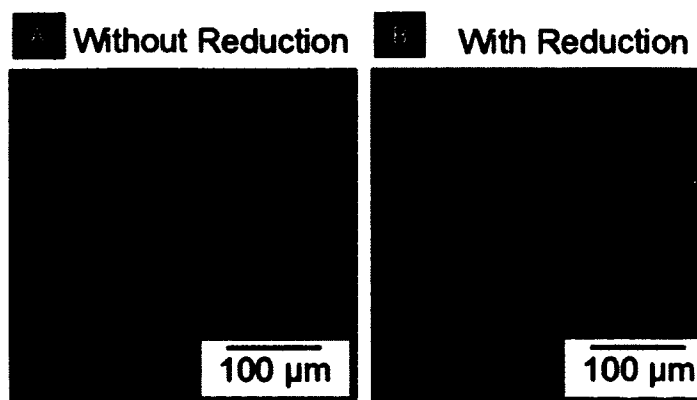


Figure 3-7. Fluorescence images obtained from a 10x10 array of 12 μm spots of FITC-labeled anti-*E. coli* O+K attached to ND-seeded surfaces without (A) and with (B) sodium borohydride reduction treatment prior to performing UV-assisted TFAAD linkage to NDs.

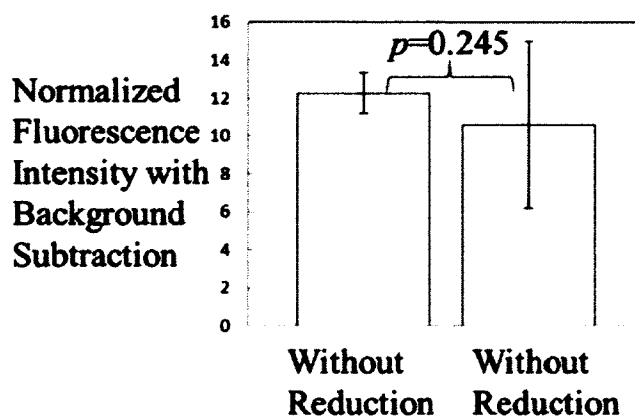


Figure 3-8. Normalized fluorescence intensity obtained from seven 10x10 arrays on ND surface with and without reduction.

Figure 3-9 shows the effect of surface coverage of NDs on the bacteria capture capability from solutions of different bacterial concentrations (10^5 , 10^6 and 10^7 cells/ml). Heat-inactivated *E. coli* O157:H7 were used along with a specific antibody for these experiments. The bacteria capture density was found to increase with surface coverage of NDs. The bacteria capture density would plateau for higher surface coverage values; however, it must not have reached high enough ND surface coverage to achieve the

plateau point. Nevertheless, the capture densities obtained were about 800 cells per sq. mm, which is higher than that reported previously with diamond surfaces for the exact same antibody-antigen pair.[105]

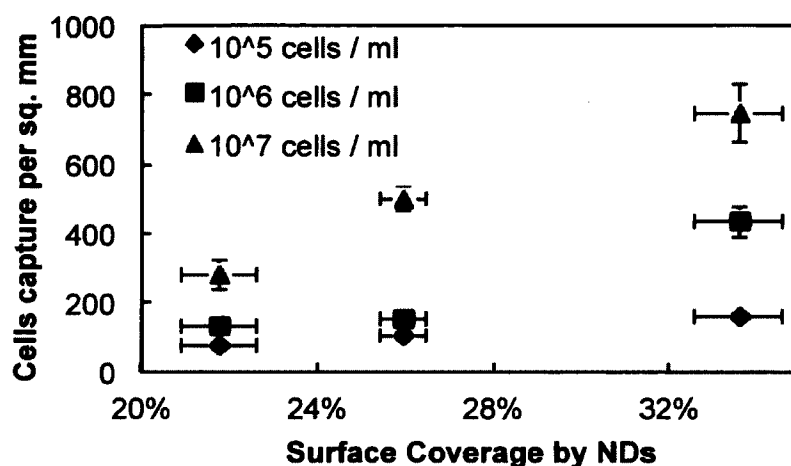


Figure 3-9. Bacteria capture density obtained using the antibody-ND coating as a function of surface coverage of NDs on the sample.

Figure 3-10 shows the microfabricated 3x3 IDE array seeded with NDs using the above recipe that gave us the highest surface coverage. The electrodes were fabricated of 200 nm Au/25 nm Cr, and each finger is 9 μm thick with 9 μm spacing. PECVD oxide was coated to insulate the wiring from the solution and a circular window in the oxide was opened to expose the IDEs to the solution. In order to elucidate the effect on IDE nanostructuring *via* ND seeding, impedance measurements in solutions were performed with varying conductivity before and after ND seeding. Impedance spectra of IDEs in deionized water (as shown in Figure 3-11) shows that the resistive or the charge transfer contribution to the overall impedance decreased with ND seeding. This implies that the ND seeds form electrically conductive islands between the electrode fingers. This is

consistent with previous reports that hydrogen-terminated diamond surfaces become conductive when exposed to water.[297] Figure 3-12 shows that the decrease in overall impedance and shift in phase at the IDEs upon ND seeding were consistently seen in deionized water and phosphate buffered saline (PBS) dilutions. Moreover, as the solution became more conductive the charge transfer took place less through surface conduction and more through solution conductance. Specifically, at 1000 Hz the reduction in magnitude of impedance due to ND seeding changes from 40% to 20% as the solution conductivity increases from 3.95 $\mu\text{S}/\text{cm}$ to 16500 $\mu\text{S}/\text{cm}$. Typically in impedance spectroscopy, the conductivity of the solution is adjusted through addition of potassium chloride to achieve an overall magnitude in the range of 10 to 30 $\text{k}\Omega$ prior to carrying out detection. ND seeding can be used to lower the required impedance without altering the solution conductivity; thus increasing the potential to combine impedance spectroscopy with on-chip pre-concentration mechanisms like dielectrophoresis that require low conductivity solutions.

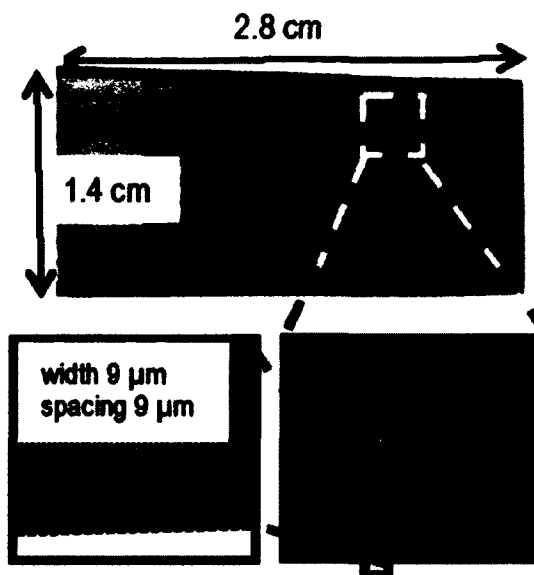


Figure 3-10. Optical images of a biosensor chip containing an array of nine interdigitated electrode (IDE) pairs that were fabricated to demonstrate the application of ND seeding layer for chemically stable covalent linkage of antibodies to electrodes. Each IDE contained sixty finger pairs with each finger 9 μm wide and spaced 9 μm apart.

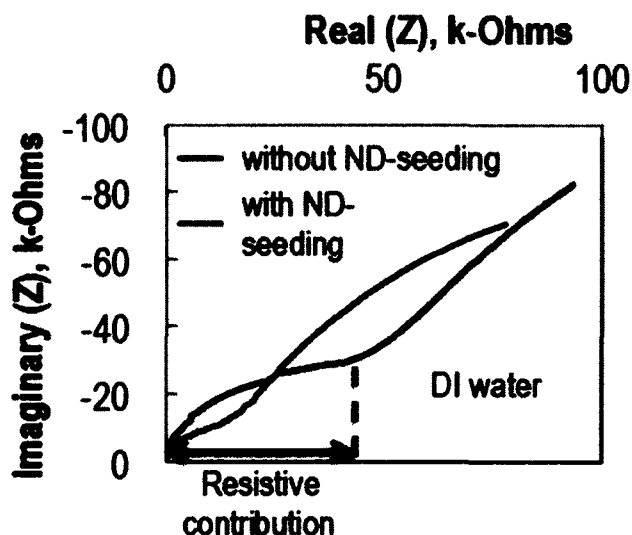


Figure 3-11. A representative plot of real *versus* imaginary part of the impedance measured in de-ionized water on an IDE before and after ND seeding.

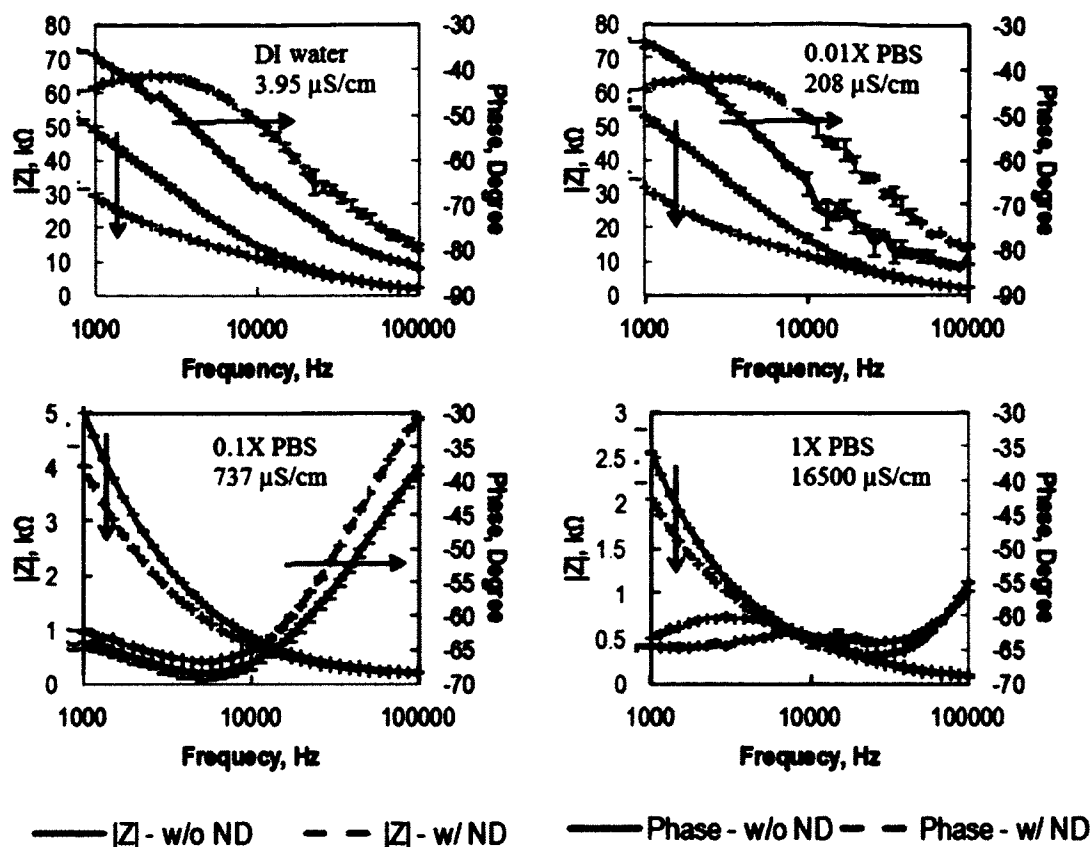


Figure 3-12. Representative plot of impedance magnitude and phase plotted against frequency as obtained on an IDE exposed to solutions with different electrical conductivity.

Further IDEs were seeded with NDs to create non-faradaic impedance biosensors for bacterial detection without using redox probes, where the capture agent was immobilized on the NDs with the UV-alkene surface chemistry. The IDE portion of the chip was seeded with NDs, followed by selective functionalization of some of the IDEs with anti-*E. coli* O157:H7 as described in the Methods section. Further, two control IDEs were created by skipping the antibody attachment step. A polydimethylsiloxane well was then applied on the IDE region, and bacteria were captured from the solution containing 10^6 or 10^8 cells/ml. Changes in overall impedance and phase across each of the IDEs

were recorded over a frequency range from 100 Hz to 10^5 Hz. Figure 3-13 shows sample magnitude and phase curves obtained on one of the active sensors. Although insignificant shifts in impedance magnitude was observed, significant phase shifts on all of the active sensors were observed; such phase shifts were not seen on control sensors. In order to understand the physical basis of the impedance changes, the response of the interface was compared with a variety of different equivalent circuit models, including those discussed by Varshney and Li.[298] While a number of models were investigated by complex non-linear least square fitting using Zview, the circuit shown in Figure 3-14 provided a good fit to the data with a reasonable number of components with errors less than five percent. The equivalent circuit model consists of a double layer capacitance C_{dl} , a generalized finite Warburg element for a short circuit terminus W_s ($Z = R \tanh([\sqrt{i} T \omega]^P) / [\sqrt{i} T \omega]^P$) with a continuously varying exponent ($0 < P < 1$), a charge transfer resistance R_{ct} , a solution resistance R_s , and a resistance R_n and capacitance C_n arising due to the presence of the functionalization layer, including the antibody and the blocker protein molecules. During the dissociation of pure water through $2H_2O \rightarrow H_3O^+ + OH^-$, a total ion concentration (c) of 2×10^{-7} mol/L can be achieved, and hence the maximum Debye length achieved is ($\lambda = 0.3/\sqrt{c} =$) 680 nm at 20 °C. However, in deionized water, due to the presence of impurities, Debye lengths of a few hundred nanometers was expected. Because the Debye screening length is comparable to the height at which antibody binds to the cell surface, the resistance and capacitance of the functionalization layer have been considered discretely as shown in Figure 3-14.

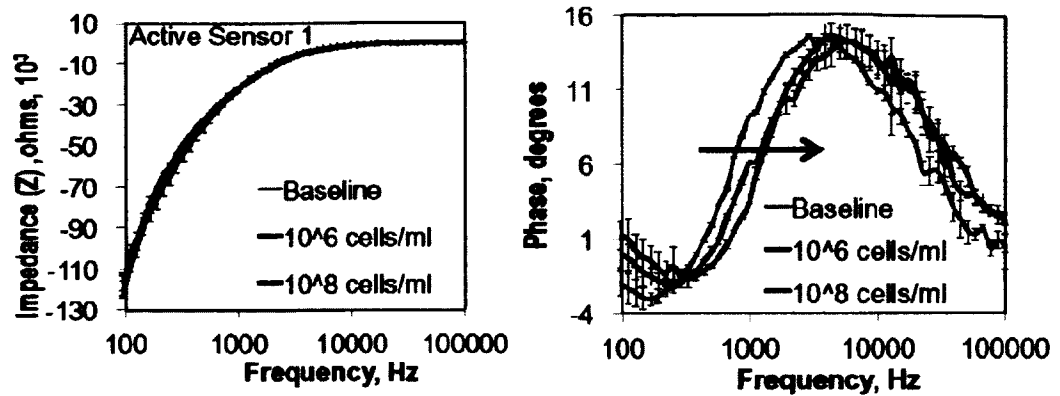


Figure 3-13. Example impedance spectra on an active sensors before (baseline) and after exposure to 10^6 cells/ml or 10^8 cells/ml of *E. coli* O157:H7 cells.

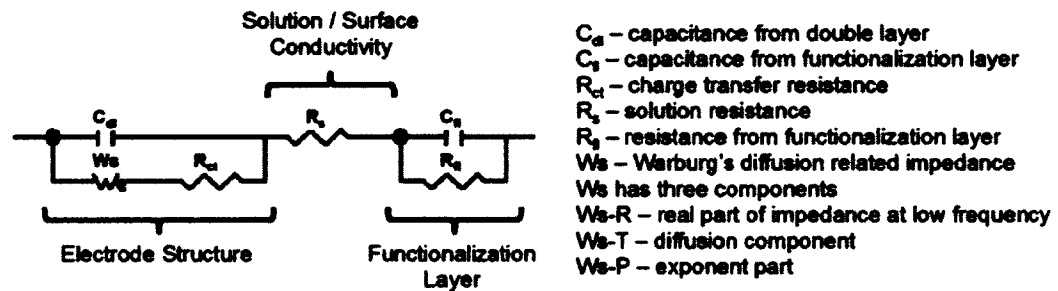


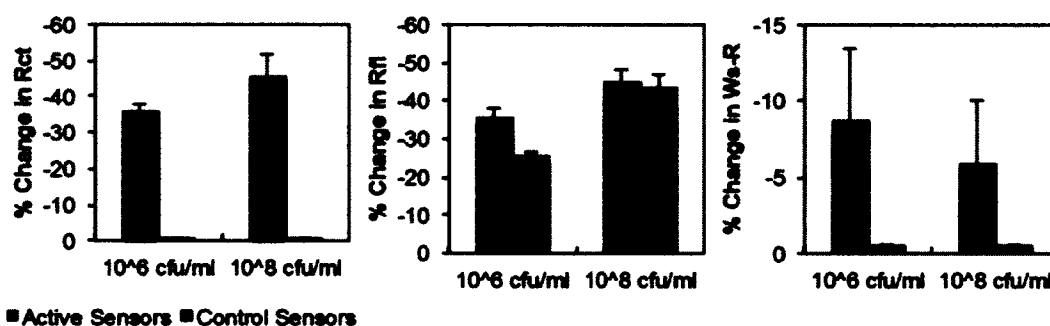
Figure 3-14. A modified Randles circuit that best fit our impedance results.

Equivalent circuit fits obtained for one of the active and the control sensors are given in Table 3-1. Fit results for other active and control sensors are provided in Tables 3-S1 and 3-S2 in the supplementary information respectively. The parameter R_{ct} , R_{fl} , and W_s -R change by more than 5% during the cell capture process with respect to the values obtained after antibody functionalization and blocking as shown in Figure 3-15. The values for R_{ct} decreases by $38.8 \pm 2.3\%$ and $45.9 \pm 5.8\%$ only on the active sensors during the capture from 10^6 cfu/ml and 10^8 cfu/ml respectively, with a minimal change of 6.5% between the two concentrations. This reduction in R_{ct} is because the bacterial attachment causes non-flagellar protein filaments (pili and fimbriae) and

lipopolysaccharides, all primarily negatively charged in case of *E. coli* O157:H7, to replace the less electrically conductive water molecules and lower the charge transfer resistance. This process also reduces the effective diffusion length between adjacent electrodes and thus a decrease in the Warburg diffusion element W_s -R was observed. The values for the exponent P were found to be higher than 0.5, which suggests existence of charge transfer mechanisms other than pure diffusion between the two ND-seeded electrodes. The value of R_n also reduces during the cell capture steps; however, this drop was also seen on the control sensors. The reduction in R_n is due to the loss of casein blocker molecules during the repetitive washing steps post cell capture to remove non-specifically bound bacteria.

Table 3-1. Equivalent Circuit Fit Values For One Of The Active and Control Sensors.

	Active Sensor			Control Sensor		
Parameters	After antibody immobilization and blocking with casein	After capture from 10^6 cfu/ml	After capture from 10^8 cfu/ml	After antibody immobilization and blocking with casein	After capture from 10^6 cfu/ml	After capture from 10^8 cfu/ml
R1 (Ω)	12,541	7,864	6,864	~ 0	~ 0	~ 0
R2 (Ω)	1,807	1176	932.3	1,713	1,259	913
Ws1-R (Ω)	536,160	497,200	512,230	999,220	980,110	982,310
Ws1-T	4.9×10^{-3}			7.2×10^{-3}		
Ws1-P	0.77			0.56		
R2 (Ω)	25			25		
C1 (F)	2.4×10^{-9}			2.2×10^{-9}		
C2 (F)	1.38×10^{-9}			1.4×10^{-9}		

**Figure 3-15.** Significant changes observed in charge transfer resistance (R_{ct}), (R_n), and (W_{s1-R}) upon binding of bacterial cells to the sensor surface.

The change in R_{ct} obtained using the ND-seeded gold electrodes for 10^6 cfu/ml *E. coli* O157:H7 (~38.8%) is nearly 1.5 times higher than the 27.8% change reported by Yang *et al.* using indium tin oxide (ITO) impedance biosensor in combination with

[Fe(CN)₆]^{3-/4-} redox probes.[299] In case of ND-seeded electrodes, the sensor was exposed to 200 µl in a PDMS well, while Yang *et al.* evaporated the 20 µl pure culture on the sensor. The changes in R_{ct} obtained using ND-seeded biosensor for 10⁸ cfu/ml *E. coli* O157:H7 (~46%) is nearly 225% of those reported by Varshney and Li using gold impedance biosensors (-20.9%).[300] Varshney and Li only saw such magnitude of improvement when magnetic nanoparticle based sample enrichment was performed prior to impedance detection. Moreover, one of the active sensors in our test was later tested after storage in ITS at room temperature for four days test, and the fit results were found comparable to the fresh sensors. An extensive testing on stability of antibodies on ND-seeded gold surfaces is being tested. Similarly, while our tests here were limited primarily to 10⁶ and 10⁸ cfu/ml, and detection limits were not evaluated, the combination of the ND-seeded biosensors with the use of redox probes, microfluidics, and preconcentration techniques such as dielectrophoresis or magnetophoresis for real-time pathogen sensing is being tested out.

Table 3-2 shows the properties of solvent mixtures estimated from molar ration weighted calculation. Table 3-3 is equivalent circuit fit values for the other two active sensors, and Table 3-4 is equivalent circuit fit values for the other control sensor.

Table 3-2. Properties of solvent mixtures estimated from molar ratio weighted calculations.

Solvent	Dilution Ratio	Molar Ratio	Dielectric Constant	Refractive Index	Density g/ml	Viscosity mPa-s
Acetone	1:1	0.4919	34.0572	1.4200	0.9390	0.5802
	1:3	0.7439	27.5817	1.3897	0.8625	0.4225
	1:5	0.8288	25.3997	1.3795	0.8370	0.3870
Ethanol	1:1	0.5506	34.5036	1.4140	0.9405	1.4465
	1:3	0.7861	29.2870	1.3862	0.8648	1.2705
	1:5	0.8597	27.6580	1.3776	0.8395	1.2239
IPA	1:1	0.4831	32.8357	1.4297	0.9385	2.2453
	1:3	0.7371	25.5455	1.4038	0.8618	2.3049
	1:5	0.8237	23.0594	1.3950	0.8362	2.3259
Methanol	1:1	0.6385	37.9524	1.3826	0.9415	0.8028
	1:3	0.8412	35.1749	1.3520	0.8663	0.6699
	1:5	0.8983	34.3934	1.3434	0.8412	0.6401
Water	1:1	0.7985	73.2897	1.3624	1.0450	1.1253
	1:3	0.9224	77.4161	1.3443	1.0215	1.0481
	1:5	0.9520	78.4000	1.3400	1.0137	1.0313

Table 3-3. Equivalent Circuit Fit Values for the Other Two Active Sensors.

Parameters	Active Sensor 2			Active Sensor 3		
	After antibody immobilization and blocking with casein	After capture from 10^6 cfu/ml	After capture from 10^8 cfu/ml	After antibody immobilization and blocking with casein	After capture from 10^6 cfu/ml	After capture from 10^8 cfu/ml
R1 (Ω)	13,591	9,148	8,269	21,655	13,498	10,105
R3 (Ω)	1,774	1,170	1,039	1,720	1,055	925
Ws1-R (Ω)	489,690	469,680	480,090	721,470	612,930	648,700
Ws1-T	5.02×10^{-3}			5.07×10^{-3}		
Ws1-P	0.7679			0.73527		
R2 (Ω)	25			25		
C1 (F)	2.75×10^{-9}			2.10×10^{-9}		
C2 (F)	1.46×10^{-9}			1.55×10^{-9}		

Table 3-4. Equivalent Circuit Fit Values for the other Control Sensor.

Parameters	Control Sensor 2		
	After antibody immobilization and blocking with casein	After capture from 10^6 cfu/ml	After capture from 10^8 cfu/ml
R3 (Ω)	1,773	1,348	1,077
Ws1-R (Ω)	1.13×10^6	9.5×10^5	9.3×10^5
Ws1-T	8.6×10^{-3}		
Ws1-P	0.54		
R2 (Ω)	25		
C1 (F)	2.1×10^{-9}		
C2 (F)	1.3×10^{-9}		
R1 (Ω)	1×10^{-7}		

3.4 Conclusion

In summary, a new method using nanodiamond seeding to immobilize antibodies on impedance biosensors has been demonstrated and improve the overall detection sensitivity than that obtained with gold or ITO electrodes. Methanol forms the ideal solvent in seeding gold sensing surfaces with NDs with positive zeta potential, in comparison to solvents such as acetone, ethanol, IPA and deionized water. Further, the seeding has to be performed in solutions with higher ND concentration and for seeding times as long as 30 minutes to produce maximum surface coverage, and to consecutively achieve maximum bacterial capture density. These NDs with positive zeta potential can be functionalized with the UV-alkene chemistry without further reduction step. NDs when seeded at IDEs, act as electrically conductive islands between the electrodes and

reduce the effective gap between the electrodes, thus allowing to perform impedance spectroscopy in solutions with low electrical conductivity such as ITS. This ND seeding procedure along with the UV-alkene chemistry is applicable to a wide range of sensing methodologies, including quartz crystal microbalance, surface plasmon resonance, microarray technology, and electrochemical sensing. Bacterial sensing can be performed in ITS and the changes obtained in resistance to charge transfer with bacterial capture is nearly twice than that obtained with plain electrodes.

CHAPTER 4

REDUCTION OF NON-SPECIFIC BINDING IN BEADS-BASED DIELECTROPHORETIC PRECONCENTRATION AT DIAMOND ELECTRODES

4.1 Introduction

Detection of pathogens is becoming increasingly important in public health applications such as food safety and epidemiology of infectious disease. With the increasing push to lower pathogen detection limits, sample volume, and processing times, preconcentration schemes, or referred to as purification schemes for pathogens from complex sample matrices have become important to integrate with existing biosensors. Many microfluidics-based approaches have been proposed and offer the possibility of automated sample handling with high degree of parallelization. There are several novel preconcentration schemes combined with a microfluidic platform, which is potentially automated, miniaturization, and massparallelization, have been reported, such as dielectrophoresis (DEP) [301-303], magnetophoresis [304-306], acoustophoresis[307, 308], and hydrophoresis[309]. Dielectrophoretic (DEP) can work across a wide range of particle size from DNA to large cells or bacteria. The particles become polarized in the presence of a non-uniform electric field which will generate DEP force. Particles in the field will be attracted to the high or low field gradient depending on the particle electrical properties relative to those of the suspension medium, and the frequency of excitation. Combining DEP with the use of microfluidic channel become practical because sufficient

field strength is achievable at sub-millimeter scale with only few volts applied. Selective concentration can be achieved in a single automated device. Isolator-based DEP concentrator has successfully separated polystyrene beads[310-312], DNA[313, 314], yeast cells[315], virus[316], and bacteria cells[310, 317-319]. The microelectrode of the DEP device is offering a variety of configurations, such as parallel or interdigitated [320], castellated [321], insulator-based or electrodeless [322], extruded [323-325], and top-bottom patterned [326-329]. The configuration of interdigitated or parallel, castellated, insulator-based DEP device are formed as a 2-D configuration, which means the electrode are on the same platform. Top-bottom DEP device forms with the DEP electrodes in a 3-D configuration, the top and bottom of the microfluidic channel of the DEP device need to be patterned with DEP electrodes. Most of the DEP devices have been reported use insulator-based configuration, which means the DEP electrodes are covered with an insulator layer, except extruded configuration [323-325]. Plus, the magnitude of DEP force decreases exponentially with distance above the electrodes,[330] the DEP-based pre-concentrator typically only sample a small portion of the liquid stream unless the devices use shallow channel ($\leq 100 \mu\text{l}$), low flow rate ($\leq 1 \mu\text{l}/\text{min}$), or both in the reasonable voltage[331]. The reasonable voltage range is limited because of the Joule heating and electrolysis of the electrodes. In this chapter, a boron-doped ultra-nanocrystalline diamond (BD-UNCD)-based DEP pre-concentrator was introduced, which can be operated with a much higher voltage range because of the largest electrochemical potential window of diamond in an aqueous electrolyte [90, 265, 332]. The DEP device setup which contains microfluidic channel made with an indium tin oxide (ITO) coated glass, pre-patterned double side tape and a BD-UNCD chip. The ITO-

coated glass and BD-UNCD chip were connected with two alligator clips, which could apply AC. The DEP working efficiency and deduction of non-specific bonding by introducing polyethylene glycol (PEG) during the DEP application period have been demonstrated in this chapter.

In the pathogen detection application of DEP concentration, cell damage from DEP should be considered. Yang *et al.* proved 4 hour or greater DEP (5 MHz, 20 V_{p-p}) applied on *Listria monocytogenes* cells caused significant delay on cell growth in the low conductive growth media[333]. No evidence shows influences in immuno-assay based biosensing with DEP damaged cells. However, the antibody-coated beads for detecting bacteria and toxin using a microflow cytometer has been attractive in recent years[334-337]. In this chapter, an antibody/polyethylene glycol (PEG) functionalized beads-based pathogen isolating method was introduced to pre-select the target cells, *E. coli O157:H7* was chosen as model bacteria in this chapter. The 4 µm carboxylate-/sulfate-, epoxy-/sulfate-, and aldehyde-/sulfate- surface modified beads were chosen for the study. The amount of protein loading was characterized by MicroBCA and 280 nm UV protein assays. The immobilization of PEG was investigated using zeta-potential measurement. The 4 µm antibody/PEG functionalized beads was added to bacteria culture and mixed for 30 min, the mixture of beads and bacteria was separated using centrifugation because the different size and diameter of beads and bacteria. The isolating efficiency and selectivity has been studied in this chapter. Plus, the deduction of non-specific bonding of functionalized beads with PEG immobilization has been demonstrated, and the chemical reaction scheme of immobilizing antibody/PEG is shown in Figures 4-1, 4-2, and 4-3.

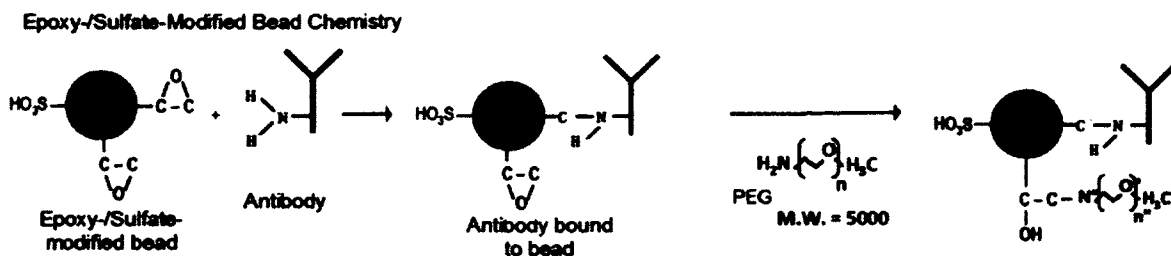


Figure 4-1. Co-immobilization of IgG and PEG on epoxy-/sulfate-modified beads.

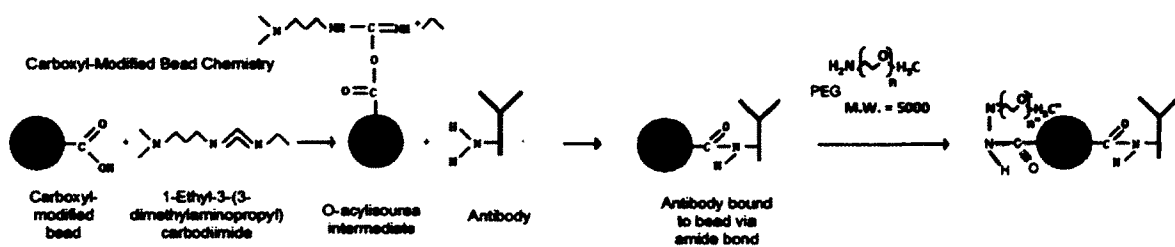


Figure 4-2. Co-immobilization of IgG and PEG on carboxylate/sulfate-modified beads.

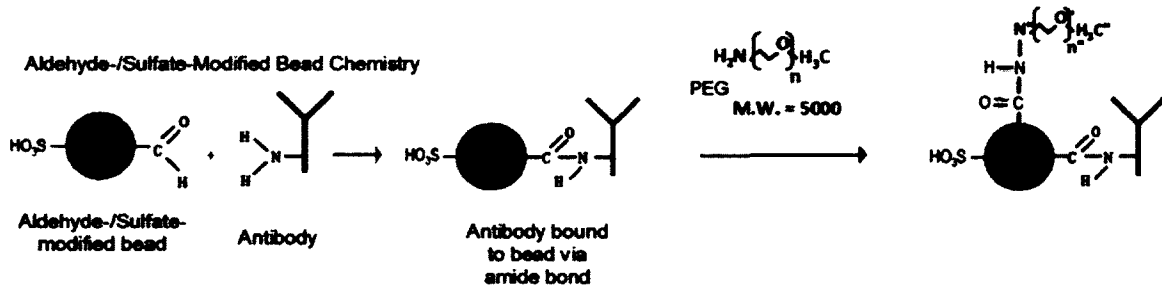


Figure 4-3. Co-immobilization of IgG and PEG on aldehyde-/sulfate-modified beads.

4.2 Materials and Methods

4.2.1 Materials

The boron-doped ultracrystalline diamond (BD-UNCD) wafer with 2 μm diamond film with resistivity of $0.2\ \Omega\cdot\text{cm}$ on a 1 μm thick silicon dioxide and 500 μm thick silicon wafer was acquired from Advanced Diamond Technology. Indium tin oxide coated polished float glass with a sheet resistivity of 15-25 Ω/square was bought from Delta Technology Ltd. The double-sided tape of 25 μm thickness was obtained from Nitto Denko America, Inc. All stock solutions were prepared by deionized (DI) water with a minimum resistivity of $18.0\ \text{M}\Omega\cdot\text{cm}$. Phosphate-buffered solution (PBS), PBS with 0.1% Tween 20 (PBS-T20), casein blocking buffer and bovine serum albumin (BSA) were bought from Sigma-aldrich. The 2-(N-morpholino)ethanesulfonic acid (MES) buffer (50 mM pH 6.0), 1-ethyl-3-(3-dimethylaminopropyl)-carbodiimide hydrochloride (EDC), micro-BCA kit and bovine gamma globulin (BGG) standards were procured from Thermo Scientific. Diethylamine (DEA) was obtained from Sigma. Cy3TM-labeled mouse IgG, goat anti-mouse IgG and FITC-labeled goat anti-mouse IgG were obtained from Jackson ImmunoResearch. The 4 μm epoxy-/sulfate-, carboxylate-/sulfate-, and aldehyde-/sulfate- modified PS beads and epoxy-modified magnetic beads were procured from Invitrogen. Pentaerythritol triacrylate (PETA) was obtained from Alfa Aesar. Trimethylolpropane tris-(3-mercaptopropionate) (TMPTMP) was obtained from Evans Chemetics LP. The m-polyethylene glycol amine (PEG, M.W. 5000) was bought from Laysan Bio, Inc.

4.2.2 Coimmobilization of IgG and PEG on epoxy-/sulfate- modified PS beads or epoxy-modified magnetic beads

A 50 μ l, 4 (w/v)% bead solution (as received) was mixed with 950 μ l of MES buffer (50 mM, pH 6.5) and 17.5 μ l of 2 mg/ml FITC-labeled goat anti-mouse IgG fixing the total amount of IgG at 35 μ g/mL which is five times more than the saturation value calculated as follows. The total amount of IgG required to achieve surface saturation S mg/g of beads can be calculated as shown in Eq. 4-1,

$$S = \frac{6C}{\rho_s d} = \frac{6 \times 2.5 \text{ mg/m}^2}{1.055 \text{ g/cm}^3 \times 4 \mu\text{m}} = 3.55 \frac{\text{mg}}{1 \text{ g } 4 \mu\text{m beads}} \quad \text{Eq. 4-1}$$

where, ρ_s is the density of solid sphere (1.055 g/cm³ for polystyrene), C is the monolayer protein capacity of the beads surface (2.5 mg IgG/m² of sphere surface) and d is the diameter of the sphere. The mass of beads in the 50 μ l, 4 (w/v)% bead solution calculates to be (0.05 mL x 1 g/mL x 4 (w/v)% =) 0.002 g. Therefore the amount of antibody needed to achieve surface saturation of the added beads will be (3.55 mg/ 1 g of 4 μ m beads x 0.002 g =) 7.1 μ g.

The beads were incubated with antibody for 4 h at 20 °C. The solution was then centrifuged at 5000g for 20 min, the supernatant was removed and the pelleted beads were washed thrice with 50 mM PBS through subsequent vortexing and centrifuging. The beads were then resuspended in 50 mM PBS with 1 mg/mL of PEG and incubated for 2 h at 20 °C. The beads were then washed thrice with 50 mM PBS and resuspended in BSA blocking buffer. After incubation for 1 h at 20 °C, the beads were washed thrice and resuspended in 50 mM PBS buffer with 130 μ g/mL sodium azide. The beads were stored at 4 °C until ready to use. The beads were discarded after 1 month of storage at 4 °C.

4.2.3 Coimmobilization of IgG and PEG on carboxylate-modified PS beads

A 50 μ l, 4 (w/v)% bead solution (as received) was mixed with 950 μ l of MES buffer (50 mM, pH 6.0) containing 40 mg EDC, and incubated for 30 min at 20 °C to create the acylisourea intermediate. The solution was then centrifuged at 5000g for 20 min, the supernatant was removed and the pelleted beads were resuspended in MES buffer (50 mM, pH 6.5) with 17.5 μ l of 2 mg/ml FITC-labeled goat anti-mouse IgG. This solution was incubated for 4 h at 20 °C. The solution was then centrifuged at 5000g for 20 min, the supernatant was removed and the pelleted beads were washed thrice with 50 mM PBS through subsequent vortexing and centrifuging. The beads were then resuspended in 50 mM PBS with 1 mg/mL of PEG and incubated for 2 h at 20 °C. The beads were then washed thrice with 50 mM PBS and resuspended in BSA blocking buffer. After incubation for 1 h at 20 °C, the beads were washed thrice and resuspended in 50 mM PBS buffer with 130 μ g/mL sodium azide. The beads were stored at 4 °C until ready to use. The beads were discarded after 1 month of storage at 4 °C.

4.2.4 Coimmobilization of IgG and PEG on aldehyde-/sulfate-modified PS beads

A 50 μ l, 4 (w/v)% bead solution (as received) was mixed with 950 μ l of MES buffer (50 mM, pH 6.5) and 17.5 μ l of 2 mg/ml FITC-labeled goat anti-mouse IgG. This solution was incubated for 4 h at 20 °C. The solution was then centrifuged at 5000 g for 20 min, the supernatant was removed and the pelleted beads were washed thrice with 50 mM PBS through subsequent vortexing and centrifuging. The beads were then resuspended in 50 mM PBS with 1 mg/mL of PEG and incubated for 2 h at 20 °C. The beads were then washed thrice with 50 mM PBS and resuspended in BSA blocking buffer. After incubation for 1 h at 20 °C, the beads were washed thrice and resuspended

in 50 mM PBS buffer with 130 $\mu\text{g/mL}$ sodium azide. The beads were stored at 4 °C until ready to use. The beads were discarded after 1 month of storage at 4 °C.

4.2.5 Coimmobilization of mouse IgG and PEG on BD-UNCD

As shown in Figure 4-4, as obtained BD-UNCD wafer was diced into 12 mm x 16 mm chips. Subsequently each BD-UNCD chip (12×16 mm) was first rinsed with acetone, IPA, DI water, and dried with nitrogen. Trifluoroacetamide-protected 10-aminodec-1-ene (TFAAD) was custom synthesized was mixed with 1-dodecene in 2:1 ratio (v/v) as the functionalization mix. The 1-dodecene provides space for TFAAD molecules and enhances the efficiency of deprotection. The photochemical attachment was carried out in a nitrogen purged reaction chamber. The functionalization mix was applied uniformly between the BD-UNCD surface and a piranha-cleaned quartz slide at about 2 $\mu\text{L}/\text{cm}^2$, then radiated with 254 nm UV at $\sim 2 \text{ mW}/\text{cm}^2$ for 8 h. Excess reaction mix was removed by sonicating the chip in chloroform and isopropyl alcohol for 5 minutes. The TFAAD attached BD-UNCD film was deprotected in a tightly sealed vial containing 65 mM sodium borohydride in anhydrous methanol solution. The solution was incubated for 6 h at 70 °C to create a primary amine group termination. The sample was then rinsed with DI water and dried with nitrogen. The primary amines on the sample surface were further reacted with glutaraldehyde in sodium cyanoborohydride coupling buffer at 20 °C for 4 h to yield an aldehyde group termination. The aldehyde-terminated surface was rinsed with DI water and dried with nitrogen. The functionalized surface was incubated for 18-22 h at 4 °C with a 100 $\mu\text{g/mL}$ mouse IgG solution. The next day, the surface was washed with PBS-T20 twice and PBS once to remove non-specifically adsorbed antibodies. The surface was further reacted with PEG-NH₂ for 1 h at 20 °C. The basic washing routine

was performed to remove non-specific absorbed PEG. The non-specific binding sites were blocked with a casein-based blocking buffer for 1 h at 20 °C. The surface was then washed again with PBS-T20 twice and PBS once to remove loosely bound casein.

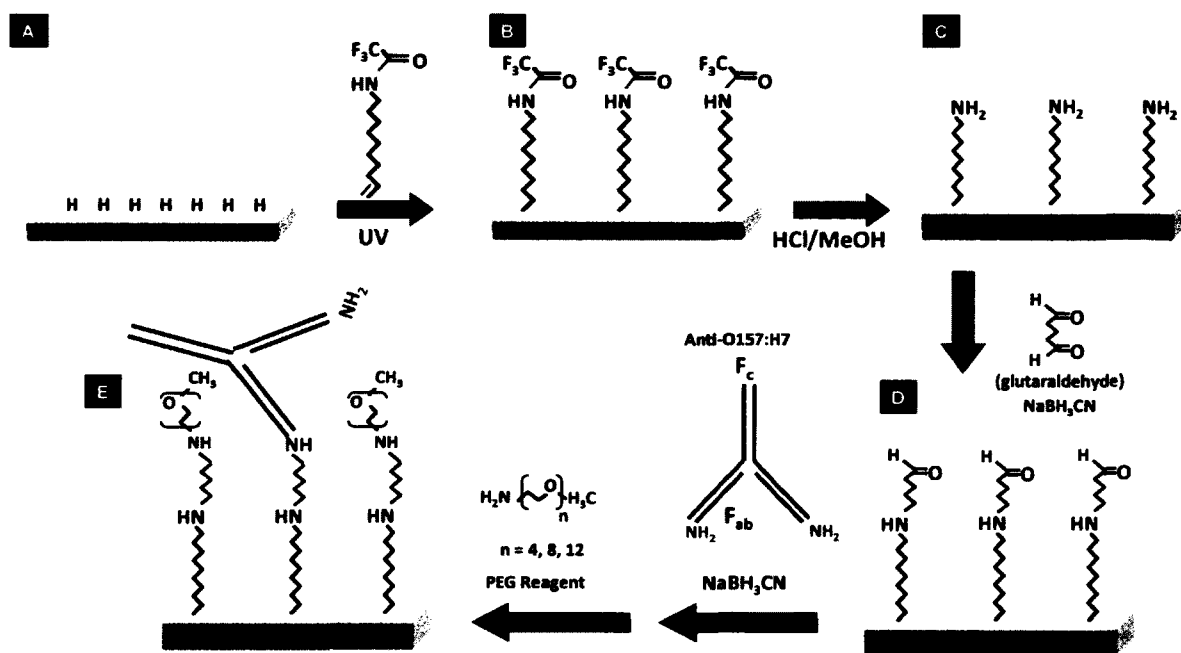


Figure 4-4. Co-immobilization of IgG and PEG on BD-UNCD surface using the UV-alkene chemistry. (A) As-deposited BD-UNCD is hydrogen-terminated. (B) TFAAD grafted to BD-UNCD surface. (C) Trifluoroacetic acid group is deprotected to create primary amines. (D) Reductive glutaraldehyde of the primary amines on the BD-UNCD surface. (E) Reaction with primary amines on the IgG with the aldehydes on the BD-UNCD surface followed by reaction of remainder of the aldehyde groups with the primary amines of the PEG.

4.2.6 Preparation of microfluidic channel with BD-UNCD functionalized surface

Figure 4-5A shows the exploded view of different layers of the microfluidic preconcentrator which contains the glass slides with ~100 nm ITO layer coated underneath, the 25 μm thick double side tape patterned with xurography, the 1 μm thick BD-UNCD layer, the 1 μm thick silicon dioxide layer and the 525 μm thick silicon layer. Using a diamond tipped pen, the surface of the functionalized BD-UNCD chip was

scratched in the middle which is shown in Figure 4-5B. This created two discontinuous areas on the chip, right half of the chip where DEP was applied and left half where DEP was not applied. The pattern of a 2×10 mm microfluidic channel was drawn in Adobe Illustrator software, and a cutting plotter was used to pattern the 25 μ m thick, 12 mm \times 16 mm double sided tape. One side of the tape was attached to the 12 mm \times 18 mm ITO coated glass, and 1/32" holes were drilled on the ITO coated glass slide using a diamond-coated wire (Lasco Diamond Products). The ITO-coated glass chip with the patterned double-sided tape and the BD-UNCD chip were clipped together using a vise for 1 h to seal the channel. The DEP bias was applied between the ITO layer and the right side of the BD-UNCD film. Microfluidic connections to the holes drilled in the ITO-coated glass were made using in-house machined L-shaped connectors. An 8 mm thick thiol-acrylate resin block was formed as previously published by Bounds *et al.* [338]. Briefly, DEA and PETA were mixed in a ratio of 16.1 mol% DEA based on acrylate groups ($\% \text{DEA} = (\text{mol DEA}) / (\text{mol Acrylate groups} + \text{mol DEA})$) for at least three hours at 20 °C. This solution was then mixed with the same volume of TMPTMP. The mixture was centrifuged at 5000 rpm for 3 min to remove bubbles. The mixture was poured over a double-sided sticky tape laying in a petri dish and cured for 1 hr at 20 °C. The cured polymer was cut into 5 \times 5 mm pieces, and drilled with a 1/32" hole on the side and the bottom to create an L-shaped channel.

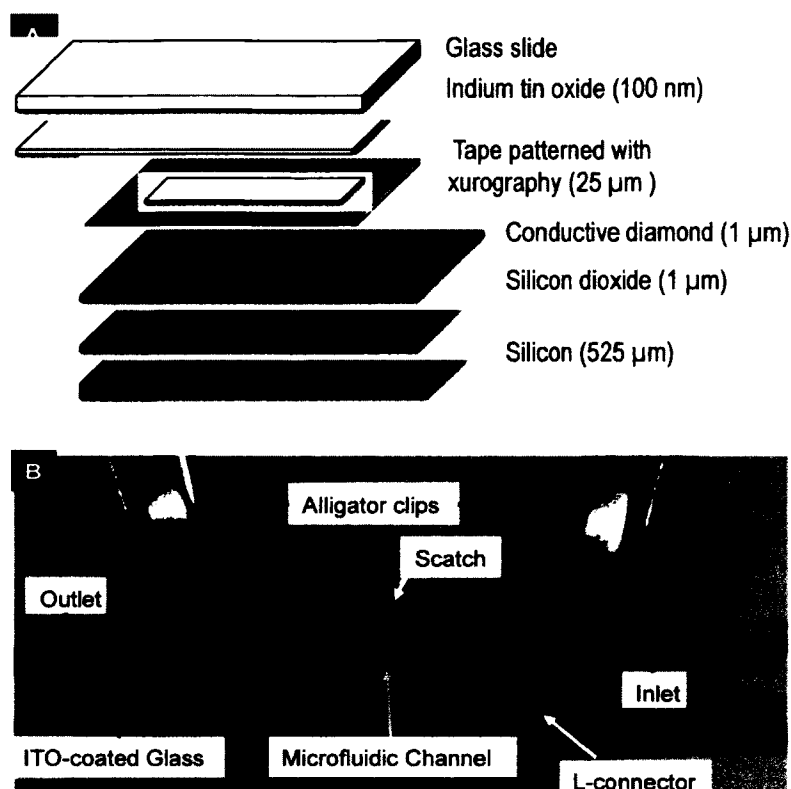


Figure 4-5. (A) Exploded view of the microfluidic preconcentrator showing different layers of construction. (B) A packaged microfluidic preconcentrator under testing.

4.2.7 Specific and non-specific adsorption of functionalized beads on functionalized BD-UNCD surface

The tubings and microfluidic connectors were blocked with casein by pumping the blocking solution at 10 $\mu\text{L}/\text{min}$ for 1 h. The blocked tubes and channels were washed with PBS-T20 for 20 min at 100 $\mu\text{L}/\text{min}$ and PBS for 20 min at 100 $\mu\text{L}/\text{min}$. To perform the tests, 1 mL of 10^5 beads/mL solution was pumped into the channel at 10 $\mu\text{L}/\text{min}$ to perform the specific and non-specific absorption with a 6 V_{p-p} , 40 kHz, square wave applied between the ITO and one side of the BD-UNCD film. The channel was then washed with PBS-T20 for 20 min at 100 $\mu\text{L}/\text{min}$ and PBS for 20 min at 100 $\mu\text{L}/\text{min}$ to

remove the non-specifically bound beads prior to quantification of beads using fluorescence microscopy under an Olympus BX-41 microscope.

4.2.8 Comparing the pathogen capture performance of different beads

Epoxy-/sulfate, aldehyde-/sulfate and carboxylate-modified PS beads, and epoxy-modified magnetic beads were functionalized with anti-*E. coli* O157:H7 with and without co-immobilization with PEG (M.W. 5000) as explained above. Capture of *E. coli* O157:H7 from isolate cultures containing approximately 1000 *E. coli* O157:H7 cfu/ml or co-cultures containing 500 *E. coli* O157:H7 cfu/ml and 500 *E. coli* K12 cfu/ml approximately. The beads were mixed with cultures for 1 h at 20 °C using a shaker. The PS beads were separated from bacteria by centrifuging at 2000 rpm for 9 min and washed twice with PBS. Negative control samples were created by eliminating the bead addition step; this allowed enumerating the bacteria that settled during the selective centrifuging of beads and beads with bacteria. The beads from the bacteria capture experiments were then plated on the LB and MacConkey Sorbitol agar plate for 12 h at 37 °C to determine the capture efficiency and selectivity of the beads is to count the plate. The LB agar plates are non-selective and allow enumeration in capture experiments with isolate cultures. The MacConkey Sorbitol (SMAC) agar allows differentiation between *E. coli* O157:H7 and *E. coli* K12 when captured by the beads from the co-cultures. *E. coli* O157:H7 produces clear colonies on the SMAC agar whereas the *E. coli* K12 produces pink colonies.

4.3 Result and Discussion

Binding of IgG was confirmed with a quantifiable 280 nm UV protein assay as well as micro-BCA assay to measure the amount of IgG before and after

functionalization of each bead type, and the amount of IgG loading on each bead type was determined by subtracting the latter two measurements. As shown in Figure 4-6A and 4-7A, calibration was created relating the optical densities in either protein quantification assay to the concentration of BGG, which BGG is an accepted reference protein for total protein quantitation of purified antibodies. As shown in Figure 4-6B and 4-7B, 280 nm UV absorption tends to overpredict IgG loading compared to the micro-BCA assay. Overall, a reaction time of 2 h is adequate for IgG attachment to either type of bead, and epoxy-/sulfate PS beads and epoxy-modified magnetic beads showed higher IgG loading compared to aldehyde-sulfate and carboxylate-modified PS beads. The IgG loading on the aldehyde-sulfate and carboxylate-modified PS beads indicated formation of a near monolayer coverage ($7.1 \mu\text{g}$ as calculated in the Methods section), while the IgG loading on epoxy-functionalized beads tend to load nearly double the amount of IgG. The p values are shown in Figure 4-6B and 4-7B.

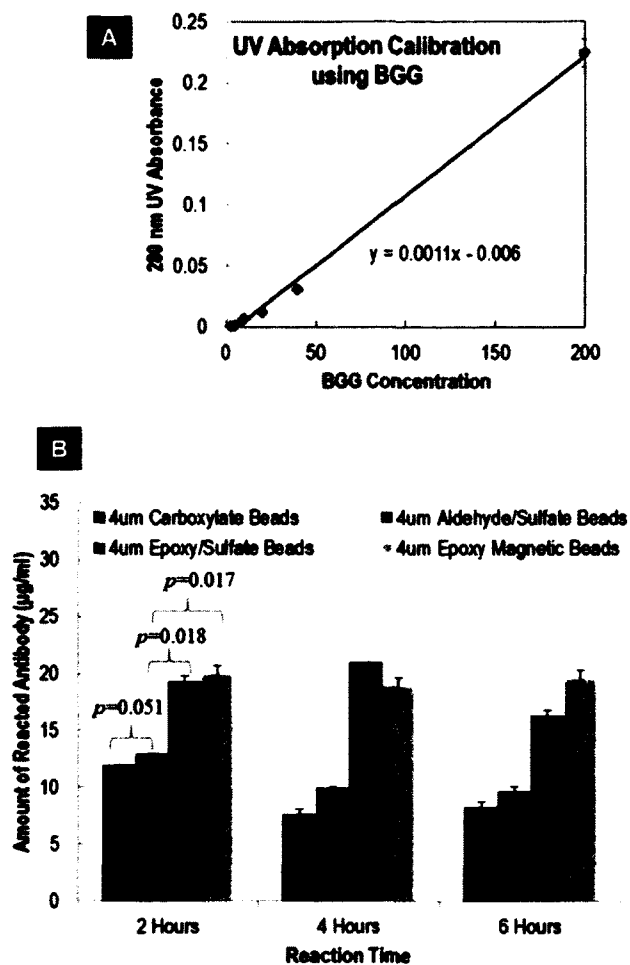


Figure 4-6. (A) Calibration chart correlating the 280 nm UV absorption to the BGG standard concentrations. (B) Amount of antibody reacted with carboxylate-modified (blue columns), aldehyde-/sulfate (red columns) and epoxy-/sulfate (green columns) PS beads, and epoxy-modified magnetic beads (yellow columns) as a function of incubation time as calculated using UV absorption at 280 nm.

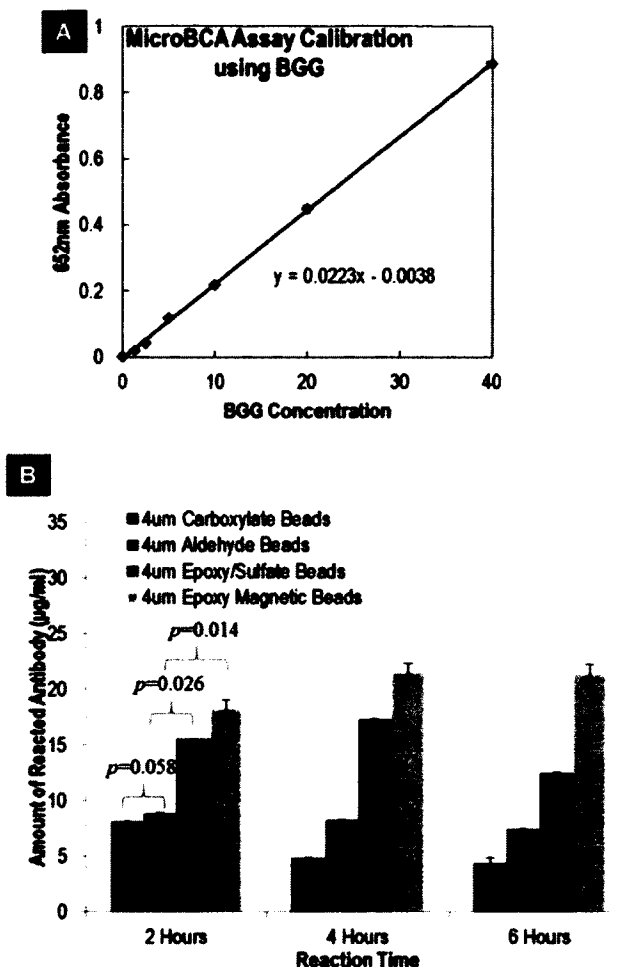


Figure 4-7. (A) Calibration chart correlating the absorption at 652 nm when measured using the micro-BCA assay to the BGG standard concentrations. (B) Amount of antibody reacted with carboxylate-modified (blue columns), aldehyde-/sulfate (red columns) and epoxy-/sulfate (green columns) PS beads, and epoxy-modified magnetic beads (yellow columns) as a function of incubation time as calculated using the micro-BCA assay.

To characterize the attachment of PEG to the PS beads, as shown in Figure 4-8 the electrophoretic mobilities of the beads as received, after attachment of IgG and after attachment of PEG were measured using a Brookhavens Instruments' ZetaPlus™. The values for zeta potential were calculated using the Smoluchowski equation. Since zeta-potential is the potential difference between the dispersion medium and the slipping layer of the particle, a change in zeta potential with the attachment of PEG on the bead surface

can be observed. Further, it is known that when the zeta potential of colloids is between 0 to ± 5 mV leads to instant coagulation, between ± 10 to ± 30 mV leads to incipient stability, between ± 30 to ± 40 mV leads to moderate stability, between ± 40 to ± 60 mV leads to good stability, and greater than ± 60 leads to excellent stability. Since the aldehyde groups present a mild negative charge, the sulfate-groups in the as received beads were responsible for the zeta potential of -51.45 mV as shown in Figure 4-9 (blue columns). The attachment of IgG adds positively charged amine residues to the surface, which counteracts the stabilizing effect of the negatively charged sulfate groups and reduces the net charge per bead; thus increase the zeta-potential to -42.64 mV. Further, the co-immobilization of PEG adds its negatively charged backbone to the bead surface and thus reduces the zeta-potential to -51.45 mV. The as received epoxy-/sulfate beads showed a zeta potential of -38.54 mV, which is higher than that of as received aldehyde-/sulfate beads (-51.45 mV). This may be due the low polarity of the epoxy group in water compared to an aldehyde group. The attachment of IgG makes the zeta potential of the epoxy-/sulfate beads (-45.65 mV) similar to that of IgG coated aldehyde-/sulfate beads (-42.64 mV). The attachment of PEG increases the average zeta potential to -49.56 mV; however, it was a statistically insignificant increase. Since the carboxylate-modified beads lacked ionizable sulfate groups like the other beads, the zeta potential of the as-received beads was high (-20.78 mV). Attachment of IgG dropped the zeta potential to -33.34 mV, a value closer to that of other IgG coated beads. Attachment of PEG to the carboxylate-modified beads dropped the zeta potential further to -47.94 mV, which is close to the values for other IgG/PEG co-immobilized beads. Overall, the zeta potential

values show that PEG co-immobilization was achieved on the all the PS beads and it dropped the zeta potential close to -50 mV, thus improving the stability of the beads.

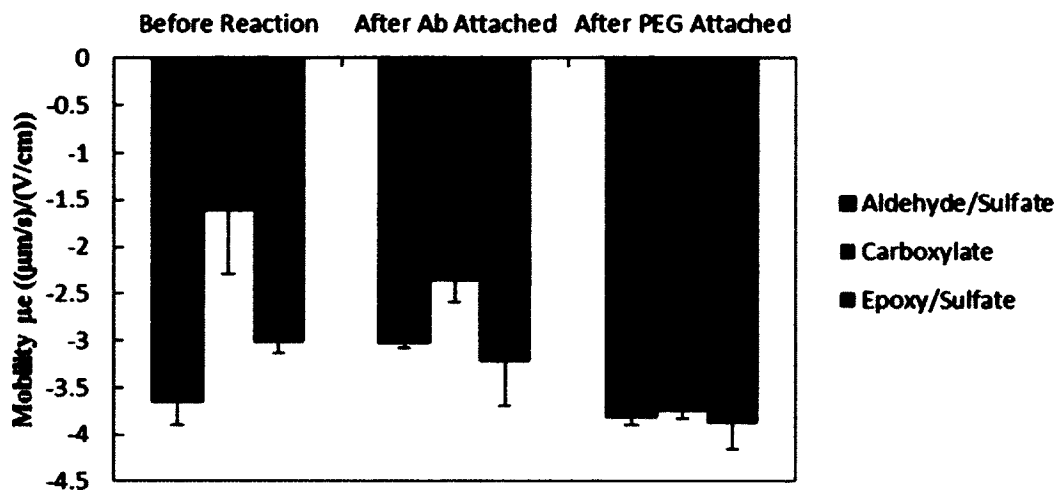


Figure 4-8. The electrophoretic mobility experimentally measured for carboxylate-modified, aldehyde-/sulfate and epoxy-/sulfate beads as received, after antibody attachment, and after PEG co-immobilization.

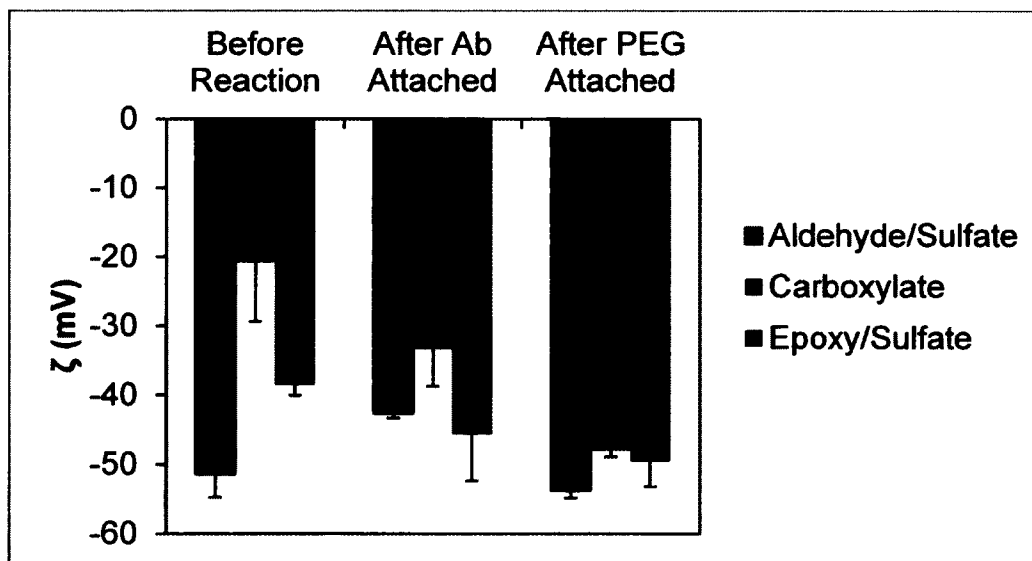


Figure 4-9. The zeta-potential measurement of CML, aldehyde/sulfate and epoxy/sulfate beads after antibody and PEG attached.

Next, how PEG coimmobilization influenced the effectiveness of epoxy-/sulfate, aldehyde-/sulfate, and carboxylate-modified PS beads and epoxy-modified magnetic beads in capturing live pathogen *E. coli* O157:H7 is measured. Figure 4-10 shows capture efficiency % (CE%) for tests conducted from PBS containing ~1000 *E. coli* O157:H7 cfu/ml. CE% was defined as $[(E. coli\ O157:H7\ \text{count captured by beads} - E. coli\ O157:H7\ \text{count in negative controls}) / E. coli\ O157:H7\ \text{count initially present}] \times 100$. The carboxylate-modified beads with IgG and PEG coimmobilization resulted in highest CE% ($\sim 64.8 \pm 3.7\%$). This was found statistically higher than the $45.26 \pm 2.7\%$ CE% demonstrate by the carboxylate-modified beads without PEG co-immobilized ($p=0.011$). However, statistically significant increase or decrease in CE% with coimmobilization of PEG was not found with the aldehyde-/sulfate and epoxy-/sulfate PS beads and epoxy-modified magnetic beads with all p values larger than 0.05. The coimmobilization of PEG on carboxylate-modified beads forces the antibody into a favorable position for increased antibody-antigen interactions. Meanwhile, it is unable to explain why such enhancements are not seen on other types of beads. While the epoxy-modified magnetic beads did not show enhancement with PEG coimmobilization, a significant reduction in the standard deviation in CE% was observed. One would expect that since epoxy-/sulfate-modified PS beads showed a higher IgG loading, it would result in higher CE%. However, the epoxy-/sulfate-modified PS beads showed the lowest CE%, $\sim 32.8 \pm 8.6\%$ with PEG and $\sim 30 \pm 8.82\%$ without PEG. This is possibly because most of the Fab sites are not available for antigen binding. There are some reports show that the random orientation of immobilized antibody causes reduction the effect of antigen binding.[339]

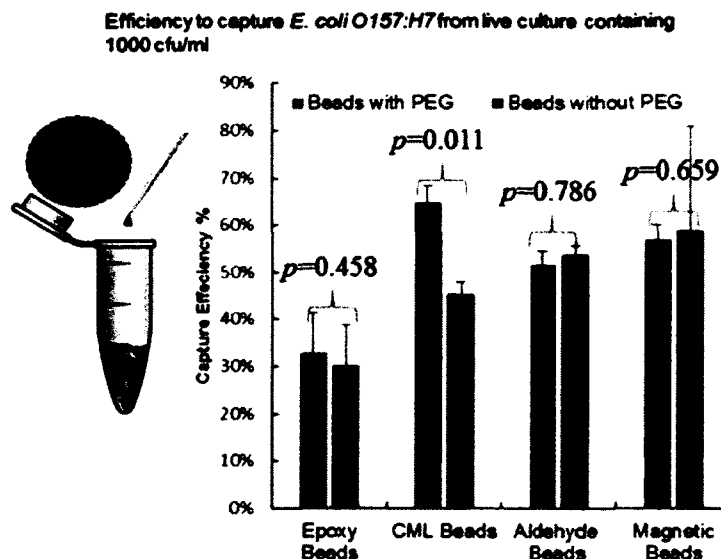


Figure. 4-10 CML, aldehyde/sulfate, epoxy/sulfate and magnetic epoxy *E. coli* O157:H7 antibody and PEG functionalized beads bacteria isolating efficiency study in *E. coli* O157:H7 cell culture.

Figure 4-11 shows the influence of PEG coimmobilization on CE% for tests conducted from PBS containing ~500 *E. coli* O157:H7 cfu/mL and ~500 *E. coli* K12 cfu/mL. Here, carboxylate-modified beads showed higher CE% compared to other beads and the effect of PEG coimmobilization did not change the average CE% obtained by the carboxylate-modified beads (p values smaller than 0.05), $\sim 65.1 \pm 8.8\%$ with PEG and $\sim 64.9 \pm 6.9\%$ without PEG (p value of 0.712). Also, compared to the capture study from isolate cultures, the CE% obtained with carboxylate-modified beads with PEG was not statistically different; however, a higher CE% for carboxylate-modified beads without PEG was observed when the capture was conducted from mixed culture. In general, coimmobilizing PEG on beads did not show statistically significant change in CE% when capturing *E. coli* O157:H7 from mixed culture. The epoxy-/sulfate-modified beads gave the lowest CE% among the beads tested and showed similar CE% with PEG ($37.3 \pm$

6.3%) and without PEG ($36.6 \pm 5\%$). Also, compared to the capture study from isolate cultures, the average CE% obtained with epoxy-/sulfate-modified beads with PEG was higher but statistically insignificant ($p=0.876$). Similarly, for the aldehyde-/sulfate-modified PS beads and epoxy-modified magnetic beads, the CE% obtained from isolate and mixed cultures were statistically indifferent. However, higher standard deviations in the CE% were obtained during the capture tests from mixed cultures.

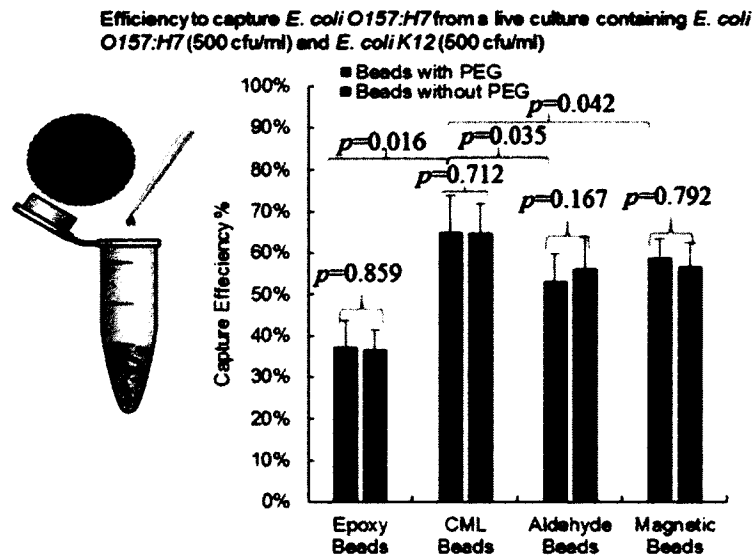


Figure. 4-11 CML, aldehyde/sulfate, epoxy/sulfate and magnetic epoxy *E. coli* O157:H7 antibody and PEG functionalized beads bacteria isolating efficiency in *E. coli* O157:H7 with *E. coli* K12 mixed culture.

Figure 4-12 shows selectivity % (S%) for *E. coli* O157:H7 capture test from mixed cultures. S% was defined as ($[E. coli$ O157:H7 count captured by beads – *E. coli* O157:H7 count in negative controls] / [total bacteria count captured – total bacteria count captured in negative controls] x 100). While high standard error was recorded due to the low bacterial counts in our experiments, by comparing the mean values S% >95 were obtained using with PEG coimmobilization on carboxylate-modified PS beads and

epoxy-modified magnetic beads. Meanwhile, the lowest %S was obtained with epoxy-/sulfate PS beads. The increase in S% with coimmobilization of PEG was also seen with carboxylate-modified PS beads ($p=0.038$) and epoxy-modified magnetic beads ($p=0.040$). There is no such improvement in %S with coimmobilization of PEG on aldehyde-/sulfate ($p=0.800$) or epoxy-/sulfate beads ($p=0.426$). From the test results in Figure 3, carboxylate-modified PS beads give the best CE% and S% when capturing pathogen from an isolate or mixed culture.

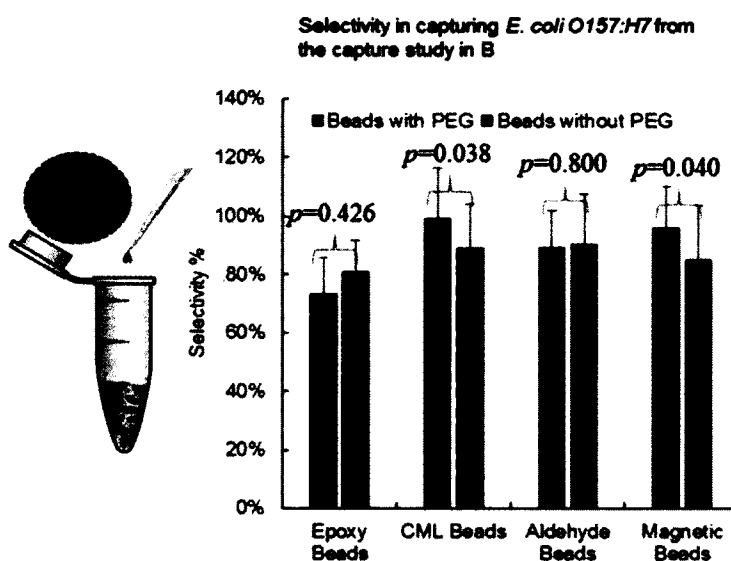


Figure. 4-12 CML, aldehyde/sulfate, epoxy/sulfate and magnetic epoxy *E. coli* O157:H7 antibody and PEG functionalized beads bacteria isolating selectivity study in *E. coli* O157:H7 with *E. coli* K12 mixed culture.

In Figure 4-13, 4-14, and 4-15 shows the accuracy, sensitivity, and specificity of antibody immobilized beads capture *E. coli* O157:H7 in the mixed *E. coli* O157:H7 and *E. coli* K12 culture. From the t-test evaluation, there is no significant change of the

accuracy, sensitivity, and specificity of three kinds of beads with or without PEG immobilization due to all the p values are bigger than 0.05.

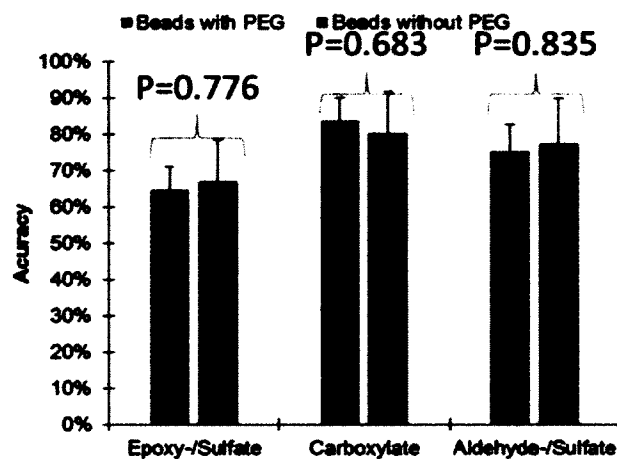


Figure 4-13. The accuracy of antibody immobilized beads capture *E. coli* O157:H7 in the mixed *E. coli* O157:H7 and *E. coli* K12 culture.

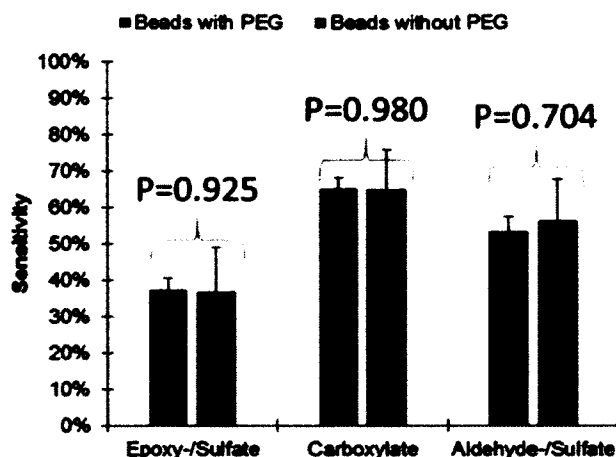


Figure 4-14. The sensitivity of antibody immobilized beads capture *E. coli* O157:H7 in the mixed *E. coli* O157:H7 and *E. coli* K12 culture.

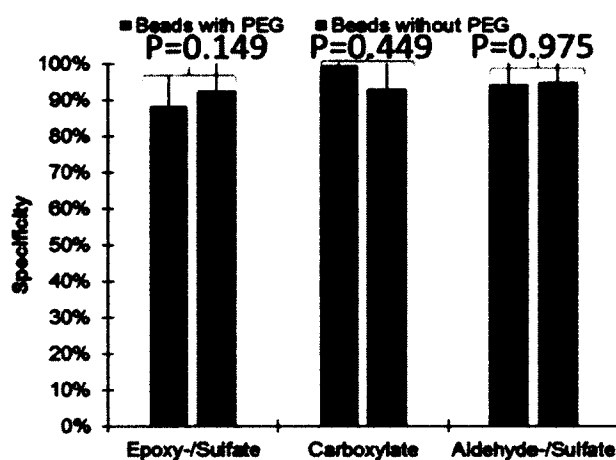


Figure 4-15. The specificity of antibody immobilized beads capture *E. coli* O157:H7 in the mixed *E. coli* O157:H7 and *E. coli* K12 culture.

As shown in Figure 4-16, BD-UNCD chips were functionalized with anti-mouse IgG, with or without PEG, and further treated with a blocking protein (casein). The functionalized BD-UNCD chips were then packaged with a microfluidic channel on top, and epoxy-/sulfate, aldehyde-/sulfate, or carboxylate-modified beads decorated with mouse IgG were passed through the microchannel to learn how coimmobilization of PEG and IgG on the BD-UNCD affected the bead capture. The magnetic beads were not

chosen, as they tend to settle faster in microfluidics channels compared to PS beads due to the density of magnetic beads. A 4 mm² area of the microfluidic channel was imaged to enumerate bead capture. Statistically with or without PEG on BD-UNCD, specific capture of the aldehyde-/sulfate- (green columns), the epoxy-/sulfate- (red columns) and the carboxylate-modified (blue columns) beads showed statistically insignificant difference (p values larger than 0.05), however the mean values did show an increase in specific capture with PEG on BD-UNCD, with the epoxy-/sulfate-modified beads captured the most ($p=0.031$). Next, as illustrated in Figure 4-17, how coimmobilization of PEG and IgG on the BD-UNCD affected the non-specific binding of bead was tested. BD-UNCD chips were functionalized with PEG, and blocked with casein. The coimmobilization of PEG reduces the non-specific binding of carboxylate- beads by ~28% ($p=0.023$), while a statistically insignificant difference was observed in the cases of aldehyde-/sulfate- ($p=0.489$) and epoxy-/sulfate- ($p=0.156$) modified beads.

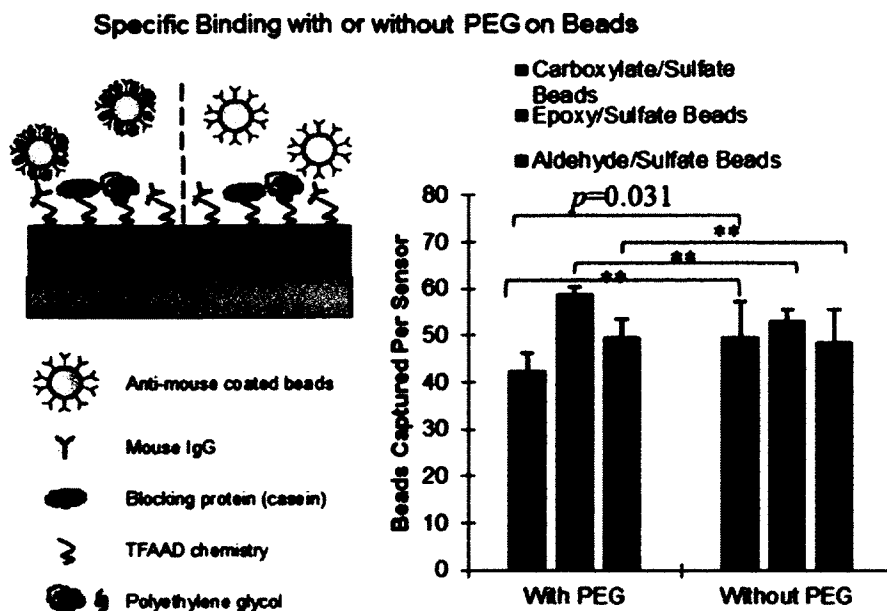


Figure. 4-16 The specific capture test of anti-mouse IgG functionalized microspheres on BD-UNCD surface with or without PEG immobilization without DEP applied. (** represents $p>0.05$)

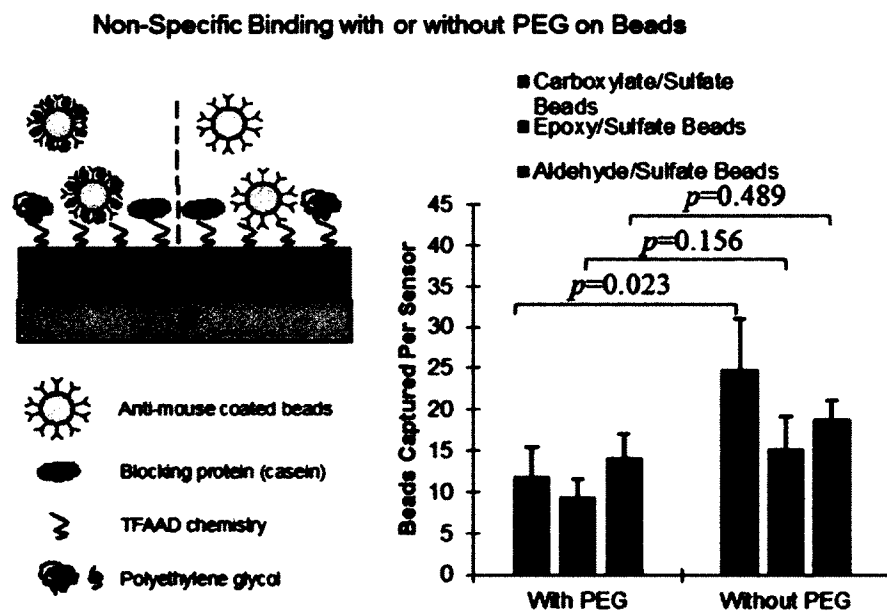


Figure. 4-17 The non-specific capture test of anti-mouse IgG functionalized microspheres on BD-UNCD surface with or without PEG immobilization without DEP applied.

Next, the same capture experiment as above while applying a DEP field between the ITO coated glass top and the BD-UNCD floor of the microfluidic channel were performed. The surface chemistry of BD-UNCD will hold up to DEP for 1 h, specifically if the specific and non-specific binding was altered due to changes in the IgG, PEG, or blocker protein content on BD-UNCD. As shown in Figure 4-18, BD-UNCD chips were functionalized with anti-mouse IgG, with or without PEG, and blocked with casein prior to flowing mouse IgG coated beads in the presence of a DEP field. Like above, a 4 mm² area of the microfluidic channel was imaged to enumerate beads capture. The specific capture of epoxy-/sulfate beads was highest, irrespective of PEG presence on BD-UNCD. Also, the presence of DEP did not change the influence of PEG coimmobilization as noted above in the absence of DEP, statistical indifference in specific capture was found with and without PEG on BD-UNCD (*p* values larger than 0.05). Overall, the use of DEP resulted in higher specific capture of all the beads. The use of epoxy-/sulfate beads showed an increase in specific capture of ~60% with PEG on BD-UNCD and ~63% without PEG. Carboxylate beads showed an increase in specific capture of ~19% with PEG on BD-UNCD and ~43% without PEG. Aldehyde-/sulfate beads showed an increase in specific capture of ~37% with PEG on BD-UNCD and ~50% without PEG.

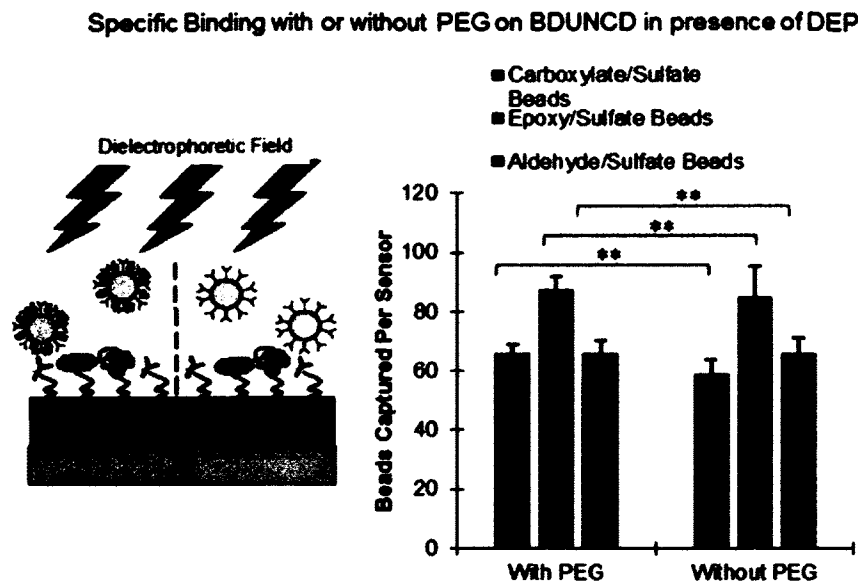


Figure. 4-18 The specific capture test of anti-mouse IgG functionalized microspheres on BD-UNCD surface with or without PEG immobilization with DEP applied. (** represents $p > 0.05$)

Next, as illustrated in Figure 4-19, how coimmobilization of PEG and IgG on the BD-UNCD affected the non-specific binding of beads in the presence of DEP were tested. BD-UNCD chips were functionalized with PEG, and blocked with casein prior to flowing mouse IgG coated beads in the presence of a DEP field. The addition of PEG on BD-UNCD reduced the non-specific binding of the epoxy-/sulfate beads by ~37% ($p=0.026$), which is higher compared to that found in the absence of DEP. The non-specific binding of aldehyde-/sulfate and carboxylate-modified beads showed statistically insignificant change on adding PEG to the BDUNCD surface (p values larger than 0.05). Overall, like the observations on specific binding in Figure 4-17, the non-specific binding of all beads had increased with DEP compared to the non-specific binding without DEP. To examine closely the extent of DEP-mediated increase in specific binding over non-specific binding, specificity % (Sp%) as (bead captured specifically / bead captured

specifically and nonspecifically x 100) was calculated. Table 4-1 shows the Sp% values calculated from data in Figure 4-16, 4-17, 4-18, and 4-19. The Sp% in experiments without PEG coimmobilization on BD-UNCD with DEP and without DEP is found within $\pm 5\%$ error of each other. The same holds true for Sp% in experiments with PEG coimmobilization on BD-UNCD with DEP and without DEP. This shows that DEP did not increase the non-specific binding over non-specific binding, neither *vice versa*. Further, the Sp% in experiments without DEP show that the addition of PEG to the BD-UNCD surface did not improve non-specific binding above and beyond a $\pm 5\%$ error of each other. The same holds true for Sp% from experiments with DEP. Examining the mean values, the epoxy-/sulfate beads show some improve in Sp%, but still within a $\pm 5\%$ error margin. This shows that the coimmobilization of PEG on BDUNCD did not majorly improve the specific binding over non-specific binding.

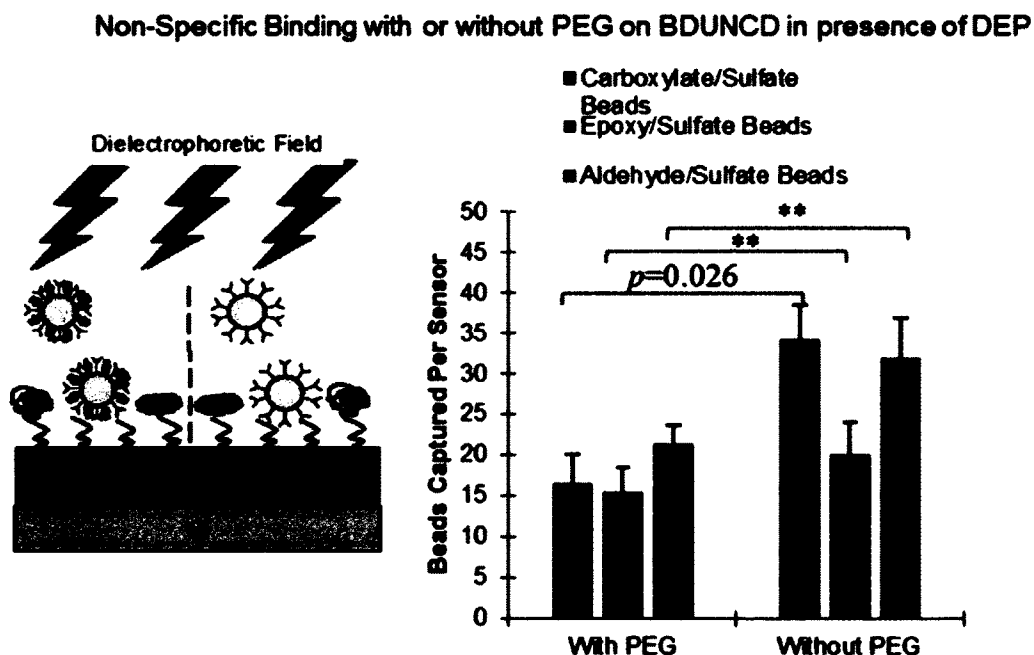


Figure. 4-19 The non-specific capture test of anti-mouse IgG functionalized microspheres on BD-UNCD surface with or without PEG immobilization with DEP applied. (** represents $p>0.05$)

Table 4-1. Specificity of capture calculated from data in Figure 4-16, 4-17, 4-18, and 4-19.

Bead Type	without DEP		with DEP	
	without PEG on BD-UNCD	with PEG on BD-UNCD	without PEG on BD-UNCD	with PEG on BD-UNCD
Epoxy-/Sulfate	72±6.2%	78±5.4%	72±6.7%	81±6.6%
Aldehyde-/Sulfate	69±4.3%	67±4.2%	67±5.1%	69±4.1%
Carboxylate	64±4.0%	69±3.8%	65±4.5%	65±3.3%

As shown in Figure 4-20, the BD-UNCD surface is functionalized with anti-mouse IgG and blocked with blocking protein (casein). The carboxylate- (blue columns), aldehyde- (green columns), and epoxy- (red columns) beads with mouse IgG immobilized were applied on the BD-UNCD surface for 1 hour to test the specific binding ability with the present of PEG on the bead surface. Aldehyde-/sulfate-, epoxy-/sulfate- and carboxylate-/sulfate- functionalized beads show similar behavior on specific capture. There is no significant decreasing of specific capture with or without PEG attachment on the beads (p values larger than 0.05). In Figure 4-21, it illustrated the test of non-specific binding of beads with or without the present of PEG immobilization, which shows a great reduction of non-specific binding of beads on BD-UNCD surface when the beads are decorated with PEG (p values smaller than 0.05). The dielectrophoresis (DEP) is an important factor to improve the specific capture efficiency of IgG functionalized beads on the BD-UNCD surface. The specific capture was improved by applying DEP force to grab down the functionalized beads onto the BD-

UNCD surface to have more chance of physical contact for all three different surface modified beads, however, there is no decreasing of specific capture whether with the immobilization of PEG on the bead surface (p values larger than 0.05), as shown in Figure 4-22. Although, with the DEP applied, the beads will have a greater chance to have physical contact with BD-UNCD surface which will also give a higher chance of non-specific binding. Figure 4-23 illustrates the non-specific bonding of functionalized beads has a slightly increase comparing with no DEP present, but the non-specific binding was greatly decreased by coimmobilizing PEG on beads surface for epoxy-/sulfate- beads ($p=0.012$). Table 4-2 shows the Sp% values calculated from data in Figures 4-20, 4-21, 4-22, and 4-23.

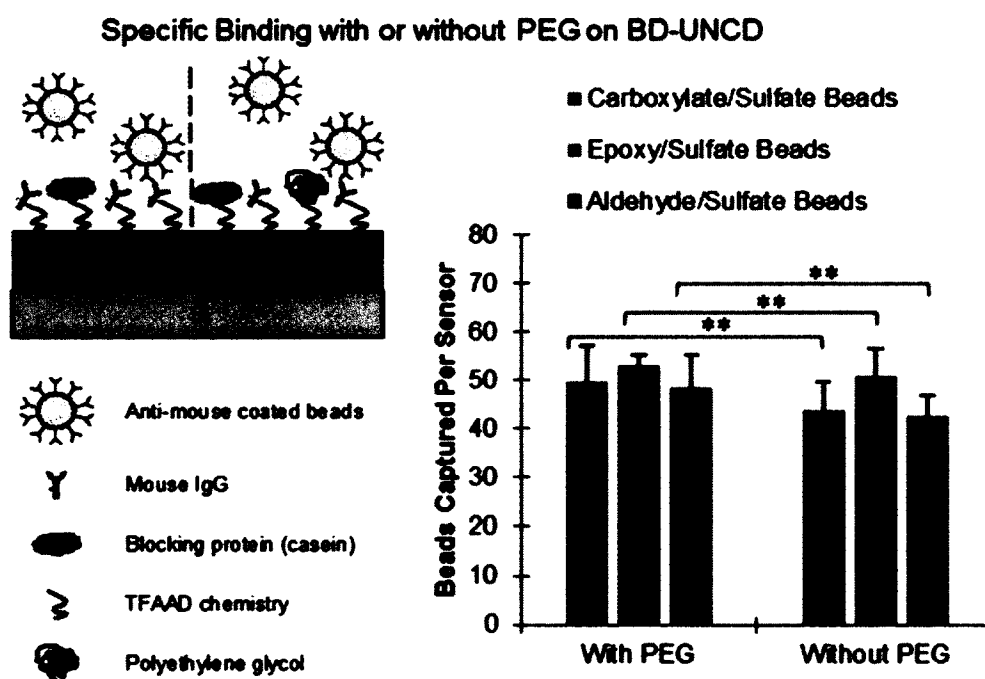


Figure. 4-20 The specific capture test of anti-mouse IgG functionalized microspheres on BD-UNCD surface with or without PEG immobilization without DEP applied. (** represents $p > 0.05$)

Non-Specific Binding with or without PEG on BD-UNCD

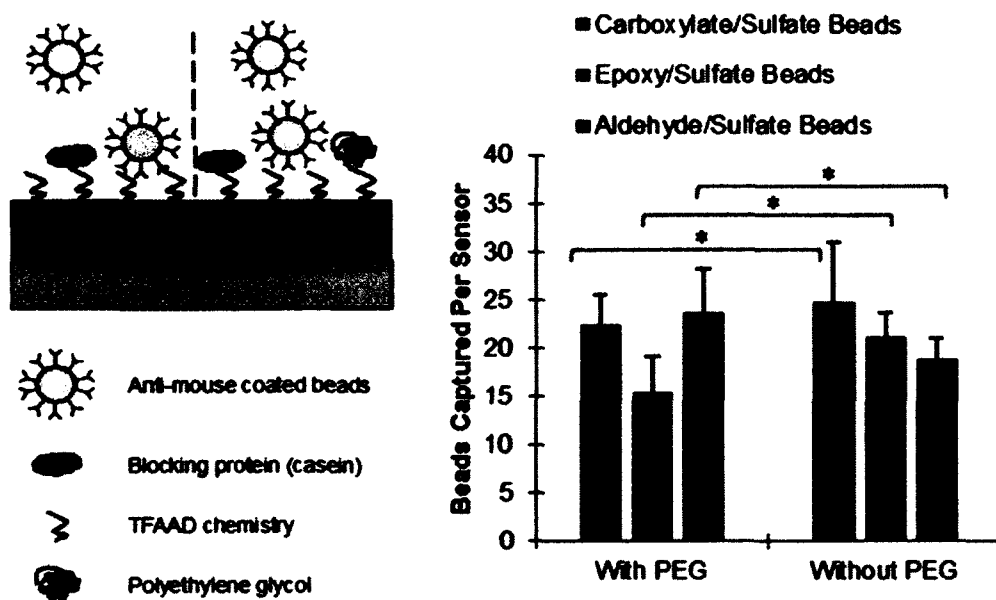


Figure. 4-21 The non-specific capture test of anti-mouse IgG functionalized microspheres on BD-UNCD surface with or without PEG immobilization without DEP applied. (* represents $p < 0.05$)

Specific Binding with or without PEG on BDUNCD in presence of DEP

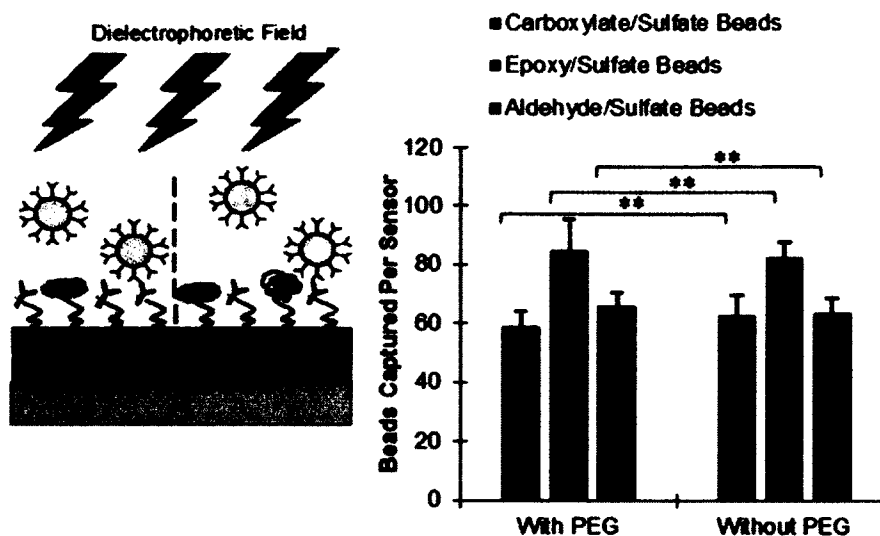


Figure. 4-22 The specific capture test of anti-mouse IgG functionalized microspheres on BD-UNCD surface with or without PEG immobilization with DEP applied. (** represents $p > 0.05$)

Non-Specific Binding with or without PEG on BDUNCD in presence of DEP

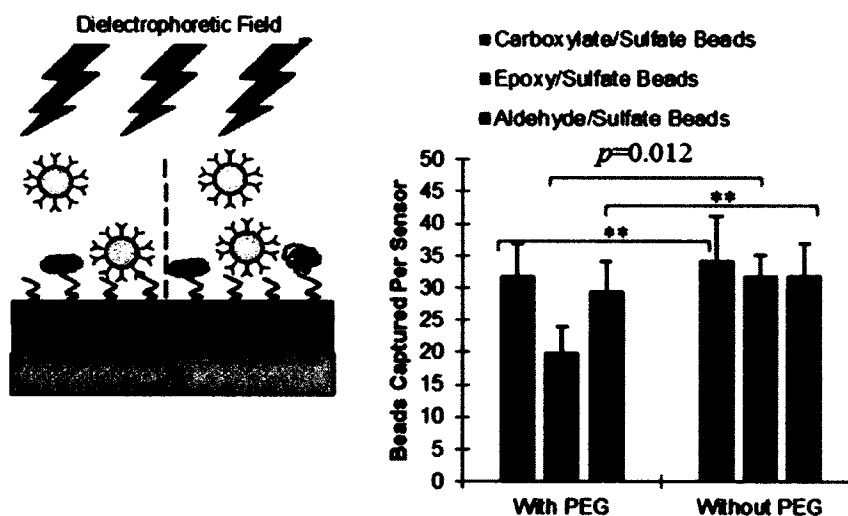


Figure. 4-23 The non-specific capture test of anti-mouse IgG functionalized microspheres on BD-UNCD surface with or without PEG immobilization with DEP applied. (** represents $p > 0.05$)

Table 4-2. Specificity of capture calculated from data in Figure 4-20, 4-21, 4-22, and 4-23.

Bead Type	without DEP		with DEP	
	without PEG on Bead	with PEG on Bead	without PEG on Bead	with PEG on Bead
Epoxy-/Sulfate	78±5.6%	86±6.7%	81±5.4%	85±5.8%
Aldehyde-/Sulfate	72±4.0%	78±5.1%	68±5.8%	76±5.8%
Carboxylate	67±4.2%	78±4.4%	63±4.9%	80±4.9%

4.4 Conclusion

In this chapter, the co-immobilization of IgG and PEG were performed on the BD-UNCD surface, epoxy-/sulfate-, aldehyde-/sulfate-, and carboxylate- modified microsphere surface in order to reduce the non-specific binding of non-target biomolecules. With the immobilization of PEG on the bead surfaces, the capture efficiencies in isolated bacteria culture and mixed culture was increased, in addition, the capture selectivity was improved. With the presence of DEP, the specific capture is significantly increased, and at the same time with immobilization of PEG on both BD-UNCD surface and beads surface, the non-specific binding can be reduced.

CHAPTER 5

BD-UNCD IMPEDANCE BIOSENSOR MICROFABRICATION AND POTENTIAL BIOSENSING APPLICATIONS TESTING

5.1 Introduction

Electrochemical biosensors have been widely developed for many applications in food safety, environmental monitoring, detection of bacteria, and clinical chemistry due to their specificity, sensitivity, accuracy, fast respond, and portability [340-342]. Impedance spectroscopy especially focuses on investigating the electrochemical properties of interfaces and materials [6, 343]. Impedance spectroscopy-based biosensors [344-347] are the most suitable for detecting antigens [348-350], because of to the simplicity in transducing the detection signal and high sensitivity in monitoring bimolecular interactions at the interface. In impedance measurements, an AC current with a sinusoidal signal $v(t) = V_m \sin(\omega t)$ are applying to the electrodes, and generating a current $i(t) = I_m \sin(\omega t + \theta)$ is measured. The ration of $v(t)/i(t)$ at a particular frequency is defined as impedance (Z) of the cell. The V_m and I_m are the amplitude of voltage and current, respect. The ω is the frequency, and θ is the phase. This measurement is performed through a range of frequency to generate the changing of impedance as a function of frequency, $Z(\omega)$. The experimental impedance data then need to be fit into an equivalent circuit for investigating the electrode surface behavior. In impedance biosensors, the antigens binding to the sensor surface, which is functionalized with biomolecules (enzyme, antibody, aptamer, and DNA), result in the changing of

impedance. Long *et al.* have reported to fit the changing impedance data into a Randles circuit, which consists of an uncompensated resistance (R_s) in series with a charge transfer resistance (R_{ct}) of a faradic reaction and the parallel combination of the capacitance (C) [343]. The concentration of antigen binding influences the changes in transfer resistance (R_{ct}), which provides the quantity information of binding antigen. However, a Randles circuit was too simple to present the real electrochemical systems, and did not describe the physical change on the electrodes surfaces properly, which will lead to the misunderstanding of experimental data. In this chapter, first, a new equivalent circuit was presented which will fit the physical meaning of each element of our biosensor. Each element in the circuit is quantified as the changing in physical properties.

Secondly, boron-doped ultra nanocrystalline diamond has been chosen as the material for fabricating biosensors. Although, silicon surfaces have been attractive to create the biomolecule-materials interface in the initial microfabricated biosensors due to the potential reduced manufacturing costs from mass-production by the existing semiconductor industry[351]; however, the poor chemical instability of silicon surface and surface chemistry in saline solutions create a need for an alternative substrate material. In contrast, diamond is well known for its extremely chemically stable electrode material with a large electrochemical potential window, reduced non-specific binding of protein, low noise to signal ratio results low detection limit, dimensional stable and the ability to regenerate surface multiple cycles [14, 39, 60, 352-355]. Yang *et al.* has developed label-free diamond-based biosensor and field-effect transistor for monitoring of DNA hybridization and protein-protein binding [201, 269]. Fujishima *et al.* have shown an enhanced detection limit of hydrogen peroxide and bisphenol A[231, 233]. The

electrochemical detection of complementary DNA was reported by Nebel *et al.* with a detection limit of 10 pM with nanostructuring of the diamond electrodes with extended nanowires, which is 100 times smaller than the detection limit of gold electrodes[271]. Also, the diamond coating surface has been reported as biocompatible in dental implants[356], vivo studies on orthopedic[272, 273] and vitro studies[109, 112, 277]. Moreover, thin diamond films can now be deposited on silicon and other microelectronic compatible substrates by chemical deposition processes readily integrable with other semiconductor practices [15]. With the invention of conducting diamond material, which is doped with boron, makes diamond an even more attractive material for biosensing applications. In this chapter, a 3×3 array of BD-UNCD interdigitated microelectrodes impedance biosensor was presented to monitor the changes between electrodes and multiple mediums for the potential biosensing applications.

5.2 Materials and Methods

5.2.1 Materials

The boron-doped ultracrystalline diamond (BD-UNCD) wafer with 2 μm diamond film with resistivity of $< 0.1 \Omega \cdot \text{cm}$ on a 2 μm thick silicon dioxide and 500 μm thick silicon wafer was acquired from Advanced Diamond Technology. All stock solutions were prepared by deionized (DI) water with a minimum resistivity of 18.0 M Ω -cm. Phosphate-buffered solution (PBS), PBS with 0.1% Tween 20 (PBS-T20), casein blocking buffer and bovine serum albumin (BSA) were bought from AMRESCO. FITC-labeled goat anti-mouse IgG were obtained from Jackson ImmunoResearch.

5.2.2 BD-UNCD impedance biosensor fabrication

As shown in Figure 5-1, the first step in the BD-UNCD impedance biosensor fabrication, the BD-UNCD wafer with 2 μm thick BD-UNCD film was sent to the University of Texas at Dallas to deposit 1 μm thick silicon dioxide film as the mask (Figure 5-1B) for dry etching BD-UNCD film. However, the adhesion force between BD-UNCD film and silicon dioxide film is weak. The BD-UNCD film is pre-treated with $\text{H}_2\text{SO}_4:\text{H}_2\text{O}_2$ (v/v) = 3:1 at 120 $^\circ\text{C}$ for 10 min to have the BD-UNCD with $-\text{OH}$ group terminated. The $-\text{OH}$ group terminated BD-UNCD surface can increase the adhesion force for silicon dioxide deposition to avoid peeling-off of the silicon dioxide film. The silicon dioxide is deposited via Unaxis 790 PECVD system at 250 $^\circ\text{C}$, pressure 900 mTorr, 400 sccm of 2% SiH_4 in He and 900 sccm of N_2O , with 50 W power for 30 min (growth rate 35 nm/min). After silicon dioxide deposition, a regular photolithography process using SPR-220-4A positive photoresist was performed to generate the mask for silicon dioxide etching, which will become the pattern of impedance biosensor. The photoresist pattern wafer was transfer into a RIE system for drying etching silicon dioxide film with 56 sccm of CHF_3 at 35 mTorr using 200 W power for total 50 min process (5 min \times 10 times to prevent overheat of the photoresist) at etching rate of 22.8 nm/min, as shown in Figure 5-1C. The BD-UNCD film is etched using ICP-RIE system (silicon dioxide as mask) with O_2 plasma with 50 sccm of O_2 at 50 mTorr using 1800 W RF power and 100 W substrate power, which has the etching rate of 50 nm/min, for 40 min. The silicon dioxide mask was removed with 7:1 buffered oxide etchant (BOE), as shown in Figure 5-1D. The BD-UNCD pattern was covered with 500 nm thick silicon dioxide layer which was deposit using a PECVD system in the University of Texas at

Dallas, as shown in Figure 5-1E. The sensor electrodes and connection fingers was exposed by etching the silicon dioxide which was patterned using a regular photolithography process (S1813 positive photoresist as the mask), as shown in Figure 5-1F.

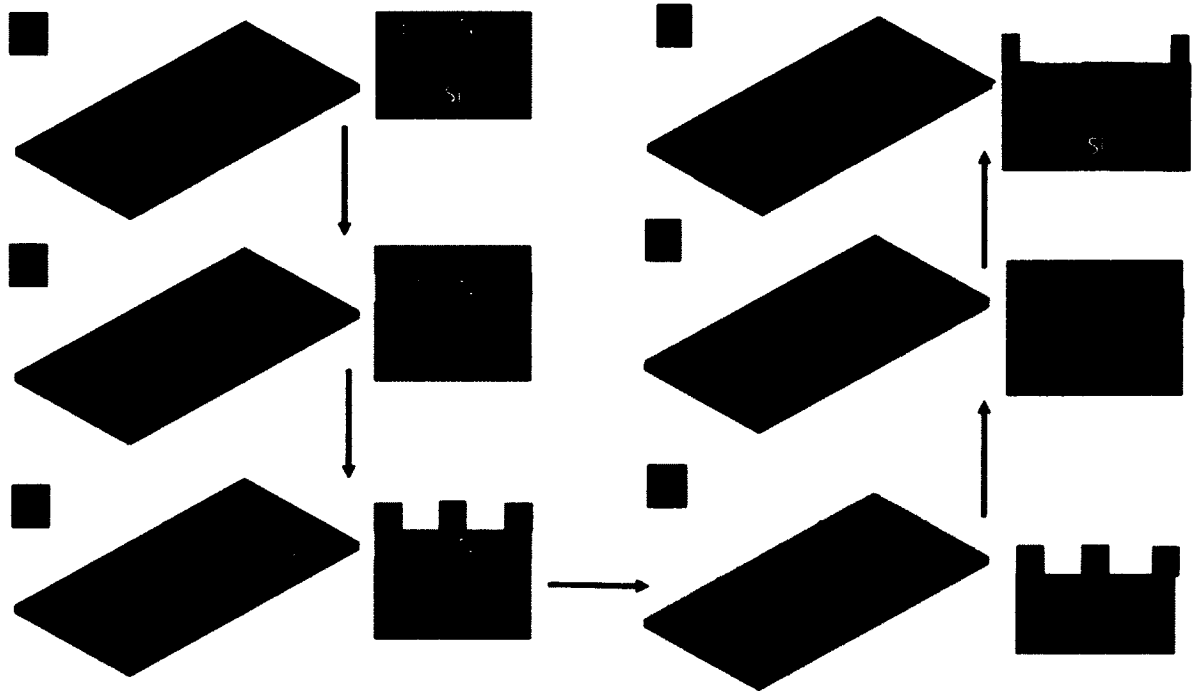


Figure 5-1. Process flow of fabricating BD-UNCD impedance sensor. (A) 2 μm thick BD-UNCD film on 525 μm thick silicon wafer which has 1 μm thick silicon dioxide on it, (B) 1 μm thick silicon dioxide was deposit on BD-UNCD film via PECVD, (C) the wafer processed through regular photolithography and buffered oxide etching process to generate patterns on silicon dioxide, (D) the silicon dioxide patterns were used as mask to etch BD-UNCD film in ICP-RIE system and removed with BOE after etching BD-UNCD film, (E) 500 nm silicon dioxide was deposit on the wafer via PECVD as an insulation layer, (F) a regular photolithography and buffered oxide etching process were performed to open the windows on sensor electrodes parts and connection fingers parts.

5.2.3 Coimmobilization of FITC-labeled goat anti-mouse IgG and PEG on BD-UNCD

Obtained BD-UNCD wafer was diced into 12 mm x 16 mm chips. Subsequently each BD-UNCD chip (12×16 mm) was first rinsed with acetone, IPA, DI water, and dried with nitrogen. Trifluoroacetamide-protected 10-aminodec-1-ene (TFAAD) was custom synthesized was mixed with 1-dodecene in 2:1 ratio (v/v) as the functionalization mix. The 1-dodecene provides space for TFAAD molecules and enhances the efficiency of deprotection. The photochemical attachment was carried out in a nitrogen purged reaction chamber. The functionalization mix was applied uniformly between the BD-UNCD surface and a piranha-cleaned quartz slide at about 2 $\mu\text{L}/\text{cm}^2$, then radiated with 254 nm UV at $\sim 2 \text{ mW}/\text{cm}^2$ for 8 h. Excess reaction mix was removed by sonicating the chip in chloroform and isopropyl alcohol for 5 minutes. The TFAAD attached BD-UNCD film was deprotected in a tightly-sealed vial containing 65 mM sodium borohydride in anhydrous methanol solution. The solution was incubated for 6 h at 70 °C to create a primary amine group termination. The sample was then rinsed with DI water and dried with nitrogen. The primary amines on the sample surface were further reacted with glutaraldehyde in sodium cyanoborohydride coupling buffer at 20 °C for 4 h to yield an aldehyde group termination. The aldehyde-terminated surface was rinsed with DI water and dried with nitrogen. The functionalized surface was incubated for 18-22 h at 4 °C with a 100 $\mu\text{g}/\text{ml}$ FITC-label goat anti-mouse IgG solution. On the next day, the surface was washed with PBS-T20 twice and PBS once to remove non-specifically adsorbed antibodies. The surface was further reacted with PEG-NH₂ for 1 h at 20 °C. The basic washing routine was performed to remove non-specific absorbed PEG. The non-

specific binding sites were blocked with a casein-based blocking buffer for 1 h at 20 °C. The surface was then washed again with PBS-T20 twice and PBS once to remove loosely-bound casein.

5.2.4 Biosensor testing

Electrical connections were made using a high-density card-edge connector. Impedance measurements were made with a CompactStat (Ivium Technologies). The excitation voltage was limited to 10 mV to prevent the restructuring or delamination of the BD-UNCD electrodes, the denaturing of attached biomolecules, or electroporation of capture bacteria. The measurements were made using DI water that measured a conductivity of 3.95 $\mu\text{S}/\text{cm}$. The first impedance measurements were made when exposing the sensor to 0.001x PBS. The sensor surface was rinsing with DI water for three times. Subsequently, the sensor was exposed to 0.01x PBS and impedance measurement again. The impedance measurement was followed the sequence of mediums, 0.025x PBS, 0.05x PBS, 0.1x PBS, 0.5x PBS, 1x PBS and human serum. Between each measurement, the sensor was rinsed with DI water for three times.

5.3 Result and Discussion

Figure 5-2 below shows the camera images and microscope images of the fabricated BD-UNCD sensor with 9 IDE electrodes. During the fabrication of BD-UNCD biosensor, the BD-UNCD surface was treated with the mixture of $\text{H}_2\text{SO}_4/\text{H}_2\text{O}_2$ to gain additional adhesion force for SiO_2 deposition due to the O-termination of BD-UNCD surface. However, this process will change part of the surface H-termination group into O-termination group. Since the previously reported UV-alkene surface chemistry scheme for attaching protein on a CVD diamond surface is based on the hydrogenated carbon

atoms, the ability of immobilizing protein on the fabricated BD-UNCD biosensor surface has been tested. Figure 5-3A confirms the attachment of FITC-label goat anti-mouse IgG on the fabricated BD-UNCD sensor surfaces, compared with which on the H-terminated BD-UNCD surface, shown in Figure 5-3B. The quantification of fluorescent intensity from both of the BD-UNCD surfaces has been studied, as shown in Figure 5-4. There is no significant difference of fluorescent intensity between fabricated BD-UNCD surface and H-terminated surface ($p=0.022$), even for the negative control. In our experiment, the negative control (without UV-alkene chemistry) recorded any fluorescent from our microscope, provides the evidence of insignificant attachment of antibodies.

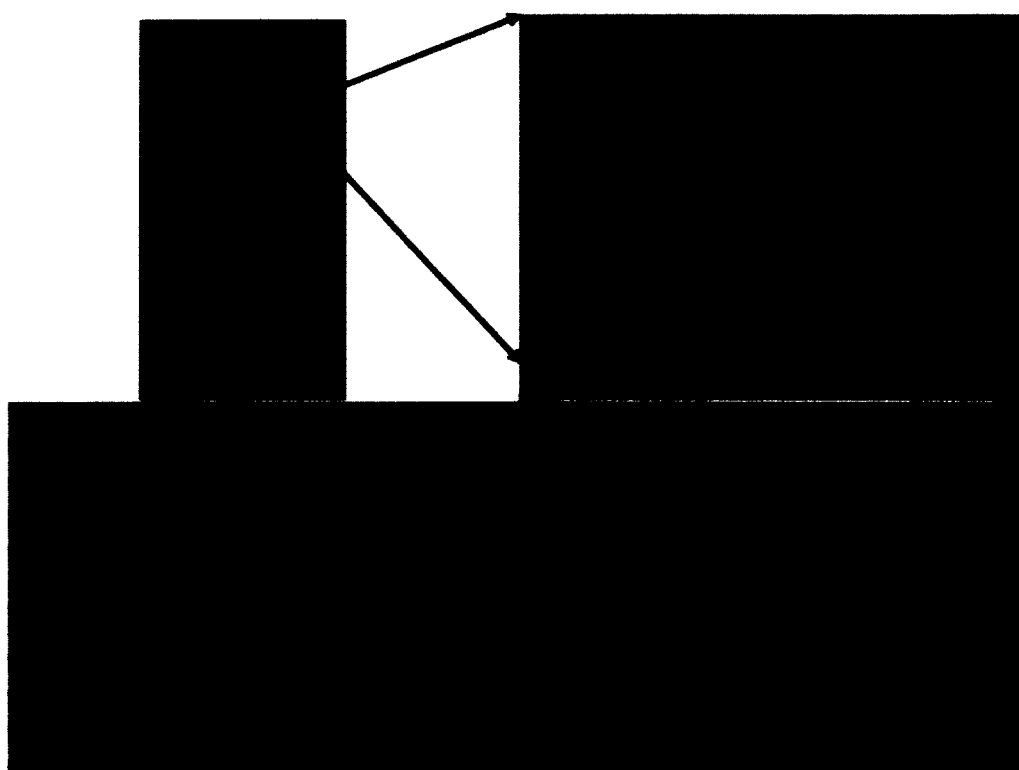


Figure 5-2. The images of fabricated BD-UNCD impedance sensor (A). The microscope images of IDE electrodes with different magnifications (B) 100x, (C) 200x, and (D) 500x.

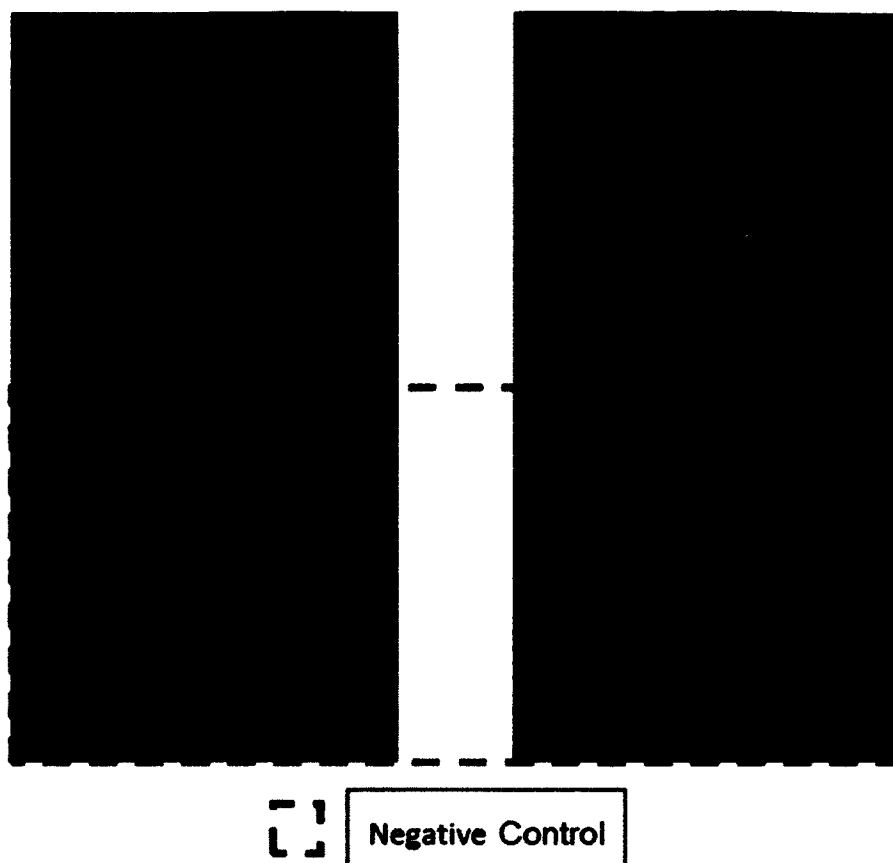


Figure 5-3. Fluorescent image of (A) fabricated BD-UNCD surface and (B) non-fabricated BD-UNCD surface with the attachment of FITC-label goat anti-mouse IgG via UV-alkene chemistry.

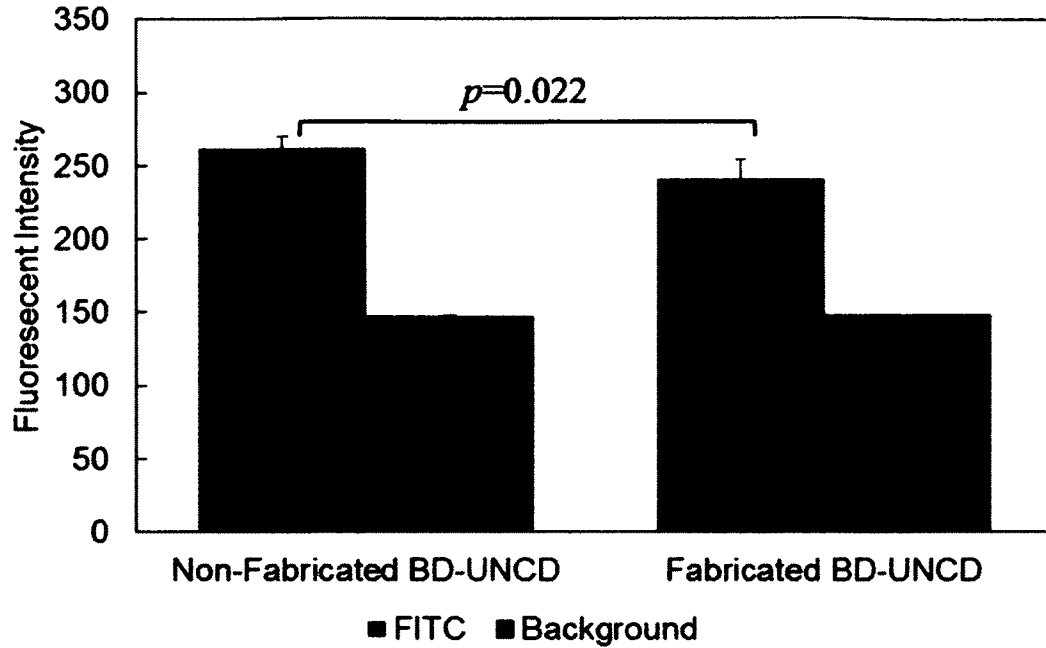
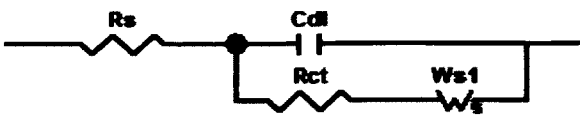
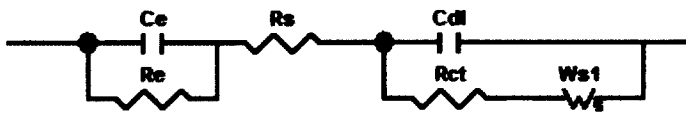
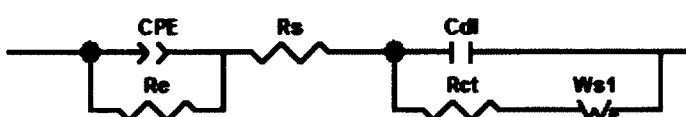

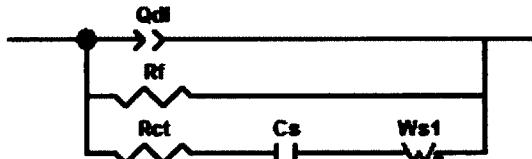
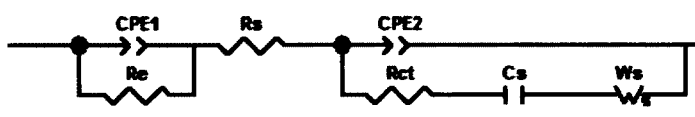



Figure 5-4. Fluorescent intensity of both surface with negative control.

Table 5-1 shows the different circuits used to fit the data obtained via impedance spectroscopy at the BD-UNCD interdigitated electrodes. Impedance spectroscopy at interdigitated electrodes is typically modeled using a Randle's circuit as shown in Table 5-1, which accounts for solution resistance (R_s), the capacitance of the double layer (C_{dl}) formed on the electrode, the resistance to diffusion of ions (W_s) through the double layer and interfacial electron transfer (R_{ct}). The diffusion of ions in the double layer modeled via a Warburg diffusion element ($Z_W = \frac{R \tanh(iT\omega)^{Phi}}{(iT\omega)^{Phi}}$, where $Phi = 0.5$) is a constant phase element (CPE), with a frequency-independent phase of 45° and with a magnitude inversely proportional to the square root of the frequency. The Nyquist plot of such a model results in a semicircle followed by a line at an angle of 45° typically.

Table 5-1. Equivalent circuit on impedance spectroscopy.

Equivalent Circuit	Notation	Reference
	R_s - Solution Resistance C_{dl} - Double layer Capacitance R_{ct} - Charge Transfer Resistance W_{s1} - Warburg Diffusion element	[357]
	C_e - Electrode capacitance R_e - Electrode Resistance	Electrode model with Randle's Circuit
	CPE - Constant Phase Element for electrode	CPE in electrode model
	$CPE2$ - Constant Phase Element for double layer effect	C_{dl} replaced by $CPE2$
	Q_{dl} - Constant Phase Element 2 for double layer R_f - Field resistance C_s - Space Charge Capacitance	[358]
	C_s - Space Charge Capacitance	Modified Circuit model
	QPE - Constant Phase Element 2	[92]

The Randle's equivalent circuit is one of the simplest possible models describing processes at the electrochemical interface but fails to account for electrode capacitance and resistance. BD-UNCD films are non-homogeneous in nature, composed of 5-10 nm grains with boron dopant mostly present at the grain boundaries. Such doped semi-

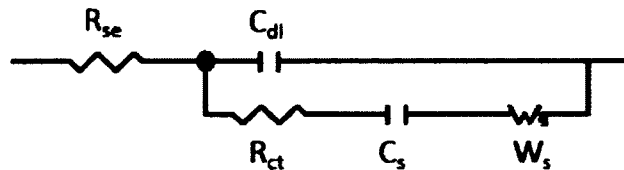
conducting electrodes can be modeled as a capacitor representing the bulk of the BD-UNCD grain in parallel with a resistor that represents the conducting pathway along the grain boundaries[359]. Thus, circuit 2 shown in Table 5-1 was tried, as well as circuits 3 and 4, which were modification of circuit 2 replacing either the electrode capacitance or the double layer capacitance with a *CPE* to account for anomalous relaxation effects. The *CPE* ($Z_{CPE} = \frac{1}{T (i\omega)^{Phi}}$) is a simple distributed element which produces impedance having a constant phase angle in the complex plane. In this model, the *CPE* acts as a capacitor if $Phi > 0.5$, as resistor if $Phi < 0.5$ and as inductor if $Phi = -1$.

Recently Siddiqui *et al.* proposed an equivalent circuit for BD-UNCD electrodes where two modified constant phase elements (*CPEs*) were used for modeling the double layer, the diffusion of ions and the solution resistance as shown in circuit 7 [92]. This model does not use a separate charge transfer resistance (R_{ct}) as in Randle's circuit, but this lumps it with the *CPEs* as modified *CPEs* ($Z_{CPE2} = \frac{R}{(i R T \omega)^{Phi}}$).

With semiconducting electrodes, the charges at the surface of the electrode can often be separated to form a space-charge region that controls the flow of electrons. In case of BD-UNCD, the surface is typically hydrogenated as deposited. However, during photolithography and reactive ion etching process, the BD-UNCD surfaces are oxygenated to form carboxylate, alcohol or aldehyde terminations. These surface states can lead to formation of a space-charge region within the electrode, which is often modeled using a capacitor in parallel with charge transfer resistance. Van de Lagemaat *et al.* modeled their homoepitaxial CVD diamond electrode with 'oxidized' surface as the circuit 5 shown in Table 5-1 with a capacitance (C_s) modeling the space charge

region[358]. A modification of circuit 4 with the C_s in series with the R_{ct} was tested as shown in circuit 6.

While all the circuits above failed to model our data, the data best fit with a modified Randle's circuit placing C_s in series with the R_{ct} as shown in Figure 5-5. The Z arising from C_e and $CPE1$ was high, suggesting the neglect of such elements and lumping the R_e and R_s into a single element. From Nyquist plots shown in Figure 5-6, incongruity is found on impedance data patterns for sensor 7 and 8 compared with those obtained from other sensors.



- R_{se} – Solution and electrode resistance
- C_{dl} – Double layer Capacitance
- R_{ct} – Charge transfer resistance
- C_s – Space charge capacitance
- W_s – Warburg short circuit diffusion element
- W_s – Consists of three components:
 - W_s -R – Resistance
 - W_s -T – Time constant or capacitance
 - W_s -P – Exponent

Figure 5-5. Equivalent circuit diagram for curve fit using impedance spectroscopy.

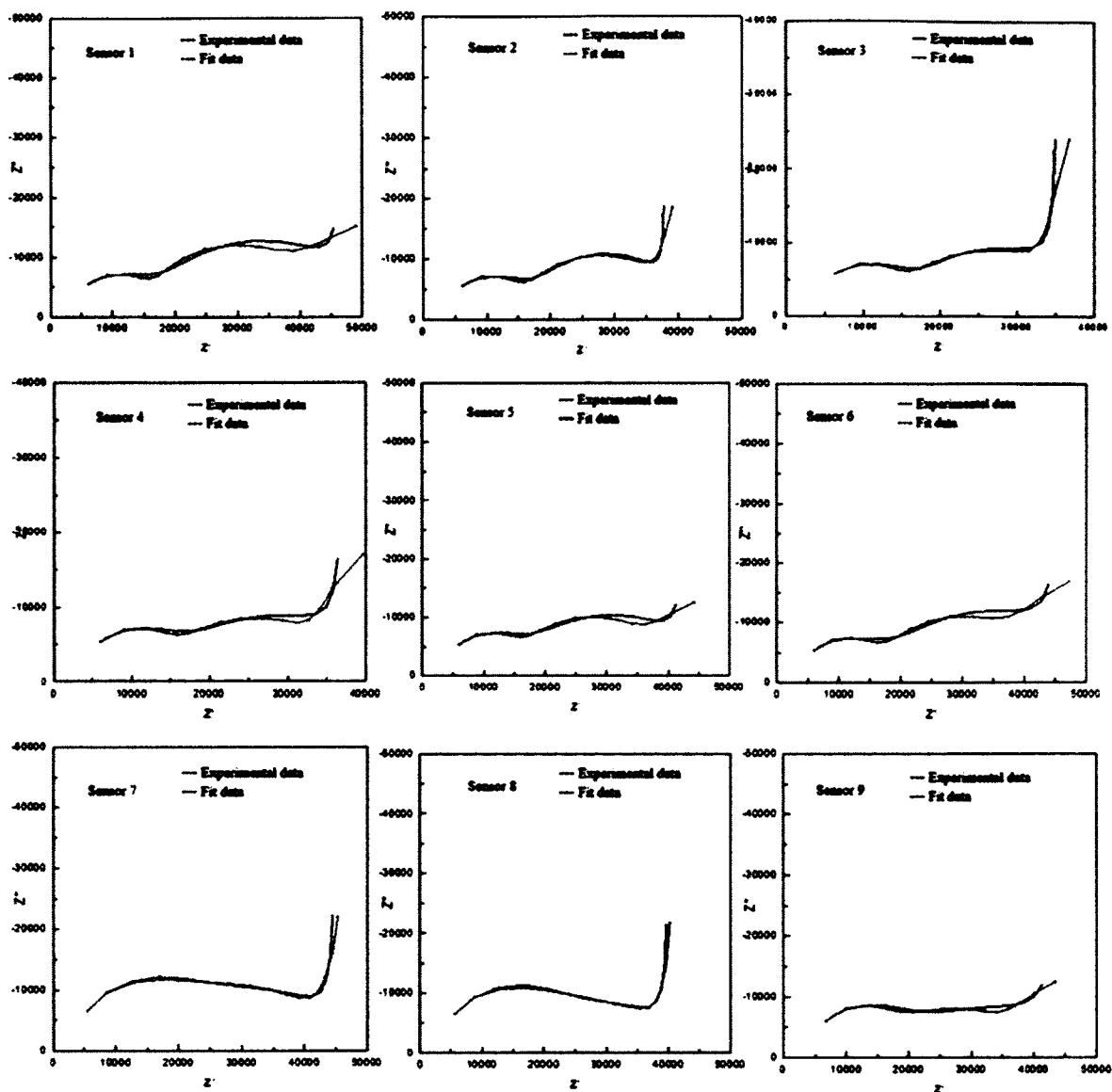


Figure 5-6. Nyquist Plots on impedance spectroscopy obtained from nine sensors (for 0.1xPBS).

From Figure 5-7, the chart on charge transfer resistance on all nine sensors infers the malfunction of sensor 7 and 8 due to electrode surface damage as they are exhibiting high resistance beyond the average with the corresponding values from other sensors. In Figure 5-8, it shows Bode Plots on nine sensors for 0.1xPBS. Figure 5-9 to 5-14 shows Parameter plots, Figure 5-9 electrode resistance, Figure 5-10 double layer capacitance,

Figure 5-11 space charge capacitance, Figure 5-12 Warburg resistance, Figure 5-13 Warburg parameter $W1-T$, and Figure 5-14 Warburg parameter $W1-P$ for all nine sensors in 0.1x PBS.

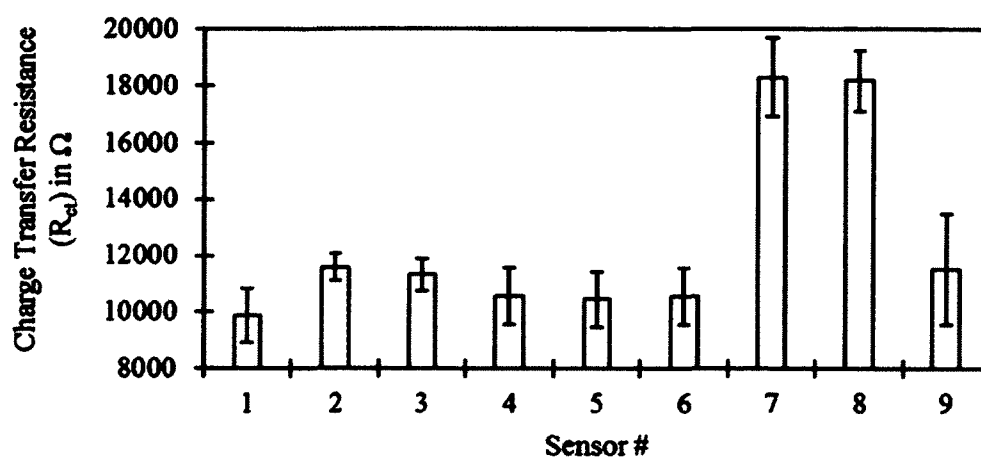


Figure 5-7. Charge transfer resistance (R_{ct}) in ohm obtained for all nine sensors.

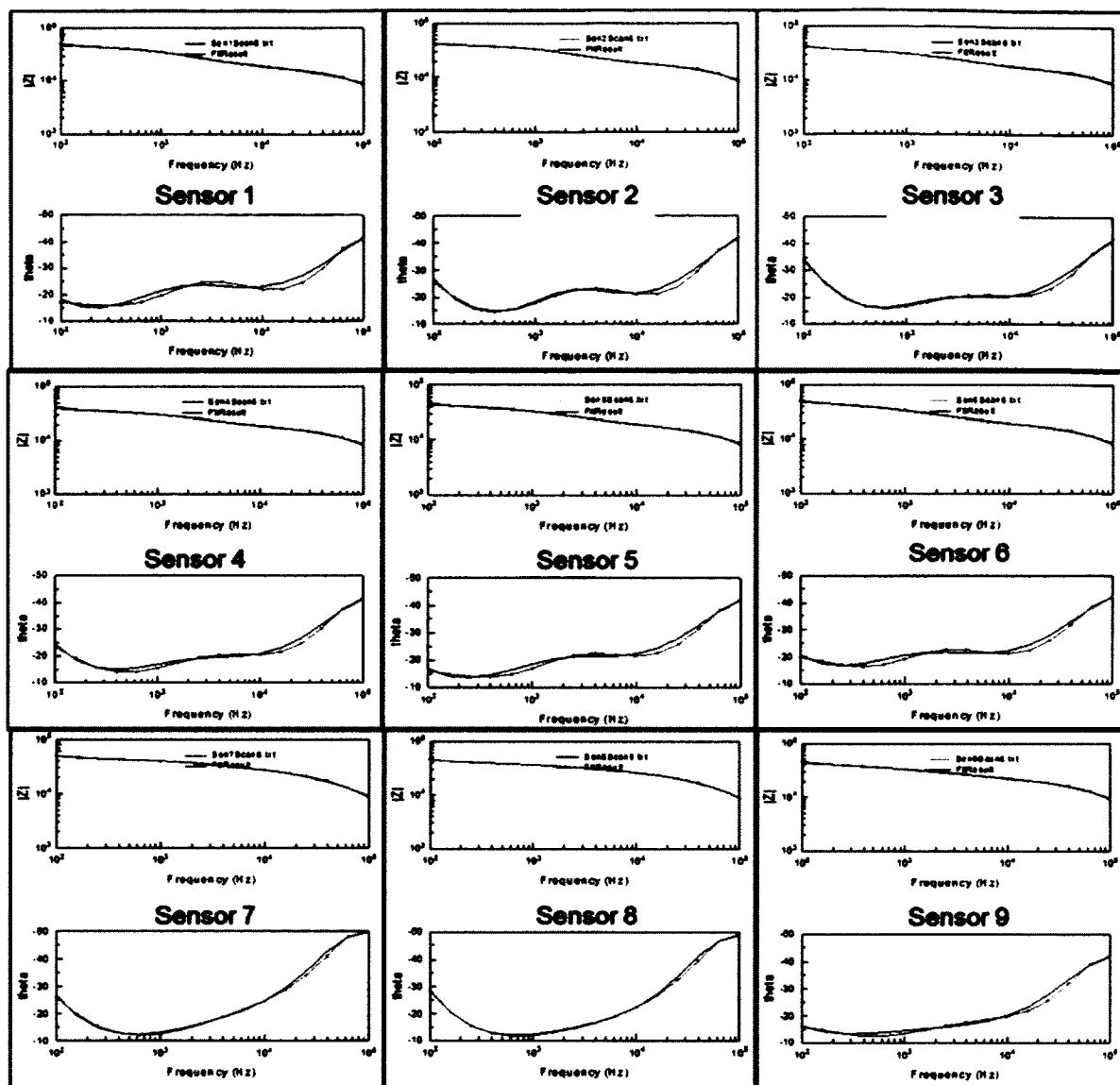


Figure 5-8. Bode Plots on nine sensors for 0.1xPBS

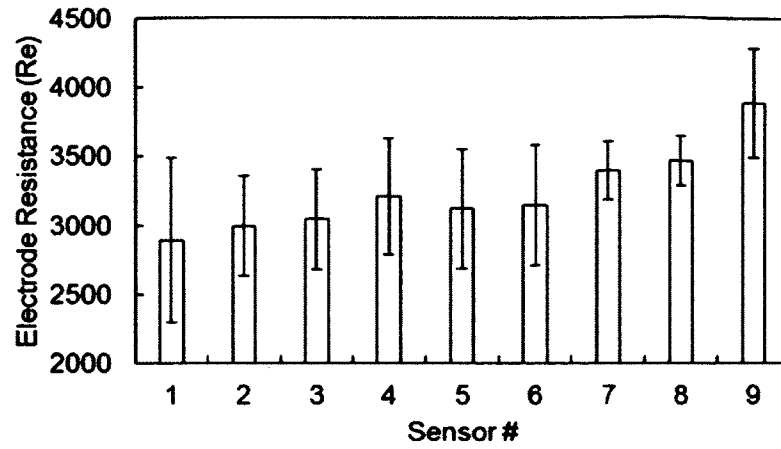


Figure 5-9. Parameter plots, electrode resistance for all nine sensors in 0.1x PBS.

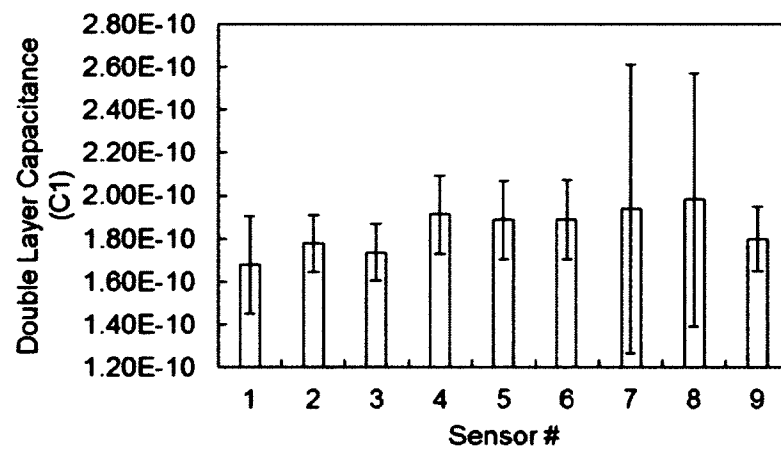


Figure 5-10. Parameter plots, double layer capacitance, (C) space charge capacitance W1-P for all nine sensors in 0.1x PBS.

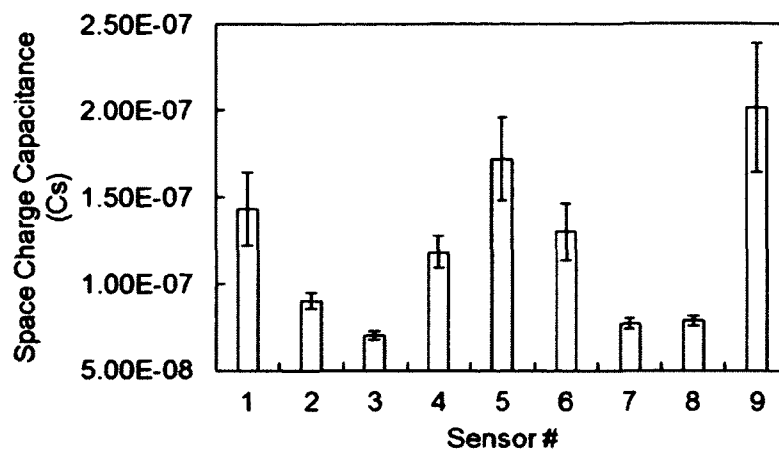


Figure 5-11. Parameter plots, space charge capacitance parameter for all nine sensors in 0.1x PBS.

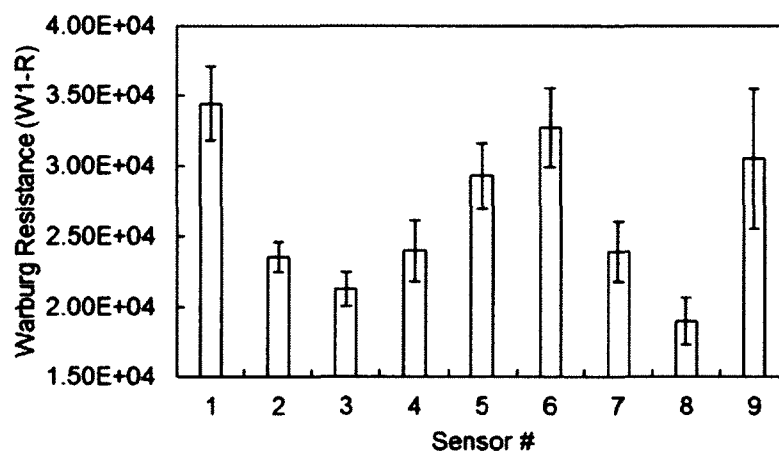


Figure 5-12. Parameter plots, Warburg resistance for all nine sensors in 0.1x PBS.

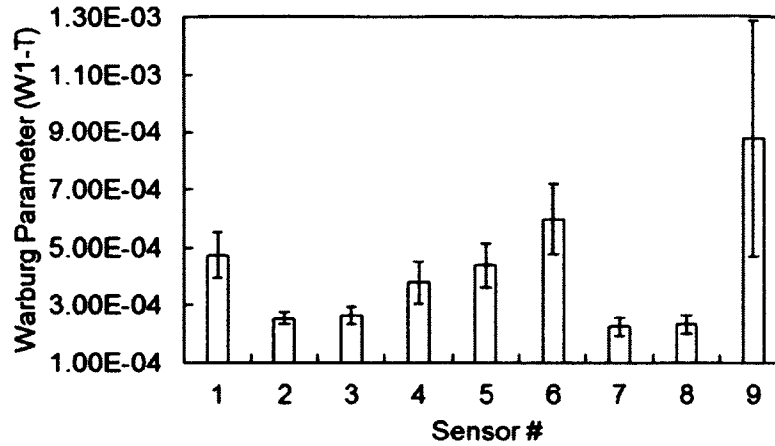


Figure 5-13. Parameter plots, Warburg parameter W1-T for all nine sensors in 0.1x PBS.

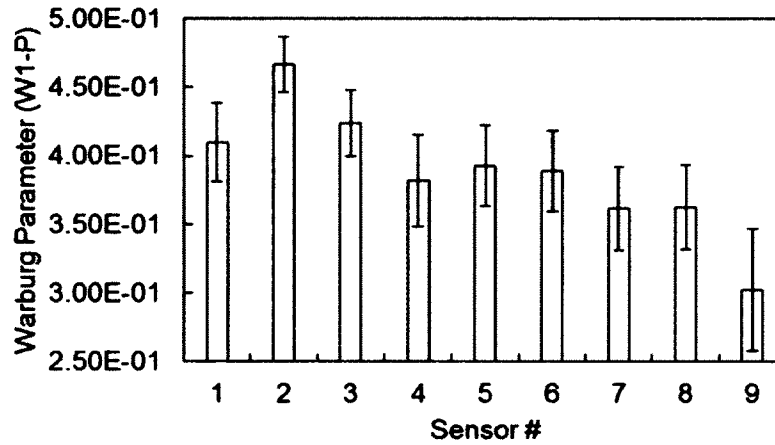


Figure 5-14. Parameter plots, Warburg parameter W1-P for all nine sensors in 0.1x PBS.

5.4 Conclusion

In this chapter, a BD-UNCD based IDE microelectrodes impedance sensor was developed, and test for potential biosensing applications. A new simulation model has been developed to fit the impedance measurement of this sensor. The impedance change of the sensor was demonstrated in different concentration of PBS solution with different solution conductivities to test the working properties of those sensors. The charge transfer resistance is the main parameter to determine if the sensor is working properly.

CHAPTER 6

CONCLUSION AND FUTURE WORK RECOMMENDATIONS

6.1 Conclusion

This dissertation provides meaningful insight to realizing our proposed DEP-e-MIB scheme to detect bacteria in clinical samples. The operation of the biosensor is only feasible upon realization of a unique electrode structure that can withstand DEP conditions while the sample is being flowed over the sensor and that can provide adequate sensitivity to impedance changes upon binding of the target to the bioreceptors.

Conductive diamond electrodes have a wide electrochemical window for oxidation and reduction of water compared to gold electrodes and thus hold the potential to realizing the DEP-e-MIB scheme. However, such diamond electrodes have not been found conductive enough. So the process of making nanodiamond-seeded gold electrodes was tested and using such electrodes for DEP and impedance spectroscopy. Although the gold-electrodes with an ND surface coverage of nearly 35% did not hold up to the DEP conditions, these electrodes provided excellent sensitivity for impedance biosensing. Methanol forms the ideal solvent in seeding gold sensing surfaces with NDs with positive zeta potential, in comparison to solvents such as acetone, ethanol, IPA and deionized water. Further, the seeding has to be performed in solutions with higher ND concentration and for seeding times as long as 30 minutes to produce maximum surface coverage, and to consecutively achieve maximum bacterial capture density. These NDs

with positive zeta potential can be functionalized with the UV-alkene chemistry without further reduction step. NDs when seeded at a 3x3 interdigitated electrode array, act as electrically conductive islands between the electrodes and reduce the effective gap between the electrodes, thus allowing to perform impedance spectroscopy in solutions with low electrical conductivity such as ITS. This ND seeding procedure along with the UV-alkene chemistry is applicable to a wide range of sensing methodologies, including quartz crystal microbalance, surface plasmon resonance, microarray technology, and electrochemical sensing. Bacterial sensing can be performed in ITS and the changes obtained in resistance to charge transfer with bacterial capture is nearly twice than that obtained with plain electrodes.

Next, the use of boron-doped ultra nanocrystalline diamond electrodes for DEP was tested without actually fabricating a 3x3 interdigitated electrode array out it. When using a flat BD-UNCD electrode in a microfluidic channel, it was difficult to apply adequate DEP force on bacteria and hence the need to use immunolatex beads as a DEP tag to apply more force on the bacteria and also help purify bacteria from sample was realized. All bead-based assays are plagued with non-specific binding and hence the effect of bead bioconjugation chemistry, bead PEGylation, and PEGylation of BD-UNCD surface were examined. When performing tagging and isolation of bacteria from isolated cultures of *E. coli O157:H7*, PEGylation of the beads only increases the capture (isolation) efficiency in case of carboxy-modified beads. Whereas when performing tagging and isolation of bacteria from mixed cultures of *E. coli O157:H7* and *E. coli K12*, PEGylation of the beads does not influence the capture efficiency or selectivity. The following was found with different types of beads without PEGylation. The PEGylation

of the BD-UNCD electrode does not impact the specific capture regardless the type of bead, however the non-specific capture of epoxy-/sulfate- beads was found to decrease, while that for the carboxylate and aldehyde-/sulfate- beads was found to be statistically similar. The presence of DEP was found to amplify any differences in capture or non-specific capture of beads on the PEGylated and non-PEGylated BD-UNCD surfaces. Application of DEP led to higher specific captures of epoxy-/sulfate- beads overall, regardless of the PEGylation condition of the BD-UNCD. The following was found with the BD-UNCD surface PEGylated. In the absence of DEP or PEGylation of beads, specific binding is not statistically different between the beads with different bioconjugation chemistry, however, the non-specific binding was found to be lower for the epoxy-/sulfate- and aldehyde-/sulfate- chemistries compared to the carboxylate modified beads. On application of DEP, the differences in specific and non-specific capture amplified causing clear differences amongst the beads with different bioconjugation chemistries. In the absence of DEP, PEGylation of beads does not affect the specific capture of the beads, however it reduces the non-specific capture of the beads. This holds true also in the presence of DEP. Overall, for each type of bead, DEP is found to increase the specific capture as well as non-specific capture of the beads, regardless of the PEGylation conditions.

At last, a BD-UNCD based 3x3 IDE microelectrodes array sensor was developed, and tested for potential biosensing applications. After inspecting the fluorescent intensity from the immobilized fluorescent-labeled antibodies on the fabricated and non-fabricated BD-UNCD surface, the patterned BD-UNCD surface can be immobilized with antibody as good as deposited BD-UNCD surface. The impedance spectroscopy data obtained

using BD-UNCD IDEs in 0.1X PBS was acquired, and an equivalent circuit model has been identified to fit this data. Examining sensors with high charge transfer resistance allows identifying sensors that might not provide adequate sensitivity. Overall the charge transfer resistance and the electrode resistance were high compared to a similar structured gold IDEs. This indicates that open BD-UNCD IDEs although capable of applying DEP may not be suitable for impedance biosensing.

6.2 Future Work Recommendations

The DEP-e-MIB has been fabrication with gold, nanodiamonds-seeded gold and boron-doped ultra nanocrystalline diamond, and tested out for DEP application and impedance spectroscopy. Gold and ND-seeded gold IDEs cannot be used for DEP application due to electrode damage from electrolysis and joule heating, however BD-UNCD IDEs are suitable for application of DEP but its relatively high electrode resistant and charge transfer resistance make it less sensitive for impedance spectroscopy. For future work, a new design of DEP-e-MIB was recommended as shown in Figure 6-1A. Here the IDEs and the wiring would be made with gold, and only the IDEs will be selectively covered with 200 nm thick BD-UNCD as shown in Figure 6-1B. This protects the gold from getting damaged from electrolysis. Another advantage of such design is that the electrode resistance will be lower compared to our BD-UNCD IDEs and hence enable impedance spectroscopy.

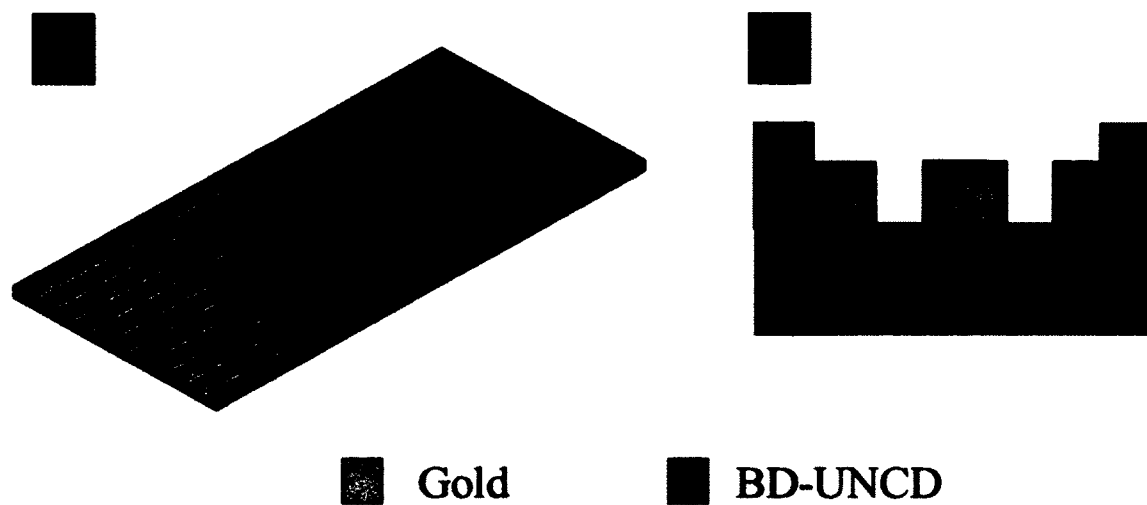


Figure 6-1. (A) Scheme of the new design of DEP-e-MIB, and (B) cross view of IDE.

REFERENCES

1. Collings, A.F.C., F., *Biosensors: recent advances*. Rep. Prog. Phys. , 1997. **60**: p. 1397-1445.
2. Suehiro, J., A. Ohtsubo, T. Hatano and M. Hara, *Selective detection of bacteria by a dielectrophoretic impedance measurement method using an antibody-immobilized electrode chip*. Sensors and Actuators B: Chemical, 2006. **119**(1): p. 319-326.
3. Magliulo, M., P. Simoni, M. Guardigli, E. Michelini, M. Luciani, R. Lelli and A. Roda, *A Rapid Multiplexed Chemiluminescent Immunoassay for the Detection of Escherichia coli O157:H7, Yersinia enterocolitica, Salmonella typhimurium, and Listeria monocytogenes Pathogen Bacteria*. Journal of Agricultural and Food Chemistry, 2007. **55**(13): p. 4933-4939.
4. Lum, J., R. Wang, K. Lassiter, B. Srinivasan, D. Abi-Ghanem, L. Berghman, B. Hargis, S. Tung, H. Lu and Y. Li, *Rapid detection of avian influenza H5N1 virus using impedance measurement of immuno-reaction coupled with RBC amplification*. Biosensors and Bioelectronics, 2012. **38**(1): p. 67-73.
5. Dijkma, M., B. Kamp, J.C. Hoogvliet and W.P. van Bennekom, *Development of an Electrochemical Immunosensor for Direct Detection of Interferon- γ at the Attomolar Level*. Analytical Chemistry, 2001. **73**(5): p. 901-907.
6. Ma, K.-S., H. Zhou, J. Zoval and M. Madou, *DNA hybridization detection by label free versus impedance amplifying label with impedance spectroscopy*. Sensors and Actuators B: Chemical, 2006. **114**(1): p. 58-64.
7. Gagnon, Z.R., *Cellular dielectrophoresis: applications to the characterization, manipulation, separation and patterning of cells*. Electrophoresis, 2011. **32**(18): p. 2466-2487.
8. Ramón-Azcón, J., T. Yasukawa, H.J. Lee, T. Matsue, F. Sánchez-Baeza, M.-P. Marco and F. Mizutani, *Competitive multi-immunosensing of pesticides based on the particle manipulation with negative dielectrophoresis*. Biosensors and Bioelectronics, 2010. **25**(8): p. 1928-1933.
9. Lee, H.J., T. Yasukawa, H. Shiku and T. Matsue, *Rapid and separation-free sandwich immunosensing based on accumulation of microbeads by negative-dielectrophoresis*. Biosensors and Bioelectronics, 2008. **24**(4): p. 1000-1005.

10. Zou, Z., S. Lee and C.H. Ahn, *A polymer microfluidic chip with interdigitated electrodes arrays for simultaneous dielectrophoretic manipulation and impedimetric detection of microparticles*. Sensors Journal, IEEE, 2008. **8**(5): p. 527-535.
11. Cheng, I.-F., H.-C. Chang, D. Hou and H.-C. Chang, *An integrated dielectrophoretic chip for continuous bioparticle filtering, focusing, sorting, trapping, and detecting*. Biomicrofluidics, 2007. **1**(2): p. 021503.
12. Granger, M.C.e.a., *Standard electrochemical behavior of high-quality, boron-doped polycrystalline diamond thin-film electrodes.*. Anal. Chem. , 2000. **72** p. 3793–3804.
13. Swain, G.M.R., M. , *The electrochemical activity of boron-doped polycrystalline diamond thin-film electrodes*. Anal. Chem. , 1993. **65**: p. 345-351.
14. Christoph, E.N., R. Bohuslav, S. Dongchan, U. Hiroshi and Y. Nianjun, *Diamond for Bio-sensor Applications*. Journal of Physics D: Applied Physics, 2007. **40**(20): p. 6443.
15. Corrigan, T.D., Krauss, A. R., Gruen, D. M., Auciello, O. & Chang, R. P. H., *Low temperature growth of ultrananocrystalline diamond on glass substrates for field emission applications*. . Mater. Res. Soc. Symp. Proc. , 2000. **593**: p. 233–236.
16. Wang, X., J. Wang, H. Cheng, P. Yu, J. Ye and L. Mao, *Graphene as a spacer to layer-by-layer assemble electrochemically functionalized nanostructures for molecular bioelectronic devices*. Langmuir, 2011. **27**(17): p. 11180-6.
17. Hartl, A., E. Schmich, J.A. Garrido, J. Hernando, S.C. Catharino, S. Walter, P. Feulner, A. Kromka, D. Steinmuller and M. Stutzmann, *Protein-modified nanocrystalline diamond thin films for biosensor applications*. Nat Mater, 2004. **3**(10): p. 736-42.
18. Radadia, A.D., C.J. Stavis, R. Carr, H. Zeng, W.P. King, J.A. Carlisle, A. Aksimentiev, R.J. Hamers and R. Bashir, *Control of Nanoscale Environment to Improve Stability of Immobilized Proteins on Diamond Surfaces*. Adv Funct Mater, 2011. **21**(6): p. 1040-1050.
19. Yang, W., O. Auciello, J.E. Butler, W. Cai, J.A. Carlisle, J.E. Gerbi, D.M. Gruen, T. Knickerbocker, T.L. Lasseter, J.N. Russell, Jr., L.M. Smith and R.J. Hamers, *DNA-modified nanocrystalline diamond thin-films as stable, biologically active substrates*. Nat Mater, 2002. **1**(4): p. 253-7.
20. Jacobs-Cook, A.J., *MEMS versus MOMS from a Systems Point of View*. Journal of Micromechanics and Microengineering, 1996. **6**(1): p. 148.

21. Brown, E.R., *RF-MEMS switches for reconfigurable integrated circuits*. Microwave Theory and Techniques, IEEE Transactions on, 1998. **46**(11): p. 1868-1880.
22. Verpoorte, E. and N.F. de Rooij, *Microfluidics meets MEMS*. Proceedings of the IEEE, 2003. **91**(6): p. 930-953.
23. Grill, A., *Tribology of Diamondlike Carbon and Related Materials: an Updated Review*. Surface and Coatings Technology, 1997. **94-95**(0): p. 507-513.
24. Robertson, J., *Diamond-like Amorphous Carbon*. Materials Science and Engineering: R: Reports, 2002. **37**(4-6): p. 129-281.
25. Sumant, A.V., O. Auciello, R.W. Carpick, S. Srinivasan and J.E. Butler, *Ultrananocrystalline and Nanocrystalline Diamond Thin Films for MEMS/NEMS Applications*. MRS Bulletin, 2010. **35**(04): p. 281-288.
26. Sumant, A.V., A.R. Krauss, D.M. Gruen, O. Auciello, A. Erdemir, M. Williams, A.F. Artiles and W. Adams, *Ultrananocrystalline Diamond Film as a Wear-Resistant and Protective Coating for Mechanical Seal Applications*. Tribology Transactions, 2005. **48**(1): p. 24-31.
27. Krauss, A.R., O. Auciello, M.Q. Ding, D.M. Gruen, Y. Huang, V.V. Zhirnov, E.I. Givargizov, A. Breskin, R. Chechen, E. Shefer, V. Konov, S. Pimenov, A. Karabutov, A. Rakhimov and N. Suetin, *Electron Field Emission for Ultrananocrystalline Diamond Films*. Journal of Applied Physics, 2001. **89**(5): p. 2958-2967.
28. Angus, J.C., H.A. Will and W.S. Stanko, *Growth of Diamond Seed Crystals by Vapor Deposition*. Journal of Applied Physics, 1968. **39**(6): p. 2915-2922.
29. Gruen, D.M., S. Liu, A.R. Krauss, J. Luo and X. Pan, *Fullerenes as Precursors for Diamond Film Growth without Hydrogen or Oxygen Additions*. Applied Physics Letters, 1994. **64**(12): p. 1502-1504.
30. Jiao, S., A. Sumant, M.A. Kirk, D.M. Gruen, A.R. Krauss and O. Auciello, *Microstructure of Ultrananocrystalline Diamond Films Grown by Microwave Ar-CH₄ Plasma Chemical Vapor Deposition with or without Added H₂*. Journal of Applied Physics, 2001. **90**(1): p. 118-122.
31. Birrell, J., J.A. Carlisle, O. Auciello, D.M. Gruen and J.M. Gibson, *Morphology and Electronic Structure in Nitrogen-doped Ultrananocrystalline Diamond*. Applied Physics Letters, 2002. **81**(12): p. 2235-2237.
32. Xiao, X., J. Birrell, J.E. Gerbi, O. Auciello and J.A. Carlisle, *Low Temperature Growth of Ultrananocrystalline Diamond*. Journal of Applied Physics, 2004. **96**(4): p. 2232-2239.

33. Krauss, A.R., O. Auciello, D.M. Gruen, A. Jayatissa, A. Sumant, J. Tucek, D.C. Mancini, N. Moldovan, A. Erdemir, D. Ersoy, M.N. Gardos, H.G. Busmann, E.M. Meyer and M.Q. Ding, *Ultrananocrystalline Diamond Thin Films for MEMS and Moving Mechanical Assembly Devices*. Diamond and Related Materials, 2001. **10**(11): p. 1952-1961.
34. Orlando, A., B. James, A.C. John, E.G. Jennifer, X. Xingcheng, P. Bei and D.E. Horacio, *Materials science and fabrication processes for a new MEMS technology based on ultrananocrystalline diamond thin films*. Journal of Physics: Condensed Matter, 2004. **16**(16): p. R539.
35. Mancini, A.V.S.O.A.H.-C.Y.Z.M.R.W.C.D.C., *Large-area low-temperature ultrananocrystalline diamond (UNCD) films and integration with CMOS devices for monolithically integrated diamond MEMS/NEMS-CMOS systems*, in *Micro- and Nanotechnology Sensors, Systems, and Applications*, T.G.M.S.I.A.K. Dutta, Editor. 2009, Proc. SPIE. p. 18.
36. Carpick, V.P.A.A.V.S.S.S.C.G.O.A.J.A.C.R.W., *Temperature dependence of mechanical stiffness and dissipation in ultrananocrystalline diamond*, in *Micro- and Nanotechnology Sensors, Systems, and Applications*, T.G.M.S.I.A.K. Dutta, Editor. 2009, Proc. SPIE. p. 17.
37. Garguilo, J.M., F.A.M. Koeck, R.J. Nemanich, X.C. Xiao, J.A. Carlisle and O. Auciello, *Thermionic Field Emission from Nanocrystalline Diamond-coated Silicon Tip Arrays*. Physical Review B, 2005. **72**(16): p. 165404.
38. Xiao, X., J. Wang, C. Liu, J.A. Carlisle, B. Mech, R. Greenberg, D. Guven, R. Freda, M.S. Humayun, J. Weiland and O. Auciello, *In vitro and in vivo Evaluation of Ultrananocrystalline Diamond for Coating of Implantable Retinal Microchips*. Journal of Biomedical Materials Research Part B: Applied Biomaterials, 2006. **77B**(2): p. 273-281.
39. Yang, W., O. Auciello, J.E. Butler, W. Cai, J.A. Carlisle, J.E. Gerbi, D.M. Gruen, T. Knickerbocker, T.L. Lasseter, J.N. Russell, L.M. Smith and R.J. Hamers, *DNA-modified nanocrystalline diamond thin-films as stable, biologically active substrates*. Nat Mater, 2002. **1**(4): p. 253-257.
40. Kim, M.S., S. Li, R.S. Lakshmanan, R. Guntupalli, S. Huang, Z.Y. Cheng, V.A. Petrenko, J.M. Barbaree, V. Vodyanoy, B.A. Chin, S.-I. Tu and K. Chao, *Phage-based magnetoelastic biosensor for the detection of Salmonella typhimurium*. 2009. **7315**: p. 731503-731503-10.
41. Spitsyn, B.V., L.L. Bouilov and B.V. Derjaguin, *Vapor Growth of Diamond on Diamond and other Surfaces*. Journal of Crystal Growth, 1981. **52**, Part 1(0): p. 219-226.

42. Butler, J.E. and H. Windischmann, *Developments in CVD-Diamond Synthesis During the Past Decade*. MRS Bulletin, 1998. **23**(09): p. 22-27.
43. Mark A. Prelas, G.P., Louis K. Bigelow *Handbook of Industrial Diamonds and Diamond Films*. 2009, Chichester, UK: Wiley.
44. Butler, J.E. and A.V. Sumant, *The CVD of Nanodiamond Materials*. Chemical Vapor Deposition, 2008. **14**(7-8): p. 145-160.
45. Butler, J.E., A. Cheesman and M.N.R. Ashfold, *Recent Progress in the Understanding of CVD Growth of Diamond*, in *CVD Diamond for Electronic Devices and Sensors*. 2009, John Wiley & Sons, Ltd. p. 103-124.
46. S. Rotter, i.M.Y., Y. Koga, Y. Tzeng, C.P. Klages, K. Miyoshi. *Proceedings of the Applied Diamond Conference/Frontier Carbon Technologies-ADC/FCT '99*. 1999. MYU, K.K, Tokyo.
47. Philip, J., P. Hess, T. Feygelson, J.E. Butler, S. Chattopadhyay, K.H. Chen and L.C. Chen, *Elastic, Mechanical, and Thermal Properties of Nanocrystalline Diamond Films*. Journal of Applied Physics, 2003. **93**(4): p. 2164-2171.
48. Butler, J.E., R.L. Woodin, L.M. Brown and P. Fallon, *Thin Film Diamond Growth Mechanisms [and Comment]*. Vol. 342. 1993. 209-224.
49. Butler, J.E., Y.A. Mankelevich, A. Cheesman, M. Jie and M.N.R. Ashfold, *Understanding the Chemical Vapor Deposition of Diamond: Recent Progress*. Journal of Physics: Condensed Matter, 2009. **21**(36): p. 364201.
50. Kohn, E., P. Gluche and M. Adamschik, *Diamond MEMS — a New Emerging Technology*. Diamond and Related Materials, 1999. **8**(2-5): p. 934-940.
51. Sumant, A.V., P.U.P.A. Gilbert, D.S. Grierson, A.R. Konicek, M. Abrecht, J.E. Butler, T. Feygelson, S.S. Rotter and R.W. Carpick, *Surface Composition, Bonding, and Morphology in the Nucleation and Growth of Ultra-thin, High Quality Nanocrystalline Diamond Films*. Diamond and Related Materials, 2007. **16**(4-7): p. 718-724.
52. Gruen, D.M., *Nucleation, Growth, and Microstructure of Nanocrystalline Diamond Films*. MRS Bulletin, 1998. **23**(09): p. 32-35.
53. Paul, W.M., L.A. Neil, N.R.A. Michael, C.R. James and A.M. Yuri, *Simplified Monte Carlo Simulations of Chemical Vapour Deposition Diamond Growth*. Journal of Physics: Condensed Matter, 2009. **21**(36): p. 364203.
54. May, P.W., J.N. Harvey, J.A. Smith and Y.A. Mankelevich, *Reevaluation of the Mechanism for Ultrananocrystalline Diamond Deposition from Ar/CH₄/H₂ Gas Mixtures*. Journal of Applied Physics, 2006. **99**(10): p. 104907.

55. Zuiker, C.D., A.R. Krauss, D.M. Gruen, J.A. Carlisle, L.J. Terminello, S.A. Asher and R.W. Bormett, *Characterization of Diamond Thin Films by Core-Level Photoabsorption and UV Excitation Raman Spectroscopy*. MRS Online Proceedings Library, 1996. **437**: p. null-null.
56. Gruen, D.M., A.R. Krauss, C.D. Zuiker, R. Csencsits, L.J. Terminello, J.A. Carlisle, I. Jimenez, D.G.J. Sutherland, D.K. Shuh, W. Tong and F.J. Himpsel, *Characterization of Nanocrystalline Diamond Films by Core-level Photoabsorption*. Applied Physics Letters, 1996. **68**(12): p. 1640-1642.
57. Birrell, J., J.E. Gerbi, O. Auciello, J.M. Gibson, D.M. Gruen and J.A. Carlisle, *Bonding Structure in Nitrogen Doped Ultrananocrystalline Diamond*. Journal of Applied Physics, 2003. **93**(9): p. 5606-5612.
58. Achatz, P., O.A. Williams, P. Bruno, D.M. Gruen, J.A. Garrido and M. Stutzmann, *Effect of Nitrogen on the Electronic Properties of Ultrananocrystalline Diamond Thin Films Grown on Quartz and Diamond Substrates*. Physical Review B, 2006. **74**(15): p. 155429.
59. Bhattacharyya, S., O. Auciello, J. Birrell, J.A. Carlisle, L.A. Curtiss, A.N. Goyette, D.M. Gruen, A.R. Krauss, J. Schlueter, A. Sumant and P. Zapol, *Synthesis and Characterization of Highly-conducting Nitrogen-doped Ultrananocrystalline Diamond Films*. Applied Physics Letters, 2001. **79**(10): p. 1441-1443.
60. Show, Y., M.A. Witek, P. Sonthalia and G.M. Swain, *Characterization and Electrochemical Responsiveness of Boron-Doped Nanocrystalline Diamond Thin-Film Electrodes*. Chemistry of Materials, 2003. **15**(4): p. 879-888.
61. Gajewski, W., P. Achatz, O.A. Williams, K. Haenen, E. Bustarret, M. Stutzmann and J.A. Garrido, *Electronic and optical properties of boron-doped nanocrystalline diamond films*. Physical Review B, 2009. **79**(4): p. 045206.
62. Zeng, H., A.R. Konicek, N. Moldovan, F. Mangolini, T. Jacobs, I. Wylie, P.U. Arumugam, S. Siddiqui, R.W. Carpick and J.A. Carlisle, *Boron-doped Ultrananocrystalline Diamond Synthesized with an H-rich/Ar-lean Gas System*. Carbon, 2015. **84**(0): p. 103-117.
63. Katamune, Y., S. Ohmagari, H. Setoyama, K. Sumitani, Y. Hirai and T. Yoshitake, *p-Type Semiconducting Properties of Boron Doped Ultrananocrystalline Diamond/Amorphous Carbon Composite Films Prepared by Coaxial Arc Plasma Deposition*. Meeting Abstracts, 2012. **MA2012-02**(50): p. 3512.

64. Chen, Y.C., X.Y. Zhong, A.R. Konicek, D.S. Grierson, N.H. Tai, I.N. Lin, B. Kabius, J.M. Hiller, A.V. Sumant, R.W. Carpick and O. Auciello, *Synthesis and Characterization of Smooth Ultrananocrystalline Diamond Films via Low Pressure Bias-enhanced Nucleation and Growth*. Applied Physics Letters, 2008. **92**(13): p. 133113.
65. Gerber, J., S. Sattel, H. Ehrhardt, J. Robertson, P. Wurzinger and P. Pongratz, *Investigation of Bias Enhanced Nucleation of Diamond on Silicon*. Journal of Applied Physics, 1996. **79**(8): p. 4388-4396.
66. Stoner, B.R., G.H.M. Ma, S.D. Wolter and J.T. Glass, *Characterization of bias-enhanced nucleation of diamond on silicon by *\textit{in vacuo}* surface analysis and transmission electron microscopy*. Physical Review B, 1992. **45**(19): p. 11067-11084.
67. Lee, Y.-C., S.-J. Lin, C.-Y. Lin, M.-C. Yip, W. Fang and I.N. Lin, *Pre-nucleation Techniques for Enhancing Nucleation Density and Adhesion of Low Temperature Deposited Ultra-nanocrystalline Diamond*. Diamond and Related Materials, 2006. **15**(11–12): p. 2046-2050.
68. Lifshitz, Y., X.M. Meng, S.T. Lee, R. Akhvelidany and A. Hoffman, *Visualization of Diamond Nucleation and Growth from Energetic Species*. Physical Review Letters, 2004. **93**(5): p. 056101.
69. Adiga, V.P., A.V. Sumant, S. Suresh, C. Gudeman, O. Auciello, J.A. Carlisle and R.W. Carpick, *Mechanical Stiffness and Dissipation in Ultrananocrystalline Diamond Microresonators*. Physical Review B, 2009. **79**(24): p. 245403.
70. Espinosa, H.D., B. Peng, B.C. Prorok, N. Moldovan, O. Auciello, J.A. Carlisle, D.M. Gruen and D.C. Mancini, *Fracture Strength of Ultrananocrystalline Diamond Thin Films—Identification of Weibull Parameters*. Journal of Applied Physics, 2003. **94**(9): p. 6076-6084.
71. Sepulveda, N., D. Aslam and J.P. Sullivan, *Polycrystalline Diamond MEMS Resonator Technology for Sensor Applications*. Diamond and Related Materials, 2006. **15**(2–3): p. 398-403.
72. Sepulveda, N., L. Jing, D.M. Aslam and J.P. Sullivan, *High-Performance Polycrystalline Diamond Micro- and Nanoresonators*. Microelectromechanical Systems, Journal of, 2008. **17**(2): p. 473-482.
73. Sumant, A.V., D.S. Grierson, J.E. Gerbi, J. Birrell, U.D. Lanke, O. Auciello, J.A. Carlisle and R.W. Carpick, *Toward the Ultimate Tribological Interface: Surface Chemistry and Nanotribology of Ultrananocrystalline Diamond*. Advanced Materials, 2005. **17**(8): p. 1039-1045.

74. Sumant, A.V., D.S. Grierson, J.E. Gerbi, J.A. Carlisle, O. Auciello and R.W. Carpick, *Surface Chemistry and Bonding Configuration of Ultrananocrystalline Diamond Surfaces and their Effects on Nanotribological Properties*. Physical Review B, 2007. **76**(23): p. 235429.
75. Konicek, A.R., D.S. Grierson, P.U.P.A. Gilbert, W.G. Sawyer, A.V. Sumant and R.W. Carpick, *Origin of Ultralow Friction and Wear in Ultrananocrystalline Diamond*. Physical Review Letters, 2008. **100**(23): p. 235502.
76. Haenni, W., P. Rychen, M. Fryda and C. Comninellis, *Chapter 5 Industrial applications of diamond electrodes*, in *Semiconductors and Semimetals*, E.N. Christoph and R. Jürgen, Editors. 2004, Elsevier. p. 149-196.
77. Chen, Q., D.M. Gruen, A.R. Krauss, T.D. Corrigan, M. Witek and G.M. Swain, *The Structure and Electrochemical Behavior of Nitrogen-Containing Nanocrystalline Diamond Films Deposited from CH₄/N₂/Ar Mixtures*. Journal of The Electrochemical Society, 2001. **148**(1): p. E44-E51.
78. Eaton, S.C., A.B. Anderson, J.C. Angus, Y.E. Evstefeeva and Y.V. Pleskov, *Co-doping of Diamond with Boron and Sulfur*. Electrochemical and Solid-State Letters, 2002. **5**(8): p. G65-G68.
79. Vaddiraju, S., S. Eaton-Magana, J.A. Chaney and M.K. Sunkara, *UPS of Boron-Sulfur Co-Doped, n-Type Diamond*. Electrochemical and Solid-State Letters, 2004. **7**(12): p. G331-G334.
80. Milos, N., *Conventional n-type Doping in Diamond: State of the Art and Recent Progress*. Semiconductor Science and Technology, 2005. **20**(2): p. R19.
81. Swain, G.M., *Chapter 4 Electroanalytical applications of diamond electrodes*, in *Semiconductors and Semimetals*, E.N. Christoph and R. Jürgen, Editors. 2004, Elsevier. p. 121-148.
82. Balandin, A.A., *Thermal properties of graphene and nanostructured carbon materials*. Nat Mater, 2011. **10**(8): p. 569-581.
83. Gerbi, J.E., O. Auciello, J. Birrell, D.M. Gruen, B.W. Alphenaar and J.A. Carlisle, *Electrical Contacts to Ultrananocrystalline Diamond*. Applied Physics Letters, 2003. **83**(10): p. 2001-2003.
84. Beffort, O., S. Vaucher and F.A. Khalid, *On the Thermal and Chemical Stability of Diamond during Processing of Al/Diamond Composites by Liquid Metal Infiltration (squeeze casting)*. Diamond and Related Materials, 2004. **13**(10): p. 1834-1843.
85. Angus, J.C., Y.V. Pleskov and S.C. Eaton, *Chapter 3 Electrochemistry of diamond*, in *Semiconductors and Semimetals*, E.N. Christoph and R. Jürgen, Editors. 2004, Elsevier. p. 97-119.

86. Swain, G.M., A.B. Anderson and J.C. Angus, *Applications of Diamond Thin Films in Electrochemistry*. MRS Bulletin, 1998. **23**(09): p. 56-60.
87. Pelskov, Y.V., A.Y. Sakharova, M.D. Krotova, L.L. Bouilov and B.V. Spitsyn, *Photoelectrochemical Properties of Semiconductor Diamond*. Journal of Electroanalytical Chemistry and Interfacial Electrochemistry, 1987. **228**(1-2): p. 19-27.
88. Panizza, M. and G. Cerisola, *Application of Diamond Electrodes to Electrochemical Processes*. Electrochimica Acta, 2005. **51**(2): p. 191-199.
89. Fryda, M., T. Matthée, S. Mulcahy, A. Hampel, L. Schäfer and I. Tröster, *Fabrication and Application of Diachem® Electrodes*. Diamond and Related Materials, 2003. **12**(10-11): p. 1950-1956.
90. Martin, H.B., A. Argoitia, U. Landau, A.B. Anderson and J.C. Angus, *Hydrogen and Oxygen Evolution on Boron-Doped Diamond Electrodes*. Journal of The Electrochemical Society, 1996. **143**(6): p. L133-L136.
91. Katsuki, N., E. Takahashi, M. Toyoda, T. Kurosu, M. Iida, S. Wakita, Y. Nishiki and T. Shimamune, *Water Electrolysis Using Diamond Thin-Film Electrodes*. Journal of The Electrochemical Society, 1998. **145**(7): p. 2358-2362.
92. Siddiqui, S., Z. Dai, C.J. Stavis, H. Zeng, N. Moldovan, R.J. Hamers, J.A. Carlisle and P.U. Arumugam, *A Quantitative Study of Detection Mechanism of a Label-free Impedance Biosensor Using Ultrananocrystalline Diamond Microelectrode Array*. Biosensors and Bioelectronics, 2012. **35**(1): p. 284-290.
93. Karyakin, A.A., E.E. Karyakina, L. Gorton, O.A. Bobrova, L.V. Lukachova, A.K. Gladilin and A.V. Levashov, *Improvement of Electrochemical Biosensors Using Enzyme Immobilization from Water–Organic Mixtures with a High Content of Organic Solvent*. Analytical Chemistry, 1996. **68**(24): p. 4335-4341.
94. Wang, J., B. Freiha, N. Naser, E. Gonzalez Romero, U. Wollenberger, M. Ozsoz and O. Evans, *Amperometric Biosensing of Organic Peroxides with Peroxidase-modified Electrodes*. Analytica Chimica Acta, 1991. **254**(1-2): p. 81-88.
95. Iwuoha, E.I., D. Saenz de Villaverde, N.P. Garcia, M.R. Smyth and J.M. Pingarron, *Reactivities of Organic Phase Biosensors. 2. The Amperometric Behaviour of Horseradish Peroxidase Immobilised on a Platinum Electrode Modified with an Electrosynthetic Polyaniline Film*. Biosensors and Bioelectronics, 1997. **12**(8): p. 749-761.
96. Yoshimura, M., K. Honda, R. Uchikado, T. Kondo, T.N. Rao, D.A. Tryk, A. Fujishima, Y. Sakamoto, K. Yasui and H. Masuda, *Electrochemical Characterization of Nanoporous Honeycomb Diamond Electrodes in Non-aqueous Electrolytes*. Diamond and Related Materials, 2001. **10**(3-7): p. 620-626.

97. Yoshimura, M., K. Honda, T. Kondo, R. Uchikado, Y. Einaga, T.N. Rao, D.A. Tryk and A. Fujishima, *Factors Controlling the Electrochemical Potential Window for Diamond Electrodes in Non-aqueous Electrolytes*. *Diamond and Related Materials*, 2002. **11**(1): p. 67-74.
98. Pastor-Moreno, G. and D.J. Riley, *Electrochemical Studies of Moderately Boron Doped Polycrystalline Diamond in Non-aqueous Solvent*. *Electrochimica Acta*, 2002. **47**(16): p. 2589-2595.
99. Panizza, M., G. Siné, I. Duo, L. Ouattara and C. Comninellis, *Electrochemical Polishing of Boron-Doped Diamond in Organic Media*. *Electrochemical and Solid-State Letters*, 2003. **6**(12): p. D17-D19.
100. Zhang, M., T. Desai and M. Ferrari, *Proteins and Cells on PEG Immobilized Silicon Surfaces*. *Biomaterials*, 1998. **19**(10): p. 953-960.
101. Wu, Z., B. Wang, Z. Cheng, X. Yang, S. Dong and E. Wang, *A Facile Approach to Immobilize Protein for Biosensor: Self-assembled Supported Bilayer Lipid Membranes on Glassy Carbon Electrode*. *Biosensors and Bioelectronics*, 2001. **16**(1-2): p. 47-52.
102. Deinhammer, R.S., M. Ho, J.W. Anderegg and M.D. Porter, *Electrochemical Oxidation of Amine-containing Compounds: a Route to the Surface Modification of Glassy Carbon Electrodes*. *Langmuir*, 1994. **10**(4): p. 1306-1313.
103. Smith, C.I., A. Bowfield, M.C. Cuquerella, C.P. Mansley, T. Farrell, P. Harrison, D.S. Martin, D.G. Fernig, C. Edwards, J.E. Butler, R.J. Hamers, B. Sun, X. Wang and P. Weightman, *Detection of DNA Hybridisation on a Functionalised Diamond Surface Using Reflection Anisotropy Spectroscopy*. *EPL (Europhysics Letters)*, 2009. **85**(1): p. 18006.
104. Hartl, A., E. Schmich, J.A. Garrido, J. Hernando, S.C.R. Catharino, S. Walter, P. Feulner, A. Kromka, D. Steinmuller and M. Stutzmann, *Protein-modified nanocrystalline diamond thin films for biosensor applications*. *Nat Mater*, 2004. **3**(10): p. 736-742.
105. Radadia, A.D., C.J. Stavis, R. Carr, H. Zeng, W.P. King, J.A. Carlisle, A. Aksimentiev, R.J. Hamers and R. Bashir, *Control of Nanoscale Environment to Improve Stability of Immobilized Proteins on Diamond Surfaces*. *Advanced Functional Materials*, 2011. **21**(6): p. 1040-1050.
106. Specht, C.G., O.A. Williams, R.B. Jackman and R. Schoepfer, *Ordered Growth of Neurons on Diamond*. *Biomaterials*, 2004. **25**(18): p. 4073-4078.
107. Ariano, P., P. Baldelli, E. Carbone, A. Gilardino, A. Lo Giudice, D. Lovisolo, C. Manfredotti, M. Novara, H. Sternschulte and E. Vittone, *Cellular Adhesion and Neuronal Excitability on Functionalised Diamond Surfaces*. *Diamond and Related Materials*, 2005. **14**(3-7): p. 669-674.

108. Chong, K.F., K.P. Loh, S.R.K. Vedula, C.T. Lim, H. Sternschulte, D. Steinmüller, F.-s. Sheu and Y.L. Zhong, *Cell Adhesion Properties on Photochemically Functionalized Diamond*. Langmuir, 2007. **23**(10): p. 5615-5621.
109. Bajaj, P., D. Akin, A. Gupta, D. Sherman, B. Shi, O. Auciello and R. Bashir, *Ultrananocrystalline Diamond Film as an Optimal Cell Interface for Biomedical Applications*. Biomedical Microdevices, 2007. **9**(6): p. 787-794.
110. Mech, B.V. and R.J. Greenberg, *Implantable device using ultra-nanocrystalline diamond*. 2006, Google Patents.
111. Greenberg, R.J. and B.V. Mech, *Implantable microfluidic delivery system using ultra-nanocrystalline diamond coating*. 2005, Google Patents.
112. Grausova, L., A. Kromka, Z. Burdikova, A. Eckhardt, B. Rezek, J. Vacik, K. Haenen, V. Lisa and L. Bacakova, *Enhanced Growth and Osteogenic Differentiation of Human Osteoblast-Like Cells on Boron-Doped Nanocrystalline Diamond Thin Films*. PLoS ONE, 2011. **6**(6): p. e20943.
113. Marcon, L., C. Spriet, Y. Coffinier, E. Galopin, C. Rosnoblet, S. Szunerits, L. Hélot, P.-O. Angrand and R. Boukherroub, *Cell Adhesion Properties on Chemically Micropatterned Boron-Doped Diamond Surfaces*. Langmuir, 2010. **26**(19): p. 15065-15069.
114. Givargizov, E.I., V.V. Zhiraov, A.V. Kuznetsov and P.S. Plekhanov, *Growth of Diamond Particles on Sharpened Silicon Tips*. Materials Letters, 1993. **18**(1-2): p. 61-63.
115. Taniguchi, J., H. Ohno, Y. Kawabata and I. Miyamoto, *Ion-beam Processing of Single Crystal Diamond Using SOG Mask*. Vacuum, 2006. **80**(7): p. 793-797.
116. Enlund, J., J. Isberg, M. Karlsson, F. Nikolajeff, J. Olsson and D.J. Twitchen, *Anisotropic Dry Etching of Boron Doped Single Crystal CVD Diamond*. Carbon, 2005. **43**(9): p. 1839-1842.
117. Yamada, T., H. Yoshikawa, H. Uetsuka, S. Kumaragurubaran, N. Tokuda and S.-i. Shikata, *Cycle of Two-step Etching Process Using ICP for Diamond MEMS Applications*. Diamond and Related Materials, 2007. **16**(4-7): p. 996-999.
118. Baik, E.-S., Y.-J. Baik and D. Jeon, *Diamond Tip Fabrication by Air-plasma Etching of Diamond with an Oxide Mask*. Diamond and Related Materials, 1999. **8**(12): p. 2169-2171.
119. Uetsuka, H., T. Yamada and S. Shikata, *ICP Etching of Polycrystalline Diamonds: Fabrication of Diamond Nano-tips for AFM Cantilevers*. Diamond and Related Materials, 2008. **17**(4-5): p. 728-731.

120. Hwang, D.S., T. Saito and N. Fujimori, *New Etching Process for Device Fabrication Using Diamond*. Diamond and Related Materials, 2004. **13**(11–12): p. 2207-2210.
121. Shuji, K., Y. Yukie and M. Katsumi, *Plasma Etching of CVD Diamond Films Using an ECR-type Oxygen Source*. Nanotechnology, 1999. **10**(4): p. 385.
122. Zhang, W.J., Y. Wu, C.Y. Chan, W.K. Wong, X.M. Meng, I. Bello, Y. Lifshitz and S.T. Lee, *Structuring Single- and Nano-crystalline Diamond Cones*. Diamond and Related Materials, 2004. **13**(4–8): p. 1037-1043.
123. Izak, T., A. Kromka, O. Babchenko, M. Ledinsky, K. Hruska and E. Verveniots, *Comparative Study on Dry Etching of Polycrystalline Diamond Thin Films*. Vacuum, 2012. **86**(6): p. 799-802.
124. Zou, Y.S., Y. Yang, W.J. Zhang, Y.M. Chong, B. He, I. Bello and S.T. Lee, *Fabrication of Diamond Nanopillars and Their Arrays*. Applied Physics Letters, 2008. **92**(5): p. 053105.
125. Davydova, M., A. Kromka, B. Rezek, O. Babchenko, M. Stuchlik and K. Hruska, *Fabrication of Diamond Nanorods for Gas Sensing Applications*. Applied Surface Science, 2010. **256**(18): p. 5602-5605.
126. Tran, D.T., C. Fansler, T.A. Grotjohn, D.K. Reinhard and J. Asmussen, *Investigation of Mask Selectivities and Diamond Etching Using Microwave Plasma-assisted Etching*. Diamond and Related Materials, 2010. **19**(7–9): p. 778-782.
127. Freedman, A. and C.D. Stinespring, *Fluorination of Diamond (100) by Atomic and Molecular Beams*. Applied Physics Letters, 1990. **57**(12): p. 1194-1196.
128. Miller, J.B. and D.W. Brown, *Photochemical Modification of Diamond Surfaces*. Langmuir, 1996. **12**(24): p. 5809-5817.
129. Freedman, A., *Halogenation of Diamond (100) and (111) Surfaces by Atomic Beams*. Journal of Applied Physics, 1994. **75**(6): p. 3112-3120.
130. Martin, H.B., A. Argoitia, J.C. Angus and U. Landau, *Voltammetry Studies of Single-Crystal and Polycrystalline Diamond Electrodes*. Journal of The Electrochemical Society, 1999. **146**(8): p. 2959-2964.
131. Salazar-Banda, G.R., L.S. Andrade, P.A.P. Nascente, P.S. Pizani, R.C. Rocha-Filho and L.A. Avaca, *On the Changing Electrochemical Behaviour of Boron-doped Diamond Surfaces with Time after Cathodic Pre-treatments*. Electrochimica Acta, 2006. **51**(22): p. 4612-4619.

132. Ivandini, T.A., T.N. Rao, A. Fujishima and Y. Einaga, *Electrochemical Oxidation of Oxalic Acid at Highly Boron-Doped Diamond Electrodes*. Analytical Chemistry, 2006. **78**(10): p. 3467-3471.
133. Spătaru, N., B.V. Sarada, E. Popa, D.A. Tryk and A. Fujishima, *Voltammetric Determination of l-Cysteine at Conductive Diamond Electrodes*. Analytical Chemistry, 2001. **73**(3): p. 514-519.
134. Swain, G.M., *The Susceptibility to Surface Corrosion in Acidic Fluoride Media: A Comparison of Diamond, HOPG, and Glassy Carbon Electrodes*. Journal of The Electrochemical Society, 1994. **141**(12): p. 3382-3393.
135. Holt, K.B., C. Forryan, R.G. Compton, J.S. Foord and F. Marken, *Anodic Activity of Boron-doped Diamond Electrodes in Bleaching Processes: Effects of Ultrasound and Surface States*. New Journal of Chemistry, 2003. **27**(4): p. 698-703.
136. Bennett, J.A., J. Wang, Y. Show and G.M. Swain, *Effect of sp²-Bonded Nondiamond Carbon Impurity on the Response of Boron-Doped Polycrystalline Diamond Thin-Film Electrodes*. Journal of The Electrochemical Society, 2004. **151**(9): p. E306-E313.
137. Mahé, E., D. Devilliers and C. Comninellis, *Electrochemical Reactivity at Graphitic Micro-domains on Polycrystalline Boron Doped Diamond Thin-films Electrodes*. Electrochimica Acta, 2005. **50**(11): p. 2263-2277.
138. Notsu, H., I. Yagi, T. Tatsuma, D.A. Tryk and A. Fujishima, *Surface Carbonyl Groups on Oxidized Diamond Electrodes*. Journal of Electroanalytical Chemistry, 2000. **492**(1): p. 31-37.
139. Tryk, D.A., H. Tachibana, H. Inoue and A. Fujishima, *Boron-doped Diamond Electrodes: The Role of Surface Termination in the Oxidation of Dopamine and Ascorbic Acid*. Diamond and Related Materials, 2007. **16**(4-7): p. 881-887.
140. Masuda, H., M. Watanabe, K. Yasui, D. Tryk, T. Rao and A. Fujishima, *Fabrication of a Nanostructured Diamond Honeycomb Film*. Advanced Materials, 2000. **12**(6): p. 444-447.
141. Siné, G., L. Ouattara, M. Panizza and C. Comninellis, *Electrochemical Behavior of Fluorinated Boron-Doped Diamond*. Electrochemical and Solid-State Letters, 2003. **6**(9): p. D9-D11.
142. Ferro, S. and A. De Battisti, *The 5-V Window of Polarizability of Fluorinated Diamond Electrodes in Aqueous Solutions*. Analytical Chemistry, 2003. **75**(24): p. 7040-7042.

143. Fromell, K., P. Forsberg, M. Karlsson, K. Larsson, F. Nikolajeff and L. Baltzer, *Designed Protein Binders in Combination with Nanocrystalline Diamond for Use in High-sensitivity Biosensors*. Analytical and Bioanalytical Chemistry, 2012. **404**(6-7): p. 1643-1651.
144. Hadenfeldt, S. and C. Benndorf, *Adsorption of Fluorine and Chlorine on the Diamond (100) Surface*. Surface Science, 1998. **402-404**(0): p. 227-231.
145. Ando, T., M. Nishitani-Gamo, R.E. Rawles, K. Yamamoto, M. Kamo and Y. Sato, *Chemical Modification of Diamond Surfaces Using a Chlorinated Surface as an Intermediate State*. Diamond and Related Materials, 1996. **5**(10): p. 1136-1142.
146. Takahashi, K., M. Tanga, O. Takai and H. Okamura, *DNA bonding to diamond*. Bio Ind, 2000. **17**: p. 44-51.
147. Takahashi, K., M. Tanga, O. Takai and H. Okamura, *DNA Preservation Using Diamond Chips*. Diamond and Related Materials, 2003. **12**(3-7): p. 572-576.
148. Nichols, B.M., K.M. Metz, K.-Y. Tse, J.E. Butler, J.N. Russell and R.J. Hamers, *Electrical Bias Dependent Photochemical Functionalization of Diamond Surfaces*. The Journal of Physical Chemistry B, 2006. **110**(33): p. 16535-16543.
149. Shin, D., B. Rezek, N. Tokuda, D. Takeuchi, H. Watanabe, T. Nakamura, T. Yamamoto and C.E. Nebel, *Photo- and Electrochemical Bonding of DNA to Single Crystalline CVD Diamond*. Physica Status Solidi (A), 2006. **203**(13): p. 3245-3272.
150. Zhang, G.-J., K.-S. Song, Y. Nakamura, T. Ueno, T. Funatsu, I. Ohdomari and H. Kawarada, *DNA Micropatterning on Polycrystalline Diamond via One-Step Direct Amination*. Langmuir, 2006. **22**(8): p. 3728-3734.
151. Bouvier, P., D. Delabouglise, A. Denoyelle, B. Marcus, M. Mermoux and J.-P. Petit, *Photosensitization of Boron-Doped Diamond by Surface Grafting of Pyrene Groups*. Electrochemical and Solid-State Letters, 2005. **8**(9): p. E57-E61.
152. Kuo, T.C., R.L. McCreery and G.M. Swain, *Electrochemical Modification of Boron-Doped Chemical Vapor Deposited Diamond Surfaces with Covalently Bonded Monolayers*. Electrochemical and Solid-state Letters, 1999. **2**(6): p. 288-290.
153. Kondo, T., K. Honda, D.A. Tryk and A. Fujishima, *Covalent Modification of Single-Crystal Diamond Electrode Surfaces*. Journal of The Electrochemical Society, 2005. **152**(1): p. E18-E23.
154. Shin, D., N. Tokuda, B. Rezek and C.E. Nebel, *Periodically Arranged Benzene-linker Molecules on Boron-doped Single-crystalline Diamond Films for DNA Sensing*. Electrochemistry Communications, 2006. **8**(5): p. 844-850.

155. Uetsuka, H., D. Shin, N. Tokuda, K. Saeki and C.E. Nebel, *Electrochemical Grafting of Boron-Doped Single-Crystalline Chemical Vapor Deposition Diamond with Nitrophenyl Molecules*. Langmuir, 2007. **23**(6): p. 3466-3472.
156. Lud, S.Q., M. Steenackers, R. Jordan, P. Bruno, D.M. Gruen, P. Feulner, J.A. Garrido and M. Stutzmann, *Chemical Grafting of Biphenyl Self-Assembled Monolayers on Ultrananocrystalline Diamond*. Journal of the American Chemical Society, 2006. **128**(51): p. 16884-16891.
157. Yang, W., S.E. Baker, J.E. Butler, C.-s. Lee, J.N. Russell, L. Shang, B. Sun and R.J. Hamers, *Electrically Addressable Biomolecular Functionalization of Conductive Nanocrystalline Diamond Thin Films*. Chemistry of Materials, 2005. **17**(5): p. 938-940.
158. Sochr, J., L. Švorc, M. Rievaj and D. Bustin, *Electrochemical Determination of Adrenaline in Human Urine Using a Boron-doped Diamond Film Electrode*. Diamond and Related Materials, 2014. **43**(0): p. 5-11.
159. Fujishima, A., T.N. Rao, E. Popa, B.V. Sarada, I. Yagi and D.A. Tryk, *Electroanalysis of Dopamine and NADH at Conductive Diamond Electrodes*. Journal of Electroanalytical Chemistry, 1999. **473**(1-2): p. 179-185.
160. Rao, T.N., I. Yagi, T. Miwa, D.A. Tryk and A. Fujishima, *Electrochemical Oxidation of NADH at Highly Boron-Doped Diamond Electrodes*. Analytical Chemistry, 1999. **71**(13): p. 2506-2511.
161. Sarada, B.V., T.N. Rao, D.A. Tryk and A. Fujishima, *Electrochemical Oxidation of Histamine and Serotonin at Highly Boron-Doped Diamond Electrodes*. Analytical Chemistry, 2000. **72**(7): p. 1632-1638.
162. Lee, J. and S.-M. Park, *Direct Electrochemical Assay of Glucose Using Boron-doped Diamond Electrodes*. Analytica Chimica Acta, 2005. **545**(1): p. 27-32.
163. Zhao, J., D. Wu and J. Zhi, *A Direct Electrochemical Method for Diabetes Diagnosis based on as-prepared Boron-doped Nanocrystalline Diamond Thin Film Electrodes*. Journal of Electroanalytical Chemistry, 2009. **626**(1-2): p. 98-102.
164. Zhao, J., L. Wu and J. Zhi, *Non-enzymatic Glucose Detection Using as-prepared Boron-doped Diamond Thin-film Electrodes*. Analyst, 2009. **134**(4): p. 794-799.
165. Chiku, M., K. Horisawa, N. Doi, H. Yanagawa and Y. Einaga, *Electrochemical Detection of Tyrosine Derivatives and Protein Tyrosine Kinase Activity Using Boron-doped Diamond Electrodes*. Biosensors and Bioelectronics, 2010. **26**(1): p. 235-240.

166. Nekrassova, O., N.S. Lawrence and R.G. Compton, *Direct Oxidation of Haemoglobin at Bare Boron-doped Diamond Electrodes*. *Analyst*, 2004. **129**(9): p. 804-805.
167. Zhang, M., K. Gong, H. Zhang and L. Mao, *Layer-by-layer Assembled Carbon Nanotubes for Selective Determination of Dopamine in the Presence of Ascorbic Acid*. *Biosensors and Bioelectronics*, 2005. **20**(7): p. 1270-1276.
168. Zhang, L. and X. Jiang, *Attachment of Gold Nanoparticles to Glassy Carbon Electrode and its Application for the Voltammetric Resolution of Ascorbic Acid and Dopamine*. *Journal of Electroanalytical Chemistry*, 2005. **583**(2): p. 292-299.
169. Lin, X., Y. Zhang, W. Chen and P. Wu, *Electrocatalytic Oxidation and Determination of Dopamine in the Presence of Ascorbic Acid and Uric Acid at a Poly (p-nitrobenzenazo resorcinol) Modified Glassy Carbon Electrode*. *Sensors and Actuators B: Chemical*, 2007. **122**(1): p. 309-314.
170. Hayasaka, T., S. Yoshida, K.Y. Inoue, M. Nakano, T. Ishikawa, T. Matsue, M. Esashi and S. Tanaka. *Integration of diamond microelectrodes on CMOS-based amperometric biosensor array by film transfer technology*. in *Micro Electro Mechanical Systems (MEMS), 2014 IEEE 27th International Conference on*. 2014.
171. Popa, E., Y. Kubota, D.A. Tryk and A. Fujishima, *Selective Voltammetric and Amperometric Detection of Uric Acid with Oxidized Diamond Film Electrodes*. *Analytical Chemistry*, 2000. **72**(7): p. 1724-1727.
172. Terashima, C., T.N. Rao, B.V. Sarada and A. Fujishima, *Amperometric Detection of Oxidized and Reduced Glutathione at Anodically Pretreated Diamond Electrodes*. *Chemistry Letters*, 2003. **32**(2): p. 136-137.
173. Kuga, S., J.-H. Yang, H. Takahashi, K. Hirama, T. Iwasaki and H. Kawarada, *Detection of Mismatched DNA on Partially Negatively Charged Diamond Surfaces by Optical and Potentiometric Methods*. *Journal of the American Chemical Society*, 2008. **130**(40): p. 13251-13263.
174. Vermeeren, V., N. Bijnens, S. Wenmackers, M. Daenen, K. Haenen, O.A. Williams, M. Ameloot, M. vandeVen, P. Wagner and L. Michiels, *Towards a Real-Time, Label-Free, Diamond-Based DNA Sensor*. *Langmuir*, 2007. **23**(26): p. 13193-13202.
175. Oliveira, S.C.B. and A.M. Oliveira-Brett, *In Situ DNA Oxidative Damage by Electrochemically Generated Hydroxyl Free Radicals on a Boron-Doped Diamond Electrode*. *Langmuir*, 2012. **28**(10): p. 4896-4901.
176. Vermeeren, V., S. Wenmackers, P. Wagner and L. Michiels, *DNA Sensors with Diamond as a Promising Alternative Transducer Material*. *Sensors*, 2009. **9**(7): p. 5600-5636.

177. Liu, B., J. Hu and J.S. Foord, *Electrochemical Detection of DNA Hybridization by a Zirconia Modified Diamond Electrode*. *Electrochemistry Communications*, 2012. **19**(0): p. 46-49.
178. Mangombo, Z., D. Key, E. Iwuoha and P. Baker, *Development of L-phenylalanine biosensor and its application to real sample analysis*. 2013.
179. Wu, W., Z. Gu, X. Liu, L. Bai and Z. Tang, *Nanograss Array Boron-Doped Diamond Electrode for Toxicity Sensor with Shewanella loihica PV-4 in Bioelectrochemical Systems*. *Sensor Letters*, 2014. **12**(1): p. 191-196.
180. Wei, M., G. Zeng and Q. Lu, *Determination of Organophosphate Pesticides Using an Acetylcholinesterase-based Biosensor Based on a Boron-doped Diamond Electrode Modified with Gold Nanoparticles and Carbon Spheres*. *Microchimica Acta*, 2014. **181**(1-2): p. 121-127.
181. Vitoreti, A.B.F., O. Abrahão, R.A. da Silva Gomes, G.R. Salazar-Banda and R.T. Oliveira, *Electroanalytical Determination of Captopril in Pharmaceutical Formulations Using Boron-Doped Diamond Electrodes*. *Int. J. Electrochem. Sci*, 2014. **9**: p. 1044-1054.
182. Shalini, J., K.J. Sankaran, C.-Y. Lee, N.-H. Tai and I.-N. Lin, *An amperometric urea biosensor based on covalent immobilization of urease on N 2 incorporated diamond nanowire electrode*. *Biosensors and Bioelectronics*, 2014. **56**: p. 64-70.
183. Villalba, P., M.K. Ram, H. Gomez, A. Kumar, V. Bhethanabotla and A. Kumar, *GOX-functionalized Nanodiamond Films for Electrochemical Biosensor*. *Materials Science and Engineering: C*, 2011. **31**(5): p. 1115-1120.
184. Villalba, P., M.K. Ram, H. Gomez, A. Kumar, V. Bhethanabotla and A. Kumar, *Glucose Oxidase-Functionalized Nanodiamond Films for Biosensor Application*. *MRS Online Proceedings Library*, 2011. **1282**: p. null-null.
185. Bai, Y.-F., T.-B. Xu, J.H.T. Luong and H.-F. Cui, *Direct Electron Transfer of Glucose Oxidase-Boron Doped Diamond Interface: A New Solution for a Classical Problem*. *Analytical Chemistry*, 2014. **86**(10): p. 4910-4918.
186. Tran, D.T., V. Vermeeren, L. Grieten, S. Wenmackers, P. Wagner, J. Pollet, K.P.F. Janssen, L. Michiels and J. Lammertyn, *Nanocrystalline Diamond Impedimetric Aptasensor for the Label-free Detection of Human IgE*. *Biosensors and Bioelectronics*, 2011. **26**(6): p. 2987-2993.
187. Raina, S., W. Kang, J. Davidson and J.-H. Huang, *Electrochemical Biosensor Utilizing Nitrogen Incorporated Nanodiamond Ultra-Microelectrode Array*. *ECS Transactions*, 2010. **28**(34): p. 21-28.

188. Rismetov, B., T.A. Ivandini, E. Saepudin and Y. Einaga, *Electrochemical Detection of Hydrogen Peroxide at Platinum-modified Diamond Electrodes for an Application in Melamine Strip Tests*. *Diamond and Related Materials*, 2014. **48**: p. 88-95.
189. Dai, W., M. Li, H. Li and B. Yang, *Amperometric Biosensor Based on Nanoporous Nickel/Boron-doped Diamond Film for Electroanalysis of L-alanine*. *Sensors and Actuators B: Chemical*, 2014. **201**(0): p. 31-36.
190. Sim, H., J.-H. Kim, S.-K. Lee, M.-J. Song, D.-H. Yoon, D.-S. Lim and S.-I. Hong, *High-sensitivity Non-enzymatic Glucose Biosensor Based on Cu(OH)₂ Nanoflower Electrode Covered with Boron-doped Nanocrystalline Diamond Layer*. *Thin Solid Films*, 2012. **520**(24): p. 7219-7223.
191. Janegitz, B.C., R.A. Medeiros, R.C. Rocha-Filho and O. Fatibello-Filho, *Direct Electrochemistry of Tyrosinase and Biosensing for Phenol Based on Gold Nanoparticles Electrodeposited on a Boron-doped Diamond Electrode*. *Diamond and Related Materials*, 2012. **25**(0): p. 128-133.
192. Song, M.-J., J.-H. Kim, S.-K. Lee, D.-S. Lim, S.W. Hwang and D. Whang, *Analytical Characteristics of Electrochemical Biosensor Using Pt-Dispersed Graphene on Boron Doped Diamond Electrode*. *Electroanalysis*, 2011. **23**(10): p. 2408-2414.
193. Song, M.-J., J.-H. Kim, S.-K. Lee and D.-S. Lim, *Fabrication of Pt Nanoparticles-decorated CVD Diamond Electrode for Biosensor Applications*. *Analytical Sciences*, 2011. **27**(10): p. 985-985.
194. Song, M.-J., J. Kim, S. Lee, J.-H. Lee, D. Lim, S. Hwang and D. Whang, *Pt-polyaniline Nanocomposite on Boron-doped Diamond Electrode for Amperometric Biosensor with Low Detection Limit*. *Microchimica Acta*, 2010. **171**(3-4): p. 249-255.
195. Skoog, S.A., P.R. Miller, R.D. Boehm, A.V. Sumant, R. Polsky and R.J. Narayan, *Nitrogen-incorporated Ultrananocrystalline Diamond Microneedle Arrays for Electrochemical Biosensing*. *Diamond and Related Materials*, 2015. **54**(0): p. 39-46.
196. Picollo, F., *Amperometric detection of quantal catecholamine secretion from individual cells by an ion beam microfabricated single crystalline diamond biosensor*. 2013.
197. Stefan-van Staden, R.-I., R.a.M. Nejem, J.F. van Staden and H.Y. Aboul-Enein, *Amperometric Biosensor Based on Diamond Paste for the Enantioanalysis of L-lysine*. *Biosensors and Bioelectronics*, 2012. **35**(1): p. 439-442.

198. Varney, M.W., D.M. Aslam, A. Janoudi, H.-Y. Chan and D.H. Wang, *Polycrystalline-diamond MEMS Biosensors Including Neural Microelectrode-arrays*. Biosensors, 2011. **1**(3): p. 118-133.
199. Lisdat, F. and D. Schäfer, *The Use of Electrochemical Impedance Spectroscopy for Biosensing*. Analytical and Bioanalytical Chemistry, 2008. **391**(5): p. 1555-1567.
200. Hamers, R.J., J.E. Butler, T. Lasseter, B.M. Nichols, J.N. Russell Jr, K.-Y. Tse and W. Yang, *Molecular and biomolecular monolayers on diamond as an interface to biology*. Diamond and Related Materials, 2005. **14**(3-7): p. 661-668.
201. Yang, W., J.E. Butler, J.N. Russell and R.J. Hamers, *Interfacial Electrical Properties of DNA-Modified Diamond Thin Films: Intrinsic Response and Hybridization-Induced Field Effects*. Langmuir, 2004. **20**(16): p. 6778-6787.
202. Zhu, J.-T., C.-G. Shi, J.-J. Xu and H.-Y. Chen, *Direct Electrochemistry and Electrocatalysis of Hemoglobin on Undoped Nanocrystalline Diamond Modified Glassy Carbon Electrode*. Bioelectrochemistry, 2007. **71**(2): p. 243-248.
203. Weng, J., Z. Zhang, L. Sun and J.A. Wang, *High Sensitive Detection of Cancer Cell with a Folic Acid-based Boron-doped Diamond Electrode Using an AC Impedimetric Approach*. Biosensors and Bioelectronics, 2011. **26**(5): p. 1847-1852.
204. Vermeeren, V., L. Grieten, N. Vanden Bon, N. Bijmens, S. Wenmackers, S.D. Janssens, K. Haenen, P. Wagner and L. Michiels, *Impedimetric, Diamond-based Immunosensor For the Detection of C-reactive Protein*. Sensors and Actuators B: Chemical, 2011. **157**(1): p. 130-138.
205. Fritz, J., M.K. Baller, H.P. Lang, H. Rothuizen, P. Vettiger, E. Meyer, H. -J. Güntherodt, C. Gerber and J.K. Gimzewski, *Translating Biomolecular Recognition into Nanomechanics*. Science, 2000. **288**(5464): p. 316-318.
206. Yang, S.M., C. Chang, T.I. Yin and P.L. Kuo, *DNA Hybridization Measurement by Self-sensing Piezoresistive Microcantilevers in CMOS Biosensor*. Sensors and Actuators B: Chemical, 2008. **130**(2): p. 674-681.
207. Raiteri, R., M. Grattarola, H.-J. Butt and P. Skládal, *Micromechanical Cantilever-based Biosensors*. Sensors and Actuators B: Chemical, 2001. **79**(2-3): p. 115-126.
208. Ilic, B., D. Czaplewski, M. Zalalutdinov, H.G. Craighead, P. Neuzil, C. Campagnolo and C. Batt, *Single Cell Detection with Micromechanical Oscillators*. Journal of Vacuum Science & Technology B, 2001. **19**(6): p. 2825-2828.
209. Jing, L., C. Zongliang, D.M. Aslam, N. Sepulveda and J.P. Sullivan. *Diamond micro and nano resonators using laser, capacitive or piezoresistive detection*. in

Nano/Micro Engineered and Molecular Systems, 2008. NEMS 2008. 3rd IEEE International Conference on. 2008.

210. Bongrain, A., E. Scorsone, L. Rousseau, G. Lissorgues and P. Bergonzo, *Realisation and Characterisation of Mass-based Diamond Micro-transducers Working in Dynamic Mode*. Sensors and Actuators B: Chemical, 2011. **154**(2): p. 142-149.
211. Kupfer, B.Z., R.K. Ahmad, A. Zainal and R.B. Jackman, *Fabrication and Characterisation of Triangle-faced Single Crystal Diamond Micro-cantilevers*. Diamond and Related Materials, 2010. **19**(7-9): p. 742-747.
212. Manai, R., E. Scorsone, L. Rousseau, F. Ghassemi, M. Possas Abreu, G. Lissorgues, N. Tremillon, H. Ginisty, J.C. Arnault, E. Tuccori, M. Bernabei, K. Cali, K.C. Persaud and P. Bergonzo, *Grafting Odorant Binding Proteins on Diamond Bio-MEMS*. Biosensors and Bioelectronics, 2014. **60**(0): p. 311-317.
213. Bongrain, A., H. Uetsuka, L. Rousseau, L. Valbin, S. Saada, C. Gesset, E. Scorsone, G. Lissorgues and P. Bergonzo, *Measurement of DNA Denaturation on B-NCD Coated Diamond Micro-cantilevers*. physica status solidi (a), 2010. **207**(9): p. 2078-2083.
214. Guo, X., L. Huang, S. O'Brien, P. Kim and C. Nuckolls, *Directing and Sensing Changes in Molecular Conformation on Individual Carbon Nanotube Field Effect Transistors*. Journal of the American Chemical Society, 2005. **127**(43): p. 15045-15047.
215. Maehashi, K., T. Katsura, K. Kerman, Y. Takamura, K. Matsumoto and E. Tamiya, *Label-Free Protein Biosensor Based on Aptamer-Modified Carbon Nanotube Field-Effect Transistors*. Analytical Chemistry, 2007. **79**(2): p. 782-787.
216. Kwang-Soup, S., D. Munenori, N. Yusuke, K. Hirofumi, U. Hitoshi and K. Hiroshi, *Surface-modified Diamond Field-effect Transistors for Enzyme-immobilized Biosensors*. Japanese Journal of Applied Physics, 2004. **43**(6B): p. L814.
217. Abouzar, M.H., A. Poghosian, A. Razavi, A. Besmehn, N. Bijnens, O.A. Williams, K. Haenen, P. Wagner and M.J. Schöning, *Penicillin Detection with Nanocrystalline-diamond Field-effect Sensor*. Physica Status Solidi (A), 2008. **205**(9): p. 2141-2145.
218. Abouzar, M.H., A. Poghosian, A. Razavi, O.A. Williams, N. Bijnens, P. Wagner and M.J. Schöning, *Characterisation of Capacitive Field-effect Sensors with a Nanocrystalline-diamond Film as Transducer Material for Multi-parameter Sensing*. Biosensors and Bioelectronics, 2009. **24**(5): p. 1298-1304.

219. Poghosian, A., M.H. Abouzar, A. Razavi, M. Bäcker, N. Bijmens, O.A. Williams, K. Haenen, W. Moritz, P. Wagner and M.J. Schöning, *Nanocrystalline-diamond Thin Films with High pH and Penicillin Sensitivity Prepared on a Capacitive Si-SiO₂ Structure*. *Electrochimica Acta*, 2009. **54**(25): p. 5981-5985.
220. Song, K.-S., G.-J. Zhang, Y. Nakamura, K. Furukawa, T. Hiraki, J.-H. Yang, T. Funatsu, I. Ohdomari and H. Kawarada, *Label-free DNA Sensors Using Ultrasensitive Diamond Field-effect Transistors in Solution*. *Physical Review E*, 2006. **74**(4): p. 041919-1-7.
221. Kawarada, H. and A.R. Ruslinda, *Diamond Electrolyte Solution Gate FETs for DNA and Protein Sensors Using DNA/RNA Aptamers*. *Physica Status Solidi (A)*, 2011. **208**(9): p. 2005-2016.
222. Rahim Ruslinda, A., K. Tanabe, S. Ibori, X. Wang and H. Kawarada, *Effects of Diamond-FET-based RNA Aptamer Sensing for Detection of Real Sample of HIV-1 Tat Protein*. *Biosensors and Bioelectronics*, 2013. **40**(1): p. 277-282.
223. Jiali, W., Z. Jianzhong, Z. Guoxiong, L. Xinru and C. Nianyi, *Fabrication and Application of a Diamond-film Glucose Biosensor Based on a H₂O₂ Microarray Electrode*. *Analytica Chimica Acta*, 1996. **327**(2): p. 133-137.
224. Xu, Z., A. Kumar and A. Kumar, *Amperometric Detection of Glucose Using a Modified Nitrogen-Doped Nanocrystalline Diamond Electrode*. *Journal of Biomedical Nanotechnology*, 2005. **1**(4): p. 416-420.
225. Zhao, W., J.-J. Xu, Q.-Q. Qiu and H.-Y. Chen, *Nanocrystalline Diamond Modified Gold Electrode for Glucose Biosensing*. *Biosensors and Bioelectronics*, 2006. **22**(5): p. 649-655.
226. Luo, D., L. Wu and J. Zhi, *Fabrication of Boron-Doped Diamond Nanorod Forest Electrodes and Their Application in Nonenzymatic Amperometric Glucose Biosensing*. *ACS Nano*, 2009. **3**(8): p. 2121-2128.
227. Wang, J. and J.A. Carlisle, *Covalent Immobilization of Glucose Oxidase on Conducting Ultrananocrystalline Diamond Thin Films*. *Diamond and Related Materials*, 2006. **15**(2-3): p. 279-284.
228. Murakamia, R.-i. and Y. Cheol-Mun. *Development of Biosensor by Direct Covalent Immobilization of Glucose Oxidase on Boron Doped Diamond Film*. in *2012 1st International Symposium on Physics and Technology of Sensors (ISPTS)*. 2012.
229. Popa, E., H. Notsu, T. Miwa, D. Tryk and A. Fujishima, *Selective Electrochemical Detection of Dopamine in the Presence of Ascorbic Acid at Anodized Diamond Thin Film Electrodes*. *Electrochemical and solid-state letters*, 1999. **2**(1): p. 49-51.

230. Suzuki, A., T.A. Ivandini, K. Yoshimi, A. Fujishima, G. Oyama, T. Nakazato, N. Hattori, S. Kitazawa and Y. Einaga, *Fabrication, Characterization, and Application of Boron-Doped Diamond Microelectrodes for in Vivo Dopamine Detection*. Analytical Chemistry, 2007. **79**(22): p. 8608-8615.
231. Tatsuma, T., H. Mori and A. Fujishima, *Electron Transfer from Diamond Electrodes to Heme Peptide and Peroxidase*. Analytical Chemistry, 2000. **72**(13): p. 2919-2924.
232. Fujishima, A. and T.N. Rao, *New Directions in Structuring and Electrochemical Applications of Boron-doped Diamond Thin Films*. Diamond and Related Materials, 2001. **10**(9–10): p. 1799-1803.
233. Notsu, H., T. Tatsuma and A. Fujishima, *Tyrosinase-modified Boron-doped Diamond Electrodes for the Determination of Phenol Derivatives*. Journal of Electroanalytical Chemistry, 2002. **523**(1–2): p. 86-92.
234. Zhou, Y.L., R.H. Tian and J.F. Zhi, *Amperometric Biosensor Based on Tyrosinase Immobilized on a Boron-doped Diamond Electrode*. Biosensors and Bioelectronics, 2007. **22**(6): p. 822-828.
235. Zhao, J., D. Wu and J. Zhi, *A Novel Tyrosinase Biosensor Based on Biofunctional ZnO Nanorod Microarrays on the Nanocrystalline Diamond Electrode for Detection of Phenolic Compounds*. Bioelectrochemistry, 2009. **75**(1): p. 44-49.
236. Zhao, J., J. Zhi, Y. Zhou and W. Yan, *A Tyrosinase Biosensor Based on ZnO Nanorod Clusters/Nanocrystalline Diamond Electrodes for Biosensing of Phenolic Compounds*. Analytical Sciences, 2009. **25**(9): p. 1083-1088.
237. Song, K.-S., T. Sakai, H. Kanazawa, Y. Araki, H. Umezawa, M. Tachiki and H. Kawarada, *Cl⁻ sensitive Biosensor Used Electrolyte-solution-gate Diamond FETs*. Biosensors and Bioelectronics, 2003. **19**(2): p. 137-140.
238. Wang, J., G. Chen, M.P. Chatrathi, A. Fujishima, D.A. Tryk and D. Shin, *Microchip Capillary Electrophoresis Coupled with a Boron-Doped Diamond Electrode-Based Electrochemical Detector*. Analytical Chemistry, 2003. **75**(4): p. 935-939.
239. Huang, T.S., Y. Tzeng, Y.K. Liu, Y.C. Chen, K.R. Walker, R. Guntupalli and C. Liu, *Immobilization of Antibodies and Bacterial Binding on Nanodiamond and Carbon Nanotubes for Biosensor Applications*. Diamond and Related Materials, 2004. **13**(4–8): p. 1098-1102.
240. Li, M., G. Zhao, R. Geng and H. Hu, *Facile Electrocatalytic Redox of Hemoglobin by Flower-like Gold Nanoparticles on Boron-doped Diamond Surface*. Bioelectrochemistry, 2008. **74**(1): p. 217-221.

241. Wenmackers, S., V. Vermeeren, M. vandeVen, M. Ameloot, N. Bijmens, K. Haenen, L. Michiels and P. Wagner, *Diamond-based DNA Sensors: Surface Functionalization and Read-out Strategies*. Physica Status Solidi (A), 2009. **206**(3): p. 391-408.
242. Antigo Medeiros, R., A.E. de Carvalho, R.C. Rocha-Filho and O. Fatibello-Filho, *Square-Wave Voltammetry Determination of Aspartame in Dietary Products Using a Boron-Doped Diamond Electrode*. Analytical Letters, 2007. **40**(17): p. 3195-3207.
243. Härtl, A., B. Baur, M. Stutzmann and J.A. Garrido, *Enzyme-Modified Field Effect Transistors Based on Surface-Conductive Single-Crystalline Diamond*. Langmuir, 2008. **24**(17): p. 9898-9906.
244. Majid, E., K.B. Male and J.H.T. Luong, *Boron Doped Diamond Biosensor for Detection of Escherichia coli*. Journal of Agricultural and Food Chemistry, 2008. **56**(17): p. 7691-7695.
245. Preechaworapun, A., T.A. Ivandini, A. Suzuki, A. Fujishima, O. Chailapakul and Y. Einaga, *Development of Amperometric Immunosensor Using Boron-Doped Diamond with Poly(o-aminobenzoic acid)*. Analytical Chemistry, 2008. **80**(6): p. 2077-2083.
246. Zhou, Y., J. Zhi, Y. Zou, W. Zhang and S.-T. Lee, *Direct Electrochemistry and Electrocatalytic Activity of Cytochrome c Covalently Immobilized on a Boron-Doped Nanocrystalline Diamond Electrode*. Analytical Chemistry, 2008. **80**(11): p. 4141-4146.
247. Wang, Q., A. Kromka, J. Houdkova, O. Babchenko, B. Rezek, M. Li, R. Boukherroub and S. Szunerits, *Nanomolar Hydrogen Peroxide Detection Using Horseradish Peroxidase Covalently Linked to Undoped Nanocrystalline Diamond Surfaces*. Langmuir, 2012. **28**(1): p. 587-592.
248. Quershi, A., Y. Gurbuz, W.P. Kang and J.L. Davidson, *A Novel Interdigitated Capacitor Based Biosensor for Detection of Cardiovascular Risk Marker*. Biosensors and Bioelectronics, 2009. **25**(4): p. 877-882.
249. Mangombo, Z., P. Baker, E. Iwuoha and D. Key, *Tyrosinase Biosensor Based on a Boron-doped Diamond Electrode Modified with a Polyaniline-poly(vinyl sulfonate) Composite Film*. Microchimica Acta, 2010. **170**(3-4): p. 267-273.
250. Rahim Ruslinda, A., X. Wang, Y. Ishii, Y. Ishiyama, K. Tanabe and H. Kawarada, *Human Immunodeficiency Virus Trans-activator of Transcription Peptide Detection via Ribonucleic Acid Aptamer on Aminated Diamond Biosensor*. Applied Physics Letters, 2011. **99**(12): p. 123702-1-3.

251. Andreescu, D., S. Andreescu and O.A. Sadik, *New Materials for Biosensors, Biochips and Molecular Bioelectronics*, in *Biosensors and Modern Biospecific Analytical Techniques*, L. Gorton, Editor. 2005, Elsevier: Amsterdam.
252. Basuray, S., S. Senapati, A. Aijian, A.R. Mahon and H.-C. Chang, *Shear and AC Field Enhanced Carbon Nanotube Impedance Assay for Rapid, Sensitive, and Mismatch-Discriminating DNA Hybridization*. ACS Nano, 2009. 3(7): p. 1823-1830.
253. Chen, Y., Y.D. Lee, H. Vedala, B.L. Allen and A. Star, *Exploring the Chemical Sensitivity of a Carbon Nanotube/Green Tea Composite*. ACS Nano, 2010. 4(11): p. 6854-6862.
254. Song, H.S., O.S. Kwon, S.H. Lee, S.J. Park, U.-K. Kim, J. Jang and T.H. Park, *Human Taste Receptor-Functionalized Field Effect Transistor as a Human-Like Nanobioelectronic Tongue*. Nano Letters, 2012. 13(1): p. 172-178.
255. Wang, M., L. Wang, G. Wang, X. Ji, Y. Bai, T. Li, S. Gong and J. Li, *Application of Impedance Spectroscopy for Monitoring Colloid Au-Enhanced Antibody Immobilization and Antibody-Antigen Reactions*. Biosensors and Bioelectronics, 2004. 19(6): p. 575-582.
256. Li, C.-Z., Y. Liu and J.H. Luong, *Impedance Sensing of DNA Binding Drugs Using Gold Substrates Modified with Gold Nanoparticles*. Analytical Chemistry, 2005. 77(2): p. 478-485.
257. Szymanska, I., H. Radecka, J. Radecki and R. Kaliszan, *Electrochemical Impedance Spectroscopy for Study of Amyloid B-Peptide Interactions with (-)-Nicotine Ditartrate and (-)-Cotinine*. Biosensors And Bioelectronics, 2007. 22(9): p. 1955-1960.
258. Choi, S.-H., G. Ankonina, D.-Y. Youn, S.-G. Oh, J.-M. Hong, A. Rothschild and I.-D. Kim, *Hollow ZnO Nanofibers Fabricated Using Electrospun Polymer Templates and Their Electronic Transport Properties*. ACS Nano, 2009. 3(9): p. 2623-2631.
259. Fowler, J.D., M.J. Allen, V.C. Tung, Y. Yang, R.B. Kaner and B.H. Weiller, *Practical Chemical Sensors from Chemically Derived Graphene*. ACS Nano, 2009. 3(2): p. 301-306.
260. Robinson, J.T., F.K. Perkins, E.S. Snow, Z. Wei and P.E. Sheehan, *Reduced Graphene Oxide Molecular Sensors*. Nano Letters, 2008. 8(10): p. 3137-3140.
261. Weetall, H.H., *Preparation of Immobilized Proteins Covalently Coupled Through Silane Coupling Agents to Inorganic Supports*. Applied Biochemistry and Biotechnology, 1993. 41(3): p. 157-188.

262. Seitz, O., P.G. Fernandes, R. Tian, N. Karnik, H.-C. Wen, H. Stiegler, R.A. Chapman, E.M. Vogel and Y.J. Chabal, *Control and Stability of Self-Assembled Monolayers under Biosensing Conditions*. Journal of Materials Chemistry, 2011. **21**(12): p. 4384-4392.
263. Yang, W., O. Auciello, J.E. Butler, W. Cai, J.A. Carlisle, J.E. Gerbi, D.M. Gruen, T. Knickerbocker, T.L. Lasseter and J.N. Russell, *DNA-Modified Nanocrystalline Diamond Thin-Films as Stable, Biologically Active Substrates*. Nature Materials, 2002. **1**(4): p. 253-257.
264. Granger, M.C., M. Witek, J. Xu, J. Wang, M. Hupert, A. Hanks, M.D. Koppang, J.E. Butler, G. Lucazeau and M. Mermoux, *Standard Electrochemical Behavior of High-Quality, Boron-Doped Polycrystalline Diamond Thin-Film Electrodes*. Analytical Chemistry, 2000. **72**(16): p. 3793-3804.
265. Swain, G.M. and R. Ramesham, *The Electrochemical Activity of Boron-Doped Polycrystalline Diamond Thin Film Electrodes*. Analytical Chemistry, 1993. **65**(4): p. 345-351.
266. Nebel, C.E., D. Shin, B. Rezek, N. Tokuda, H. Uetsuka and H. Watanabe, *Diamond and Biology*. Journal of the Royal Society Interface, 2007. **4**(14): p. 439-461.
267. Foord, J.S., *Diamond Electrochemical Sensors*, in *CVD Diamond for Electronic Devices and Sensors*. 2009, John Wiley & Sons, Ltd. p. 439-465.
268. Yang, W., J.E. Butler, J.N. Russell and R.J. Hamers, *Interfacial Electrical Properties of DNA-Modified Diamond Thin Films: Intrinsic Response and Hybridization-Induced Field Effects*. Langmuir, 2004. **20**(16): p. 6778-6787.
269. Yang, W. and R.J. Hamers, *Fabrication and Characterization of a Biologically Sensitive Field-Effect Transistor using a Nanocrystalline Diamond Thin Film*. Applied Physics Letters, 2004. **85**(16): p. 3626-3628.
270. Hartl, A., E. Schmich, J.A. Garrido, J. Hernando, S.C. Catharino, S. Walter, P. Feulner, A. Kromka, D. Steinmuller and M. Stutzmann, *Protein-Modified Nanocrystalline Diamond Thin Films for Biosensor Applications*. Nature Materials, 2004. **3**(10): p. 736-742.
271. Yang, N., H. Uetsuka, E. Osawa and C.E. Nebel, *Vertically Aligned Diamond Nanowires for DNA Sensing*. Angewandte Chemie International Edition, 2008. **47**(28): p. 5183-5185.
272. Narayan, J., W.D. Fan, R.J. Narayan, P. Tiwari and H.H. Stadelmaier, *Diamond, diamond-like and titanium nitride biocompatible coatings for human body parts*. Materials Science and Engineering: B, 1994. **25**(1): p. 5-10.

273. Tang, L., C. Tsai, W.W. Gerberich, L. Kruckeberg and D.R. Kania, *Biocompatibility of chemical-vapour-deposited diamond*. *Biomaterials*, 1995. **16**(6): p. 483-488.
274. Rupprecht, S., A. Bloch, S. Rosiwal, F.W. Neukam and J. Wiltfang, *Examination of the Bone-Metal Interface of Titanium Implants Coated by the Microwave Plasma Chemical Vapor Deposition Method*. *The International Journal Of Oral & Maxillofacial Implants*, 2002. **17**(6): p. 778-785.
275. Bacakova, L., *Nanodiamond As Promising Material for Bone Tissue Engineering*. *Nanoscience And Nanotechnology*, 2009. **9**: p. 3524-3534.
276. Grausova, L., A. Kromka, Z. Burdikova, A. Eckhardt, B. Rezek, J. Vacik, K. Haenen, V. Lisa and L. Bacakova, *Enhanced Growth and Osteogenic Differentiation of Human Osteoblast-Like Cells on Boron-Doped Nanocrystalline Diamond Thin Films*. *PLoS One*, 2011. **6**(6): p. 1-17.
277. Shi, B., Q. Jin, L. Chen and O. Auciello, *Fundamentals of Ultrananocrystalline Diamond (UNCD) Thin Films as Biomaterials for Developmental Biology: Embryonic Fibroblasts Growth on the Surface of (UNCD) Films*. *Diamond and Related Materials*, 2009. **18**(2-3): p. 596-600.
278. Garrido, J.A., *Biofunctionalization of Diamond Surfaces: Fundamentals and Applications*, in *CVD Diamond for Electronic Devices and Sensors*. 2009, John Wiley & Sons, Ltd. p. 399-437.
279. Stavis, C., T.L. Clare, J.E. Butler, A.D. Radadia, R. Carr, H. Zeng, W.P. King, J.A. Carlisle, A. Aksimentiev and R. Bashir, *Surface Functionalization of Thin-Film Diamond for Highly Stable and Selective Biological Interfaces*. *Proceedings of the National Academy of Sciences*, 2011. **108**(3): p. 983-988.
280. Colavita, P.E., B. Sun, K.-Y. Tse and R.J. Hamers, *Photochemical Grafting of N-Alkenes onto Carbon Surfaces: The Role of Photoelectron Ejection*. *Journal Of The American Chemical Society*, 2007. **129**(44): p. 13554-13565.
281. Strother, T., T. Knickerbocker, J.N. Russell, J.E. Butler, L.M. Smith and R.J. Hamers, *Photochemical Functionalization of Diamond Films*. *Langmuir*, 2002. **18**(4): p. 968-971.
282. Lu, M., T. Knickerbocker, W. Cai, W. Yang, R.J. Hamers and L.M. Smith, *Invasive Cleavage Reactions on DNA-Modified Diamond Surfaces*. *Biopolymers*, 2004. **73**(5): p. 606-613.
283. Ozawa, M., M. Inaguma, M. Takahashi, F. Kataoka, A. Krueger and E. Osawa, *Preparation and Behavior of Brownish, Clear Nanodiamond Colloids*. *Advanced Materials*, 2007. **19**(9): p. 1201-1206.

284. Mochalin, V.N., O. Shenderova, D. Ho and Y. Gogotsi, *The Properties and Applications of Nanodiamonds*. Nature Nanotechnology, 2011. 7(1): p. 11-23.
285. Butler, J.E. and A.V. Sumant, *The CVD of Nanodiamond Materials*. Chemical Vapor Deposition, 2008. 14(7): p. 145-160.
286. Orlando, A., *Science and Technology of Ultrananocrystalline Diamond Film-Based MEMS and NEMS Devices and Systems*, in *Ultrananocrystalline Diamond: Synthesis, Properties and Applications*, O.A. Shenderova and D.M. Gruen, Editors. 2012, Elsevier Science. p. 383-420.
287. Ralchenko, V., A. Saveliev, S. Voronina, A. Dementjev, K. Maslakov, M. Salerno, A. Podesta and P. Milani, *Nanodiamond Seeding for Nucleation and Growth of CVD Diamond Films*, in *Proceedings of the NATO Advanced Research Workshop on Synthesis, Properties and Applications of Ultrananocrystalline Diamond*, D.M. Gruen, O.A. Shenderova, and A.Y. Vul', Editors. 2005, Springer: St. Petersburg. p. 109-124.
288. Affoune, A., B. Prasad, H. Sato and T. Enoki, *Electrophoretic Deposition of Nanosized Diamond Particles*. Langmuir, 2001. 17(2): p. 547-551.
289. Shenderova, O., S. Hens and G. McGuire, *Seeding Slurries Based on Detonation Nanodiamond in DMSO*. Diamond and Related Materials, 2010. 19(2-3): p. 260-267.
290. Schmidlin, L., V. Pichot, S. Josset, R. Pawlak, T. Glatzel, S. Kawai, E. Meyer and D. Spitzer, *Two-Dimensional Nanodiamond Monolayers Deposited by Combined Ultracentrifugation and Electrophoresis Techniques*. Applied Physics Letters, 2012. 101(25): p. 253111-253114.
291. Kim, J.H., S.K. Lee, O.M. Kwon and D.S. Lim, *Ultra Thin CVD Diamond Film Deposition by Electrostatic Self-Assembly Seeding Process with Nano-Diamond Particles*. Journal of Nanoscience And Nanotechnology, 2009. 9(7): p. 4121-4127.
292. Girard, H.A., S. Perruchas, C. Gesset, M. Chaigneau, L. Vieille, J.C. Arnault, P. Bergonzo, J.P. Boilot and T. Gacoin, *Electrostatic Grafting of Diamond Nanoparticles: A Versatile Route to Nanocrystalline Diamond Thin Films*. ACS Applied Materials & Interfaces, 2009. 1(12): p. 2738-2746.
293. Chen, Y.-C., Y. Tzeng, A.-J. Cheng, R. Dean, M. Park and B.M. Wilamowski, *Inkjet Printing of Nanodiamond Suspensions in Ethylene Glycol for CVD Growth of Patterned Diamond Structures and Practical Applications*. Diamond And Related Materials, 2009. 18(2-3): p. 146-150.
294. Zhuang, H., B. Song, T. Staedler and X. Jiang, *Microcontact Printing of Monodiamond Nanoparticles: An Effective Route to Patterned Diamond Structure Fabrication*. Langmuir, 2011. 27(19): p. 11981-11989.

295. Sun, B., S.E. Baker, J.E. Butler, H. Kim, J.N. Russell, L. Shang, K.-Y. Tse, W. Yang and R.J. Hamers, *Covalent Molecular Functionalization of Diamond Thin-Film Transistors*. *Diamond and Related Materials*, 2007. **16**(8): p. 1608-1615.
296. Yang, W., J.E. Butler, J.N. Russell Jr and R.J. Hamers, *Direct Electrical Detection of Antigen-Antibody Binding on Diamond and Silicon Substrates using Electrical Impedance Spectroscopy*. *Analyst*, 2007. **132**(4): p. 296-306.
297. Kondo, T., I. Neitzel, V.N. Mochalin, J. Urai, M. Yuasa and Y. Gogotsi, *Electrical Conductivity of Thermally Hydrogenated Nanodiamond Powders*. *Journal of Applied Physics*, 2013. **113**(21): p. 214307-214311.
298. Varshney, M. and Y. Li, *Interdigitated Array Microelectrodes Based Impedance Biosensors for Detection of Bacterial Cells*. *Biosensors and Bioelectronics*, 2009. **24**(10): p. 2951-2960.
299. Yang, L., Y. Li and G.F. Erf, *Interdigitated Array Microelectrode-Based Electrochemical Impedance Immunosensor for Detection of Escherichia Coli O157: H7*. *Analytical Chemistry*, 2004. **76**(4): p. 1107-1113.
300. Varshney, M. and Y. Li, *Interdigitated Array Microelectrode based Impedance Biosensor Coupled with Magnetic Nanoparticle-Antibody Conjugates for Detection of Escherichia Coli O157:H7 in Food Samples*. *Biosensors and Bioelectronics*, 2007. **22**(11): p. 2408-2414.
301. Li, H. and R. Bashir, *Dielectrophoretic separation and manipulation of live and heat-treated cells of Listeria on microfabricated devices with interdigitated electrodes*. *Sensors and Actuators B: Chemical*, 2002. **86**(2-3): p. 215-221.
302. Elitas, M., R. Martinez-Duarte, N. Dhar, J.D. McKinney and P. Renaud, *Dielectrophoresis-based purification of antibiotic-treated bacterial subpopulations*. *Lab on a Chip*, 2014. **14**(11): p. 1850-1857.
303. Chia-Fu, C. and F. Zenhausern, *Electrodeless dielectrophoresis for micro total analysis systems*. *Engineering in Medicine and Biology Magazine, IEEE*, 2003. **22**(6): p. 62-67.
304. Glynn, M., D. Kirby, D. Chung, D.J. Kinahan, G. Kijanka and J. Ducr  e, *Centrifugo-magnetophoretic Purification of CD4+ Cells from Whole Blood toward Future HIV/AIDS Point-of-Care Applications*. *Journal of Laboratory Automation*, 2013.
305. Karle, M., J. Miwa, G. Roth, R. Zengerle and F. von Stetten. *A Novel Microfluidic Platform for Continuous DNA Extraction and Purification using Laminar Flow Magnetophoresis*. in *Micro Electro Mechanical Systems, 2009. MEMS 2009. IEEE 22nd International Conference on*. 2009.

306. Strohmeier, O., A. Emperle, G. Roth, D. Mark, R. Zengerle and F. von Stetten, *Centrifugal gas-phase transition magnetophoresis (GTM) - a generic method for automation of magnetic bead based assays on the centrifugal microfluidic platform and application to DNA purification*. Lab on a Chip, 2013. 13(1): p. 146-155.
307. Petersson, F., L. Åberg, A.-M. Swärd-Nilsson and T. Laurell, *Free flow acoustophoresis: microfluidic-based mode of particle and cell separation*. Analytical chemistry, 2007. 79(14): p. 5117-5123.
308. Petersson, F., L. Åberg, A.-M. Swärd-Nilsson and T. Laurell, *Free Flow Acoustophoresis: Microfluidic-Based Mode of Particle and Cell Separation*. Analytical Chemistry, 2007. 79(14): p. 5117-5123.
309. Choi, S., T. Ku, S. Song, C. Choi and J.-K. Park, *Hydrophoretic high-throughput selection of platelets in physiological shear-stress range*. Lab on a Chip, 2011. 11(3): p. 413-418.
310. Millet, L.J., K. Park, N.N. Watkins, K.J. Hsia and R. Bashir, *Separating Beads and Cells in Multi-channel Microfluidic Devices Using Dielectrophoresis and Laminar Flow*. 2011(48): p. e2545.
311. Park, I.S., K. Eom, J. Son, W.-J. Chang, K. Park, T. Kwon, D.S. Yoon, R. Bashir and S.W. Lee, *Microfluidic Multifunctional Probe Array Dielectrophoretic Force Spectroscopy with Wide Loading Rates*. ACS Nano, 2012. 6(10): p. 8665-8673.
312. Lee, H.-Y. and J. Voldman, *Optimizing Micromixer Design for Enhancing Dielectrophoretic Microconcentrator Performance*. Analytical Chemistry, 2007. 79(5): p. 1833-1839.
313. Regtmeier, J., T.T. Duong, R. Eichhorn, D. Anselmetti and A. Ros, *Dielectrophoretic Manipulation of DNA: Separation and Polarizability*. Analytical Chemistry, 2007. 79(10): p. 3925-3932.
314. Regtmeier, J., R. Eichhorn, L. Bogunovic, A. Ros and D. Anselmetti, *Dielectrophoretic Trapping and Polarizability of DNA: The Role of Spatial Conformation*. Analytical Chemistry, 2010. 82(17): p. 7141-7149.
315. Tang, S.-Y., W. Zhang, S. Baratchi, M. Nasabi, K. Kalantar-zadeh and K. Khoshmanesh, *Modifying Dielectrophoretic Response of Nonviable Yeast Cells by Ionic Surfactant Treatment*. Analytical Chemistry, 2013. 85(13): p. 6364-6371.
316. Huang, Y., S. Joo, M. Duhon, M. Heller, B. Wallace and X. Xu, *Dielectrophoretic Cell Separation and Gene Expression Profiling on Microelectronic Chip Arrays*. Analytical Chemistry, 2002. 74(14): p. 3362-3371.

317. Yang L, B.P., Chatni MR, Seop Lim K, Bhunia AK, Ladisch M, Bashir R., *A multifunctional micro-fluidic system for dielectrophoretic concentration coupled with immuno-capture of low numbers of Listeria monocytogenes*. Lab Chip, 2006. **6**(7): p. 896-905.
318. Arumugam, P.U., H. Chen, A.M. Cassell and J. Li, *Dielectrophoretic Trapping of Single Bacteria at Carbon Nanofiber Nanoelectrode Arrays†*. The Journal of Physical Chemistry A, 2007. **111**(49): p. 12772-12777.
319. Lapizco-Encinas, B.H., B.A. Simmons, E.B. Cummings and Y. Fintschenko, *Dielectrophoretic Concentration and Separation of Live and Dead Bacteria in an Array of Insulators*. Analytical Chemistry, 2004. **76**(6): p. 1571-1579.
320. Auerswald, J. and H.F. Knapp, *Quantitative assessment of dielectrophoresis as a micro fluidic retention and separation technique for beads and human blood erythrocytes*. Microelectronic Engineering, 2003. **67–68**(0): p. 879-886.
321. Mike Arnold, W. and N.R. Franich, *Cell isolation and growth in electric-field defined micro-wells*. Current Applied Physics, 2006. **6**(3): p. 371-374.
322. Cho, Y.K., S. Kim, K. Lee, C. Park, J.G. Lee and C. Ko, *Bacteria concentration using a membrane type insulator-based dielectrophoresis in a plastic chip*. Electrophoresis, 2009. **30**(18): p. 3153-3159.
323. Iliescu, C., L. Yu, F.E.H. Tay and B. Chen, *Bidirectional field-flow particle separation method in a dielectrophoretic chip with 3D electrodes*. Sensors and Actuators B: Chemical, 2008. **129**(1): p. 491-496.
324. Tay, F.E.H., L. Yu, A.J. Pang and C. Iliescu, *Electrical and thermal characterization of a dielectrophoretic chip with 3D electrodes for cells manipulation*. Electrochimica Acta, 2007. **52**(8): p. 2862-2868.
325. Voldman, J., M.L. Gray, M. Toner and M.A. Schmidt, *A Microfabrication-Based Dynamic Array Cytometer*. Analytical Chemistry, 2002. **74**(16): p. 3984-3990.
326. Aldaeus, F., Y. Lin, J. Roeraade and G. Amberg, *Superpositioned dielectrophoresis for enhanced trapping efficiency*. Electrophoresis, 2005. **26**(22): p. 4252-4259.
327. Chen, D.F., H. Du and W.H. Li, *A 3D paired microelectrode array for accumulation and separation of microparticles*. Journal of Micromechanics and Microengineering, 2006. **16**(7): p. 1162.
328. Chen, D.F., H. Du and W.H. Li, *Bioparticle separation and manipulation using dielectrophoresis*. Sensors and Actuators A: Physical, 2007. **133**(2): p. 329-334.

329. Dürr, M., J. Kentsch, T. Müller, T. Schnelle and M. Stelzle, *Microdevices for manipulation and accumulation of micro- and nanoparticles by dielectrophoresis*. ELECTROPHORESIS, 2003. **24**(4): p. 722-731.
330. Pethig R1, T.M., Lee RS., *Enhancing traveling-wave dielectrophoresis with signal superposition*. IEEE Eng Med Biol Mag, 2003. **22**(6): p. 43-50.
331. Gadish, N. and J. Voldman, *High-Throughput Positive-Dielectrophoretic Bioparticle Microconcentrator*. Analytical Chemistry, 2006. **78**(22): p. 7870-7876.
332. Tenne, R., K. Patel, K. Hashimoto and A. Fujishima, *Efficient electrochemical reduction of nitrate to ammonia using conductive diamond film electrodes*. Journal of Electroanalytical Chemistry, 1993. **347**(1-2): p. 409-415.
333. Yang, L., P. Banada, A. Bhunia and R. Bashir, *Effects of Dielectrophoresis on Growth, Viability and Immuno-reactivity of Listeria monocytogenes*. Journal of Biological Engineering, 2008. **2**(1): p. 6.
334. Kim, J.S., G.P. Anderson, J.S. Erickson, J.P. Golden, M. Nasir and F.S. Ligler, *Multiplexed Detection of Bacteria and Toxins Using a Microflow Cytometer*. Analytical Chemistry, 2009. **81**(13): p. 5426-5432.
335. Fraga, M., N. Vilariño, M.C. Louzao, K. Campbell, C.T. Elliott, K. Kawatsu, M.R. Vieytes and L.M. Botana, *Detection of Paralytic Shellfish Toxins by a Solid-Phase Inhibition Immunoassay Using a Microsphere-Flow Cytometry System*. Analytical Chemistry, 2012. **84**(10): p. 4350-4356.
336. Rodríguez, L.P., N. Vilariño, J. Molgó, R. Aráoz, M.C. Louzao, P. Taylor, T. Talley and L.M. Botana, *Development of a Solid-Phase Receptor-Based Assay for the Detection of Cyclic Imines Using a Microsphere-Flow Cytometry System*. Analytical Chemistry, 2013. **85**(4): p. 2340-2347.
337. Fraga, M., N. Vilariño, M.C. Louzao, P. Rodríguez, K. Campbell, C.T. Elliott and L.M. Botana, *Multidetecction of Paralytic, Diarrheic, and Amnesic Shellfish Toxins by an Inhibition Immunoassay Using a Microsphere-Flow Cytometry System*. Analytical Chemistry, 2013. **85**(16): p. 7794-7802.
338. Bounds, C.O., J. Upadhyay, N. Totaro, S. Thakuri, L. Garber, M. Vincent, Z. Huang, M. Hupert and J.A. Pojman, *Fabrication and Characterization of Stable Hydrophilic Microfluidic Devices Prepared via the in Situ Tertiary-Amine Catalyzed Michael Addition of Multifunctional Thiols to Multifunctional Acrylates*. ACS Applied Materials & Interfaces, 2013. **5**(5): p. 1643-1655.
339. Lu, B., M.R. Smyth and R. O'Kennedy, *Tutorial review. Oriented immobilization of antibodies and its applications in immunoassays and immunosensors*. Analyst, 1996. **121**(3): p. 29R-32R.

340. Febbraio, F., L. Merone, G.P. Cetrangolo, M. Rossi, R. Nucci and G. Manco, *Thermostable Esterase 2 from Alicyclobacillus acidocaldarius as Biosensor for the Detection of Organophosphate Pesticides*. Analytical Chemistry, 2011. **83**(5): p. 1530-1536.
341. Wang, J., *Electrochemical Glucose Biosensors*. Chemical Reviews, 2008. **108**(2): p. 814-825.
342. Wilson, G.S. and Y. Hu, *Enzyme-Based Biosensors for in Vivo Measurements*. Chemical Reviews, 2000. **100**(7): p. 2693-2704.
343. Long, Y.-T., C.-Z. Li, H.-B. Kraatz and J.S. Lee, *AC Impedance Spectroscopy of Native DNA and M-DNA*. Biophysical Journal, 2003. **84**(5): p. 3218-3225.
344. Varshney, M. and Y. Li, *Interdigitated array microelectrode based impedance biosensor coupled with magnetic nanoparticle–antibody conjugates for detection of Escherichia coli O157:H7 in food samples*. Biosensors and Bioelectronics, 2007. **22**(11): p. 2408-2414.
345. Varshney, M., Y. Li, B. Srinivasan and S. Tung, *A label-free, microfluidics and interdigitated array microelectrode-based impedance biosensor in combination with nanoparticles immunoseparation for detection of Escherichia coli O157:H7 in food samples*. Sensors and Actuators B: Chemical, 2007. **128**(1): p. 99-107.
346. Lee, J.A., S. Hwang, J. Kwak, S.I. Park, S.S. Lee and K.-C. Lee, *An electrochemical impedance biosensor with aptamer-modified pyrolyzed carbon electrode for label-free protein detection*. Sensors and Actuators B: Chemical, 2008. **129**(1): p. 372-379.
347. Liao, W. and X.T. Cui, *Reagentless aptamer based impedance biosensor for monitoring a neuro-inflammatory cytokine PDGF*. Biosensors and Bioelectronics, 2007. **23**(2): p. 218-224.
348. Ghindilis, A.L., M.W. Smith, K.R. Schwarzkopf, C. Zhan, D.R. Evans, A.M. Baptista and H.M. Simon, *Sensor Array: Impedimetric Label-Free Sensing of DNA Hybridization in Real Time for Rapid, PCR-Based Detection of Microorganisms*. Electroanalysis, 2009. **21**(13): p. 1459-1468.
349. Daniels, J.S. and N. Pourmand, *Label-Free Impedance Biosensors: Opportunities and Challenges*. Electroanalysis, 2007. **19**(12): p. 1239-1257.
350. Katz, E. and I. Willner, *Probing Biomolecular Interactions at Conductive and Semiconductive Surfaces by Impedance Spectroscopy: Routes to Impedimetric Immunosensors, DNA-Sensors, and Enzyme Biosensors*. Electroanalysis, 2003. **15**(11): p. 913-947.
351. Cai, W.e.a., *Chemical modification and patterning of iodine-terminated silicon surfaces using visible light*. J. Phys. Chem. , 2002. **B 106**: p. 2656–2664.

352. Alehashem, S., F. Chambers, J.W. Strojek, G.M. Swain and R. Ramesham, *Cyclic Voltammetric Studies of Charge Transfer Reactions at Highly Boron-Doped Polycrystalline Diamond Thin-Film Electrodes*. Analytical Chemistry, 1995. **67**(17): p. 2812-2821.
353. Clare, T.L., B.H. Clare, B.M. Nichols, N.L. Abbott and R.J. Hamers, *Functional Monolayers for Improved Resistance to Protein Adsorption: Oligo(ethylene glycol)-Modified Silicon and Diamond Surfaces*. Langmuir, 2005. **21**(14): p. 6344-6355.
354. Sun, B., S.E. Baker, J.E. Butler, H. Kim, J.N. Russell Jr, L. Shang, K.-Y. Tse, W. Yang and R.J. Hamers, *Covalent molecular functionalization of diamond thin-film transistors*. Diamond and Related Materials, 2007. **16**(8): p. 1608-1615.
355. Courtney Stavis, T.L.C., James E. Butler, Adarsh D. Radadia, Rogan Carr, Hongjun Zeng, William P. King, John A. Carlisle, Aleksei Aksimentiev, Rashid Bashir, and Robert J. Hamers, *Surface functionalization of thin-film diamond for highly stable and selective biological interfaces*. PNAS, 2011. **108**(3): p. 983-988.
356. Grausova, L., L. Bacakova, A. Kromka, S. Potocky, M. Vanecek, M. Nesladek and V. Lisa, *Nanodiamond as Promising Material for Bone Tissue Engineering*. Journal of Nanoscience and Nanotechnology, 2009. **9**(6): p. 3524-3534.
357. Randles, J.E.B., *Kinetics of rapid electrode reactions*. Discussions of the Faraday Society, 1947. **1**(0): p. 11-19.
358. van de Lagemaat, J., D. Vanmaekelbergh and J.J. Kelly, *Electrochemistry of homoepitaxial CVD diamond: energetics and electrode kinetics in aqueous electrolytes*. Journal of Electroanalytical Chemistry, 1999. **475**(2): p. 139-151.
359. Barsoukov, E. and J.R. Macdonald, *Impedance spectroscopy: theory, experiment, and applications*. 2005: John Wiley & Sons.